UCL Université catholique de Louvain

École polytechnique de Louvain (EPL)

Random field generation

Dissertation presented by
Adissa LAURENT

for obtaining the Master's degree in
Mathematical Engineering

Supervisor(s)
Vincent LEGAT , Samih ZEIN

Reader(s)
Issam DOGHRI

Academic year 2016-2017

Rue Archimède, 1 bte L6.11.01, 1348 Louvain-la-Neuve **www.uclouvain.be/epl**

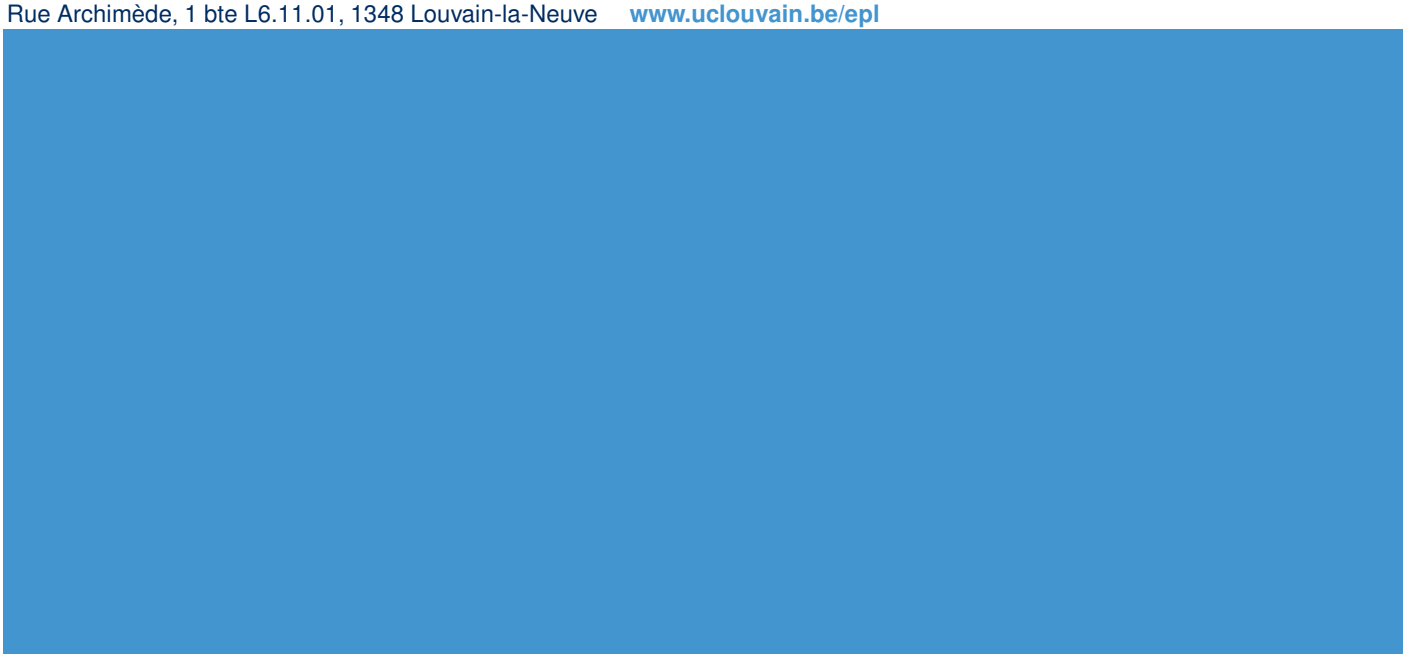

Abstract

This thesis, done in collaboration with Cenaero, contributes to the MACOBIO project. It develops a numerical tool modelling the properties of heterogeneous materials based on random field generation and analysing the mechanical responses of the composite objects.

After reviewing the different composite materials and mechanical laws based on homogenization methods, this thesis presents a numerical tool to simulate Gaussian random fields on 3D surfaces.

It first defines the covariance function associated with the Gaussian random field. The random field is then discretised on finite elements using Karhunen-Loève expansion. The Karhunen-Loève expansion is computed by solving a Fredholm integral equation of the second kind.

The integrals involved by the Fredholm equation are evaluated using Galerking methods. The integrals depend on discrete values of the covariance function, itself a function of the geodesic distances. The geodesic distances are evaluated using the fast marching method or the recursive fast marching method. The recursive fast marching method is applied on 2D and 3D surfaces and the errors of the method are characterized.

The random field generation method is applied on a composite chair. Two uncertain properties are modelled: the fibre volume fraction and the angles of the plies. Two mechanical responses (the deflection and the Tsai-Wu criterion) are analysed by means of the Monte Carlo method.

Acknowledgement

First of all, I would like to offer my special thanks to my master thesis directors, Vincent Legat and Samih Zein, for their availability, support and advices throughout the year.

Thanks as well to Issam Doghri for accepting to read this thesis and the lessons he gave me about composite objects.

This thesis would never have existed without the opportunity offered by Cenaero's team. It has been a real pleasure to work on such an interesting and multifaceted subject. To all of you, thank you.

Contents

List of Symbols

$\boldsymbol{e}_i$	Coordinate axis with $i = 1, 2, 3$ or $i = x, y$.	
ϵ_{nn}	Normal strain in direction n.	[\]
ϵ_{ns}	Shear strain between direction n and s.	[\]
$\boldsymbol{\epsilon}$	Infinitesimal strain tensor.	[\]
$\boldsymbol{\sigma}$	Infinitesimal stress tensor.	$[Pa]$
$\boldsymbol{C}$	Stiffness tensor.	$[Pa]$
$\boldsymbol{S}$	Compliance tensor.	$[Pa^{-1}]$
$W(\boldsymbol{\epsilon})$	Strain energy function per unit volume.	$[J]$
E_i	Young's modulus, in direction i ($i = 1, 2, 3$).	$[Pa]$
E_f	Young's modulus of the fibre.	$[Pa]$
E_m	Young's modulus of the matrix.	$[Pa]$
ν_{ij}	Poisson's coefficient corresponding to the displacement in direction j when a force is applied in direction i ($i, j = 1, 2, 3$).	[\]
ν_f	Poisson coefficient of the fibre.	[\]
ν_m	Poisson coefficient of the matrix.	[\]
G_{ij}	Shear modulus in direction i on a plane with normal j.	$[Pa]$
G_f	Shear modulus of the fibre.	$[Pa]$
G_m	Shear modulus of the matrix.	$[Pa]$
V_f	Fibre volume fraction.	[\]
$\mathtt{u}_0, \mathtt{v}_0, \mathtt{w}_0$	Displacements on the mid-surface of the laminate.	$[m]$
$\mathtt{u}, \mathtt{v}, \mathtt{w}$	Displacements inside the laminate.	$[m]$
$N(x, y)$	Resultant forces per segment.	$[Nm^{-1}]$
$M(x, y)$	Resultant moments per segment.	$[N]$
$(\Theta, \mathcal{F}, \mathbb{P})$	Probability space with Θ the sample space, $\mathcal{F}$ the event space, $\mathbb{P}$ the probability function.	
Ω	Computation field.	
Ω_h	Mesh.	
Ω^e	Element of the mesh.	
$u(\boldsymbol{x}, \theta)$	Second order random process.	
$\bar{u}(\boldsymbol{x})$	Mean of the second order random process.	
$u_0(\boldsymbol{x}, \theta)$	Zero mean random process.	
σ	Standard deviation.	
$\mathcal{L}^2$	Space of square integrable functions.	
$E[\cdot]$	Expectation.	
$C(\boldsymbol{x}, \boldsymbol{y})$	Covariance function.	
$l_{c,Cov}$	Covariance characteristic length.	$[m]$
$d(\boldsymbol{x}, \boldsymbol{y})$	Distance between $\boldsymbol{x}$ and $\boldsymbol{y}$.	$[m]$
$\xi_i(\theta)$	Standard normal uncorrelated variable	
$\phi_i(\boldsymbol{x})$	Eigenfunction.	
λ_i	Eigenvalue.	
$\hat{\phi}_i(\boldsymbol{x})$	Approximated eigenfunction.	
$\hat{\lambda}_i$	Eigenvalue associated with $\hat{\phi}_i(\boldsymbol{x})$.	
δ_{ij}	Delta function.	
$h_i(\boldsymbol{x})$	Shape function.	
$\mathcal{V}_h$	Set of shape functions.	
w_p, w_q	Quadrature weights.	
$\boldsymbol{x}_p, \boldsymbol{x}_q$	Quadrature points.	
∇f	Gradient of function f.	
T_A	Distance of point A with respect to the starting point.	$[m]$
ABC	Triangle.	
AB	Segment between A and B.	
$\boldsymbol{AB}$	Vector starting at A and ending at B.	
$\|\|x\|\|_M$	Anisotropic norm of x.	

$\epsilon_{ani}(\boldsymbol{x}, \boldsymbol{y})$ ..... Relative error at point $\boldsymbol{y}$ between exact anisotropic and AFMM distances w.r.t. point $\boldsymbol{x}$.
$\epsilon_{\sigma}(\boldsymbol{x})$ ..... Error variance.
$\bar{\epsilon}_{\sigma}(\boldsymbol{x})$ ..... Mean error variance.

List of Acronyms

FVF ..... Fibre volume fraction.
RTM ..... Resin transfer moulding.
FMM ..... Fast Marching Method.
$AFMM$ ..... Recursive Fast Marching Method.
RVE ..... Representative volume element.

List of Figures

List of Tables

List of Algorithms

Chapter 1

Introduction

The use of composite objects has soared during the 20th century. Even though composite objects were already used in classical times to build constructions made of wood and mud, the modern sense of composite has appeared with the discoveries of plastics. Composite materials are created by combining a matrix with reinforcement. The matrix, usually made of plastics, transfers the loads to the reinforcement, for instance carbon fibres, and ensures the cohesion between the two materials. Among composite objects, one can find tennis rackets, skis, cars, aircraft and even spacecraft [14]! For instance, the Boeing 787 Dreamliner contains about 50% of advanced composite materials [19].

The composite market is in constant evolution. Ongoing researches study new composites made of bio-degradable, environment friendly components. Those materials are made of bio-based matrices and reinforced with vegetal fibers. Some facts show their increasing importance. For instance, the bio-based market earnings are approximately 3% of those of the polymer market ($300 billion dollar sales with an annual growth rate of 3%) and its growth rate is twice as large as the one of the plastic industry [1].

The goal of the MACOBIO project is to develop composite materials reinforced with biofibres [12]. MACOBIO is part of the 2014-2020 FEDER project "Low Carbon Footprint Materials". The partners of this project are research centres and universities. As a member of the project, Cenaero provides expertise in numerical simulations. One of the objective of Cenaero, to which this thesis contributes, is to develop a numerical tool analysing the effect of uncertain properties on the mechanical responses of composite objects. This is of utmost importance as biocomposites suffer from large variations in their properties and characteristics. Those variations occur during manufacturing and impact the mechanical behaviour of the final object, sometimes even leading to failure and damage [38].

Heterogeneous materials, like composite materials, are usually modelled using homogenisation techniques. Those techniques, applied to the surface of the object, do not represent the variability of properties inherent to composite objects, especially those made of bio-based materials. The idea is to model an heterogeneous material by splitting it in several, smaller, homogeneous materials. The material properties of the reinforcement and the matrix are considered constant. The heterogeneity is described by discrete values of a random field. Those discrete values can, for instance, define the proportion of reinforcement in the material.

The random field is characterized by a covariance function (itself a function of distances, standard deviation and covariance characteristic length) and a mean value. Random fields can be generated using Karhunen-Loève expansion and discretised by means of finite elements. Discrete values of the covariance function are necessary to solve the Karhunen-Loève expansion. In order to compute those values, the distance between discrete points needs to be evaluated. Because the surfaces of composite objects are 3D surfaces, the Euclidean distance, contrarily to the Fast Marching Method [28] and the Recursive Fast Marching Method [29], does not give the correct distances between points on the surface of the object.

Once the field is generated, the properties of the whole material can be defined and mechanical loads applied on the object. The mechanical responses of the object are finally analysed using Monte Carlo method.

Before addressing results, it is necessary to lay out the theoretical basis of several subjects. The first subject, explained in Chapter 2, is the classification of composite materials, the uncertainties that impact their properties and the manufacturing steps that create them. The second subject, described in Chapter 3, is the mechanical behaviour of laminates (a given type of composite objects) and the prediction of failure or damage. Then, Chapter 4 defines Gaussian random fields and explains how to numerically represent them. Chapter 5 explains how the Fast Marching Method and the Recursive Fast Marching Method work. Chapter 6 enumerates the different software used, explains how Cenaero's program works and highlight my personal contribution. It ends with the mechanical analysis of a chair whose properties are uncertain. The last chapter summarizes the thesis and outlines future possible researches.

Chapter 2

Composite materials

The goal of this chapter is to classify composite materials depending on their components (matrix and reinforcement) [3, 15, 18, 22, 36], describe a manufacturing process [3, 15, 22, 27, 34, 36] and the uncertainties it generates [38].

2.1 Classification

Composite materials are made of two or more distinct and separable components of different shapes, chemical compositions or mechanical properties. The continuous phase, also called the *matrix*, surrounds and transfer the loads to the reinforcement. The *reinforcement* reinforces the matrix as it usually possesses higher mechanical properties. Mixing the matrix and the reinforcement allows to design a new, heterogeneous, material whose properties are superior in some sense from each of its components.

Composite materials can be classified based on their fibres' and matrix' types. Table 2.1 gives several examples of composite materials with metallic, organic or mineral matrices [15].

Composite material	**Constituent part**	**Applications**
Metallic matrix	Aluminum matrix, bore fibres Aluminium matrix, carbon fibres	Spaceship
Organic matrix		
Paper, cardboard	Resin, filling, cellulose fibre	Printing, Wrapping
Particle board	Resin, wood chips	Carpentry
Fibre board	Resin, wood fibres	Buildings
Seal material	Bitumen, elastomers, textile insert	Roofing
Mineral matrix		
Carbon-Carbon composite	Carbon matrix, carbon fibres	Sports, bio-medical
Concrete	Cement, sand, gravel	Buildings

Table 2.1: Examples of composite materials (definition with large scope)

Organic matrices, and in particular polymeric matrices, are the most common. Their mechanical properties and weights are low compared to metals and minerals. Reinforcing polymers can lead to high gains in term of mechanical properties. Furthermore, manufacturing polymer matrix composites does not require high temperature or pressure [36]. Therefore, and in order to restrict the scope of this thesis, only composite materials with plastic matrices will be considered. In the general case, such composite materials can be reinforced using metallic, organic or mineral fibres. In practice, industrial applications with organic matrices are reinforced with [15]

- metallic fibres: aluminium, boron, ...
- organic fibres: Kevlar, polyamides, natural fibres, ...
- mineral fibres: glass, carbon, ...

Composite materials can also be classified based on reinforcement topology. It can be made of fibres or particles. A *fibre*, contrarily to a *particle*, possesses a primary direction as its length is much greater than its diameter. The *aspect ratio*, the ratio of length to diameter, determines whether fibres are continuous or short. *Continuous fibres*, contrarily to *short fibres*, have high aspect ratios. Short fibres have random or preferential orientations. Long fibres can be unidirectional or woven. When fibres are organised with a preferential direction, the material is *anisotropic*, at least one of its property vary depending on the considered direction. Otherwise, the material is *isotropic*. When a layer of reinforcement is impregnated with resin, it is called a *ply*. A ply is thus a material made of two distinct materials: the fibre and the resin. Such materials are *heterogeneous* (in opposition to *homogeneous* materials). The stacking sequence of several plies of different orientations and thickness's form a *laminate*.

2.1.1 Matrix

Plastic are classified, based on their chemical structures, in thermosetting and thermoplastic. Those two families possess very different mechanical and thermal properties.

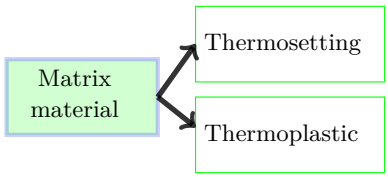

Figure 2.1: Classification of matrix materials.

Thermosetting resins form strong covalent bounds, also called *cross-links*, between polymer chains during the hardening process. Because of cross-links, thermosetting resins can not be remelted to be reshaped. However, they possess increased stiffness and may be used at high temperatures. The most common thermosetting resins in decreasing sequence are unsaturated polyester, epoxy, and phenolic [36].
Thermoplastic resins, contrarily to thermosetting resins, are linear polymers and do not cross-link. Bondings between chains are due to weak, easily broken, van der Waals forces. Thermosetting resins have low manufacturing costs but also low mechanical and thermo-mechanical properties.

2.1.2 Reinforcement

The reinforcement can be characterized by its topology (aspect ratio and orientation) and its nature (e.g. glass, carbon, aramid or natural fibres).

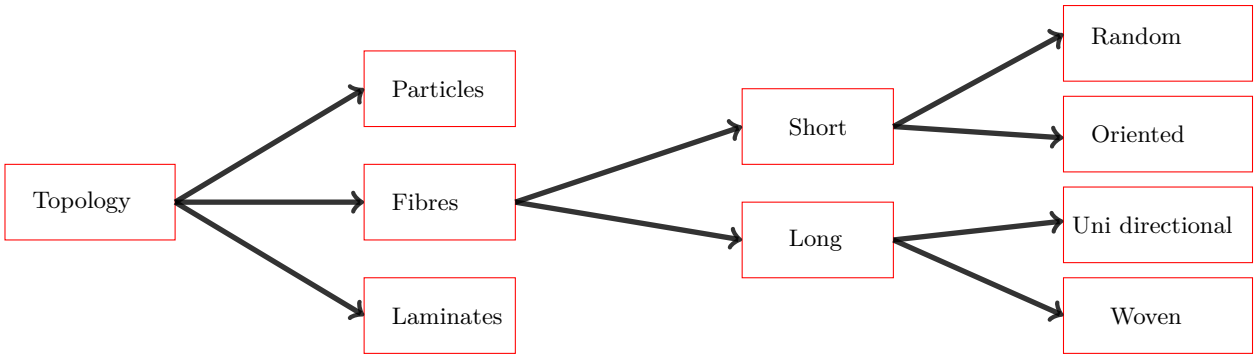

Figure 2.2: Classification of reinforcement based on topology.

The *aspect ratio* of the reinforcement measures the ratio between its length and its diameter. Particles have an aspect ratio close to one as they have approximately the same dimensions in all directions. Fibres, either long or short, cover a wider range of aspects ratios with smaller aspect ratios corresponding to short fibres. The behaviour of continuous fibre composites is different form composite reinforced with short fibres or particles. However, there does not exist a constant aspect ratio under which fibres are called short. Even inside a composite reinforced with short fibres, the lengths of the fibres vary [36].

The orientations of short and long fibres has major impact on the mechanical properties of the final composite object. The possible orientations of short fibres (aligned parallel to each other, randomly oriented in the plane or oriented with a preferential direction) are shown on figure 2.3 [22].
Long fibres can form a *mat* when randomly oriented, a *unidirectional composite* when aligned in one direction or a *fabric* when woven. Mats are made of randomly oriented long or short fibres glued together. They possess isotropic properties and, in the case of long fibres, can deform easily which makes them perfect for moulding complex geometries. Unidirectional composites (the fibre structure is shown on figure 2.4) have high mechanical properties in the direction of the fibres and poor mechanical properties in the orthogonal direction. Woven fabrics are made of parallel warp yarns in the fabric direction and a weft going over and under the warp yarns. Fibres are woven following different patterns summarised in figure 2.5.
Finally, laminates are made of different plies. Each ply may be reinforced with long unidirectional or woven fibres or with short random or oriented fibres (see figure 2.6). When laminates are made of unidirectional fibres, they are denoted by the angle between the fibre direction and the reference axis x.

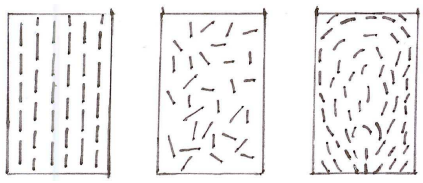

Figure 2.3: From left to right: short aligned fibres (A), randomly oriented short fibres (B), short fibres with preferential directions (C) (based on [18]).

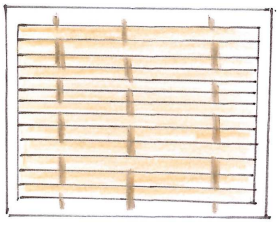

Figure 2.4: Uni-directional fibre structure.

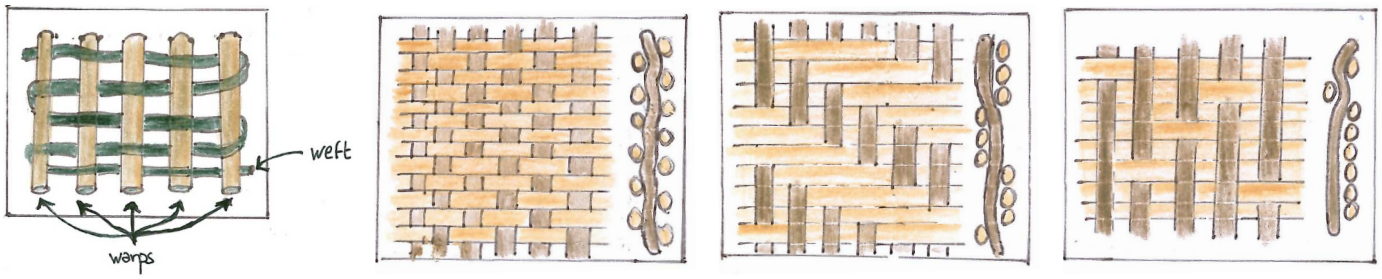

(a) Woven fabric structure (b) Plain weave (c) Twill weave (d) Satin weave

Figure 2.5: Woven fabric patterns.

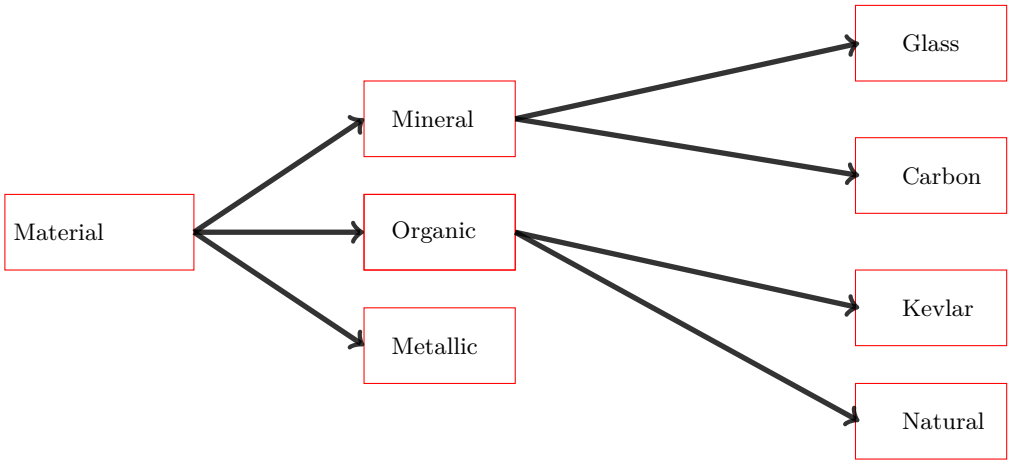

Figure 2.8: Classification of reinforcement based on its nature.

Glass fibres perform well, have reduced costs and are mostly isotropic. They are mainly made of silica (SiO_2) to which aluminium, boron, calcium and other oxides are added. Depending on the composition, glass fibres are classified as type E, R and S glass. The most common is type E glass because of its good mechanical and electrical properties. Types R and S glass fibres have higher mechanical performances but higher costs and are used for aeronautical applications. Strands can be chopped into fibres of a few centimetres, crushed or milled, assembled without twist, or twisted to make yarn which may be woven.

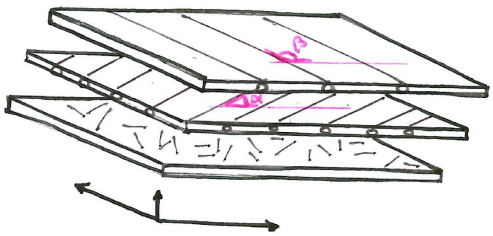

Figure 2.6: Laminate made of one ply with randomly oriented short fibres and two uni-directional plies.

Carbon fibres have very high mechanical properties, even at high temperature, and low mass density but cost way more than glass fibres. Carbon fibres are made of amorphous or crystalline carbon. Carbon crystals are made of parallel planes of carbon atoms organised in hexagons (see figure 2.7). Carbon atoms belonging to the same plane are bounded with strong covalent bonds. Carbon atoms belonging to different planes are bounded by weak van der Waals forces. Because of the anisotropy of carbon fibres, the manufacturing processes try to obtain carbon fibres with carbon planes parallel with the direction of the fibres.

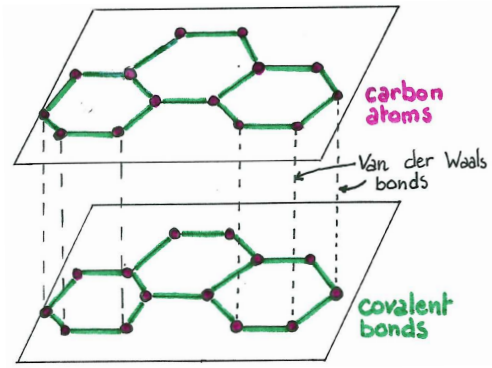

Figure 2.7: Structure of carbon crystal.

The most famous aramid fibres are called Kevlar and manufactured by Dupont de Nemours. Kevlar fibres have mechanical properties similar to carbon fibres in the direction of the fibres and low mass density. However, they possess weak resistance in compression and bending and suffer under high temperatures.

Natural fibres such as cotton, silk, wool, jute, hemp and sisal are used in everyday life for textiles and rope. Among those, vegetable fibres are themselves composite structures of lignin and hemicellulose reinforced with cellulose. They possess a high aspect ratio (greater than 1000) and, compared to synthetic fibres, have low manufacturing costs and cause less abrasive damage to manufacturing equipment. Furthermore, they allow a smaller CO_2 impact as plants can be regrown with low energy consumption and absorb CO_2 during their growths. However, natural fibres absorb more moisture than synthetic fibres. This leads to augmentation of the fibres' dimensions, negative effects on the composite properties,

greater uncertainties about the properties of the fibres and lower strengths [36, 42, 11].

Composite materials are made of a wide range of components. Those components are characterised by their material and topology. The organisation of composite materials is summarised on figure 2.9. Depending on the characteristic of the composite components, some manufacturing processes will be preferred.

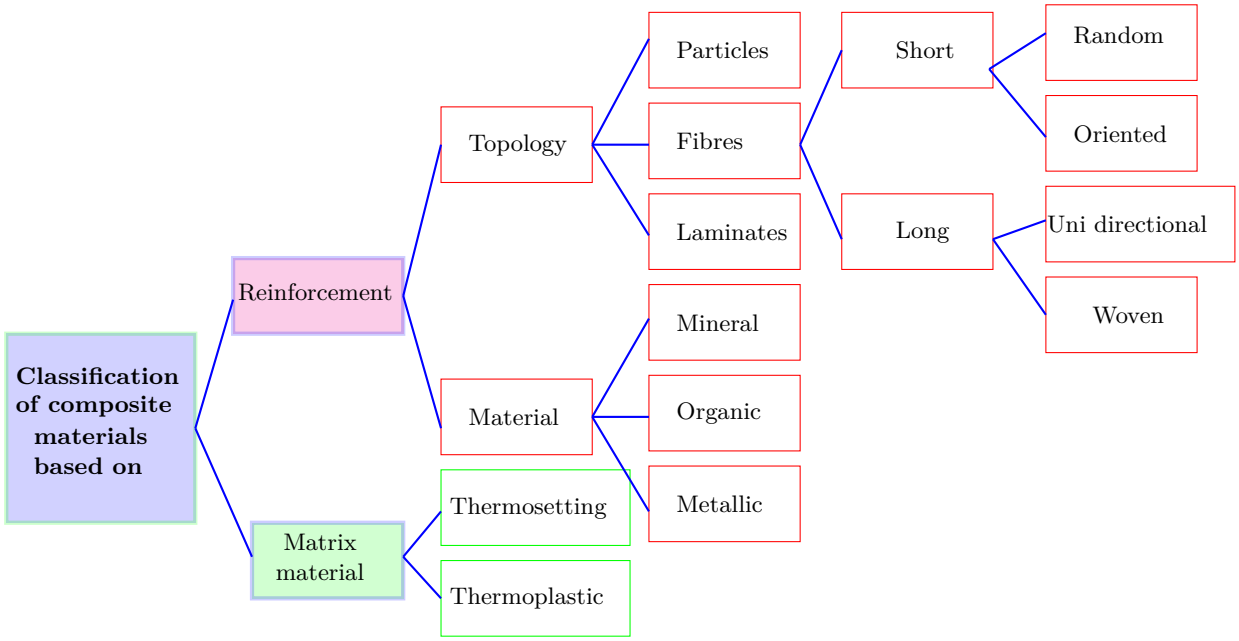

Figure 2.9: Classification of composite materials.

2.2 Manufacturing of polymer matrix composites

During the manufacturing processes of polymer matrix composites, fibres are incorporated into polymer matrices. This can be done directly or using semi-finished products.

Semi-finished products are easy to use and store for future uses. Among semi-finished products, *compounds*, contrarily to *pre-pregs*, contain additives [27]. Pre-pregs are thin sheets of fibres impregnated with low viscosity resin. They possess large fibres volume fractions and, in the case of pre-pregs impregnated with thermosetting resin, have already attained partial reticulation. Compounds are usually made of polyester resin, glass fibres and additives (filling, catalysts, releasing agents, anti-shrinkage agents...).

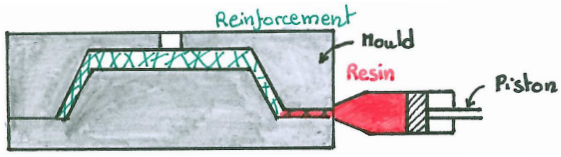

Figure 2.10: Resin transfer moulding process.

Incorporating fibres directly in the matrix during production can be done by hand layup (oldest technique, reliable but slow and costly) and higher production rate techniques such as moulding techniques (compression moulding, resin transfer moulding (RTM), pultrusion,...) and filament winding [34].

Both methods involve several steps subject to several uncertainties: variation in the fibre architecture, matrix material uncertainties and variation in environmental and process conditions. Let's illustrate them with the RTM process, a process producing composite parts of complex shapes at high production rates.

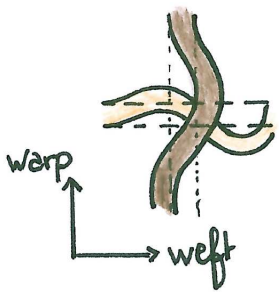

Figure 2.11: Tow waviness

The reinforcement is placed in a closed mould and the low viscosity resin is injected in the mould at low pressure. It flows to fill the mould, coat the fibres and ejects the air (see figure 2.10). The resulting composite may then be cured. *Curing* happens when the composite object becomes harder and tougher.

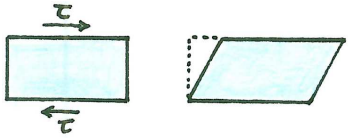

Figure 2.12: Shear deformation

The RTM process suffers from several uncertainties. The reinforcement is in the form of dry textiles, pre-pregs or preforms (reinforcement fabric shaped in a three-dimensional structure). Those fabrics suffer from variability due to tow waviness (the shifting between orthogonal fibres and bended ones) as shown on figure 2.11, size and shape variation [43]. Fibre heterogeneity comes from production, handling and storage of pre-pregs, dry textiles and preforms.

Some moulds have non planar surface which can not be flattened onto a plane without distortion. Draping the reinforcement on the mould, i.e. shaping the fabric to the surface of the mould, leads to significant shape deformations also called *shear deformations*. Such deformation is illustrated on figure 2.12. Shear deformation is mainly due to scissoring (the change in the inter-fibre angle) and inter-fibre sliding [51]. Shear deformation impacts *fibre volume fraction* (FVF) (the volume of fibre compared to the total volume), thickness, permeability, the development of residual stresses during the curing stage, dimensional accuracy and the mechanical properties of the final part.
As the resin is injected in the mould, it impregnates the reinforcement. The impregnation depends on permeability and may result in dry spots and voids (unoccupied regions inside the composite material) due to preferential direction of flows (the flows move faster along the edges of the mould as the preform does not perfectly adhere to the mould), uneven impregnation and resin rich pockets [2]. The permeability itself depends on fibre architecture and more peculiarly on FVF, viscosity and nesting. *Nesting* is the intrusion of one layer of reinforcement into the next : the hills of a reinforcement layer fill the voids formed by the valleys of the opposite reinforcement layer [7]. Nesting has a large effect on permeability, thermal conductivity and the mechanical behaviour of the composite. It impacts the laminate thickness, the FVF and the pore pattern (the way fibres are stacked on each other) and is responsible for the formation of resin rich zones. Nesting is smaller when the shear deformation is great and the fibres tows are tighter to each other. This tightness depends on the inter-tow spacing. If voids are created during the impregnation step, they will create regions of stress concentration eventually leading to local failures, impact on mechanical properties (fatigue strength, durability, inter-laminar shear strength,...) and make moisture absorption more likely [5]. The absorption of water may degrade mechanical performance (swelling, formation of internal stresses, ...) [36].
The curing process is affected by the fibres and matrix properties and by the environmental conditions. Those uncertainties may induce residual stresses, imperfect curing (under-curing and over-curing), voids and thermal degradation [41]. Resin properties vary due to resin composition, environment storing and handling [20]. Variations in thermal, mechanical and thermal-mechanical properties, generated by the composite components and the manufacturing process, impact on the cure process [32]:

- Thermal conductivity variations come from variation in fibres' angle and volume fraction.
- Thermal expansion coefficients are influenced by the moduli and thermal expansion coefficient of the components, the volume fraction and the ply misalignment. Variation in thermal expansion coefficients leads to dimensional instability.
- FVF modifies thermal conductivity, heat capacity, thermal expansion and the total heat of the reaction.

Environment conditions (temperature, moisture or pressure) and tool characteristics make the process even less predictable [32]. For instance, convective heat depends on the characteristic of the tool and other parameters. Its variation may lead to uneven curing and temperature distribution.

To summarise, the manufacturing of composite object is a complex process whose steps are subject to uncertainties. Those uncertainties come from variation in fibre architecture, uncertainties in matrix material and environmental and process conditions. They affect a wide range of physical and mechanical properties. Those properties, in term, affect the behaviour of the final object. The mechanical behaviour of a laminate can be modelled analytically. This is the subject of the next chapter.

Chapter 3

Mechanical behaviour of composite materials

This chapter describes the theoretical models governing the mechanical response of elastic laminates. The mechanical analysis of laminates involves several steps (see figure 3.1):

Micromechanics of a ply Computation of the average properties of every single ply. The average properties of a ply are computed by homogenisation methods using the properties of its different constituents.

Macromechanics of a ply Computation of the stress-strain relationship of the homogenised ply. Estimation of the failure criterion.

Macromechanics of a laminate Laminates are made by stacking several plies. Knowing the average mechanical properties of every ply allows to compute the mechanical properties and the failure criterion of the whole laminate.

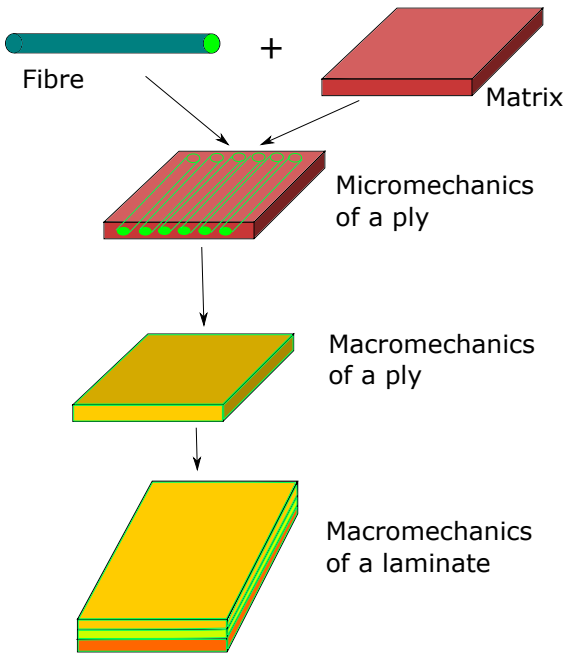

Figure 3.1: Level scales involved in the mechanical analysis of laminates.

The first section of this chapter is a reminder about linear elasticity. It defines stress, strain and the engineering constants (Young modulus, Poisson ratio and shear modulus) and lays out stress-strain relationship for several materials (Hooke's laws). Reminders about stress and strains are based on [47], definition of Hooke's laws and engineering constants on [47, 27, 26, 14, 3].
The second section consider the ply to be homogeneous. It develops Hooke's law for a bi-dimensional, homogeneous and thin ply in $(\boldsymbol{e}_1, \boldsymbol{e}_2)$ and a rotated axis systems. This law defines the macromechanical behaviour of the ply.
The third section consider the ply as an anisotropic, bi-dimensional structure with unidirectional, continuous fibres. For a composite materials made of two distinct materials (the fibres and the matrix), it computes the homogenised engineering constants of the ply that will be used to express Hooke's law of the homogenised ply. This law define the micromechanical properties of the ply.
The fourth section predicts the mechanical response of the laminate structure on which loads and moments are applied.
The last section develops strength failure theories. It analyses a failure criterion inside a ply before analysing failure criterion of the whole laminate. The second, the third, the fourth and the fifth sections are based on [27, 26, 14, 3].

3.1 Reminder about linear elasticity

Let's consider a loaded object in a three-dimensional space. The mechanical loads modify its shape. *Strain* measures the relative deformation of the object and is associated with *stress*, the intensity of the force per unit area. When deformations are not too large, one may apply Hooke's law to *elastic materials*, materials whose response only depend on their current state and not on their past.

3.1.1 Stress and strain

Normal strain is defined as the variation of length of a segment per unit length:

$$\epsilon_{nn} = \frac{ds - dS}{dS}$$

where subscript n denotes the initial direction of the segment, dS the initial length of the segment and ds the length of the segment after loading (see figure 3.2).
Shear strain is the change of angle between two segments that were perpendicular in the body before deformation:

$$\epsilon_{ns} = \frac{\pi}{2} - \lim_{P,Q \to O} \theta \tag{3.1}$$

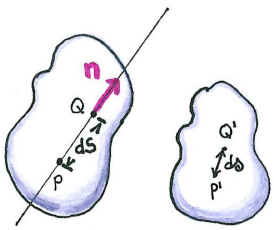

Figure 3.2: Left: body without deformation. Right: body under normal stress.

where subscript n denotes initial direction of OP, subscript s initial direction of OQ and θ the angle $Q'\hat{O}P'$ after deformation of the body (see figure 3.3).

Let's consider a system of orthogonal axis $(\boldsymbol{e}_1, \boldsymbol{e}_2, \boldsymbol{e}_3)$ such that every point $\boldsymbol{x}$ in space can be written as $\boldsymbol{x} = x_1\boldsymbol{e}_1 + x_2\boldsymbol{e}_2 + x_3\boldsymbol{e}_2$. Displacements are denoted by $\boldsymbol{u} = \boldsymbol{x}_t - \boldsymbol{x}_0$ with $\boldsymbol{x}_0$ the initial position and $\boldsymbol{x}_t$ the position at time t. Under small perturbations ($|\nabla \boldsymbol{u}| \ll 1$) and in the orthogonal axis, the *infinitesimal strain tensor* is defined as

$$[\boldsymbol{\epsilon}] = \begin{pmatrix} \epsilon_{11} & \epsilon_{12} & \epsilon_{13} \\ \epsilon_{21} & \epsilon_{22} & \epsilon_{23} \\ \epsilon_{31} & \epsilon_{32} & \epsilon_{33} \end{pmatrix} \tag{3.2}$$

with $\epsilon_{ij} = \frac{1}{2}\left(\frac{\partial u_j}{\partial x_i} + \frac{\partial u_i}{\partial x_j}\right)$, ϵ_{ii} the normal strains, ϵ_{ij} with $i \neq j$ the shear strains and $i, j = 1, 2, 3$. The infinitesimal strain tensor is thus symmetric and only contains 6 independent components.
The stress $\boldsymbol{t}(\hat{\boldsymbol{n}})$ applied on a small surface ΔA with normal vector $\hat{\boldsymbol{n}}$ is given by

$$\boldsymbol{t}(\hat{\boldsymbol{n}}) = \lim_{\Delta A \to 0} \frac{\Delta \boldsymbol{F}}{\Delta A} = \sigma^T \cdot \hat{\boldsymbol{n}} \tag{3.3}$$

where $\hat{\boldsymbol{n}} = (\boldsymbol{e}_1, \boldsymbol{e}_2, \boldsymbol{e}_3)$ and σ is the *infinitesimal stress tensor*, denoted by

$$[\boldsymbol{\sigma}] = \begin{pmatrix} \sigma_{11} & \sigma_{12} & \sigma_{13} \\ \sigma_{21} & \sigma_{22} & \sigma_{23} \\ \sigma_{31} & \sigma_{32} & \sigma_{33} \end{pmatrix} \tag{3.4}$$

For instance, the constraint $\boldsymbol{t}_3$ applied on the upper face of a cube may be written as

$$\boldsymbol{t}_3 = \sigma_{13}\boldsymbol{e}_1 + \sigma_{23}\boldsymbol{e}_2 + \sigma_{33}\boldsymbol{e}_3$$

This is illustrated by figure 3.4.

Because the infinitesimal strain and stress tensors only contain 6 independent components, they can be written as:

$$[\boldsymbol{\sigma}] = \begin{pmatrix} \sigma_1 \\ \sigma_2 \\ \sigma_3 \\ \sigma_4 \\ \sigma_5 \\ \sigma_6 \end{pmatrix} = \begin{pmatrix} \sigma_{11} \\ \sigma_{22} \\ \sigma_{33} \\ \sigma_{23} \\ \sigma_{31} \\ \sigma_{12} \end{pmatrix} \qquad [\boldsymbol{\epsilon}] = \begin{pmatrix} \epsilon_1 \\ \epsilon_2 \\ \epsilon_3 \\ \epsilon_4 \\ \epsilon_5 \\ \epsilon_6 \end{pmatrix} = \begin{pmatrix} \epsilon_{11} \\ \epsilon_{22} \\ \epsilon_{33} \\ 2\epsilon_{23} \\ 2\epsilon_{31} \\ 2\epsilon_{12} \end{pmatrix}$$

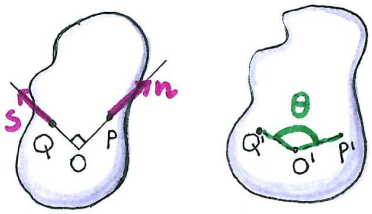

Figure 3.3: Left: body without deformation. Right: body under shear stress.

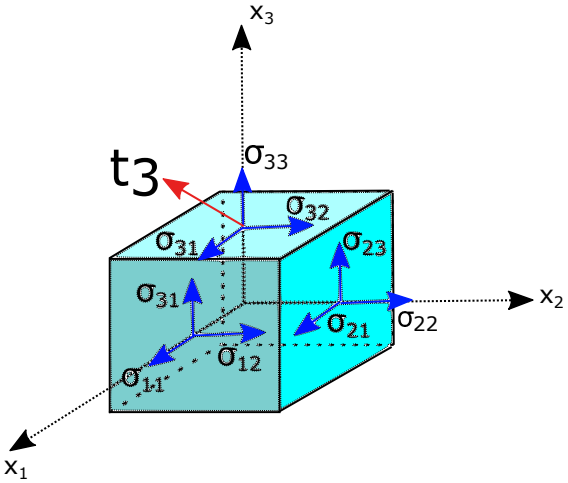

Figure 3.4: Constraint vector and tensor in a Cartesian basis.

3.1.2 Hooke's laws and engineering constants

In the case of small perturbations, there exist a linear relation linking the infinitesimal stress and strain tensors. This model is called the generalised Hooke's law.

In the most general case, Hooke's law can be written as

$$\sigma_{ij} = \sum_{k=1}^{3}\sum_{l=1}^{3} C_{ijkl}\epsilon_{kl} \qquad \epsilon_{ij} = \sum_{k=1}^{3}\sum_{l=1}^{3} S_{ijkl}\sigma_{kl}$$

where the stiffness tensor $\boldsymbol{C}$ and the compliance tensor $\boldsymbol{S}$ are fourth order tensors and contain 81 elements. Because $\boldsymbol{\epsilon}$ and $\boldsymbol{\sigma}$ are symmetric, the number of independent elements reduce to 36. Further symmetry can be found if we analyse the strain energy function per unit volume:

$$W(\boldsymbol{\epsilon}) = \frac{1}{2}\boldsymbol{\epsilon} : \boldsymbol{\sigma} = \frac{1}{2}\sum_{i=1}^{3}\sum_{j=1}^{3} \epsilon_{ij}\sigma_{ij}$$

In uni-dimensional case, this function is equal to $W(\epsilon) = \frac{1}{2}\epsilon\sigma = \frac{1}{2}\epsilon E\epsilon$ and represents the area under the stress-strain curve (see figure 3.5). The infinitesimal stress tensor can thus be expressed as

$$\boldsymbol{\sigma} = \frac{d}{d\boldsymbol{\epsilon}}\left(\frac{1}{2}\boldsymbol{\epsilon} : \boldsymbol{C} : \boldsymbol{\epsilon}\right)$$

and $C_{ijkl} = \frac{\partial^2}{\partial\epsilon_{ij}\partial\epsilon_{kl}} = \frac{\partial^2}{\partial\epsilon_{kl}\partial\epsilon_{ij}} = C_{klij}$. This reduce the number of independent elements of the stiffness tensor to 21. Hooke's law simply to $\sigma_i = \sum_{j=1}^{6} C_{ij}\epsilon_j$.

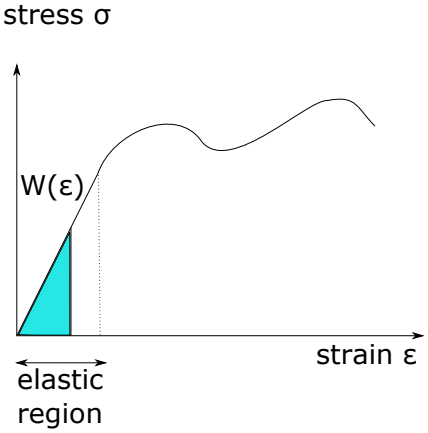

Figure 3.5: Stress -strain curve and strain energy function in the elastic region.

Orthotropic materials have 3 mutually perpendicular planes of material symmetry. For orthotropic materials, Hooke's law simplify to:

$$\begin{pmatrix}\sigma_1\\ \sigma_2\\ \sigma_3\\ \sigma_4\\ \sigma_5\\ \sigma_6\end{pmatrix} = \begin{pmatrix}C_{11} & C_{12} & C_{13} & 0 & 0 & 0\\ C_{12} & C_{22} & C_{23} & 0 & 0 & 0\\ C_{13} & C_{23} & C_{33} & 0 & 0 & 0\\ 0 & 0 & 0 & C_{44} & 0 & 0\\ 0 & 0 & 0 & 0 & C_{55} & 0\\ 0 & 0 & 0 & 0 & 0 & C_{66}\end{pmatrix}\begin{pmatrix}\epsilon_1\\ \epsilon_2\\ \epsilon_3\\ \epsilon_4\\ \epsilon_5\\ \epsilon_6\end{pmatrix} \tag{3.5}$$

The corresponding relation relating strain to stress is :

$$\begin{pmatrix}\epsilon_1\\ \epsilon_2\\ \epsilon_3\\ \epsilon_4\\ \epsilon_5\\ \epsilon_6\end{pmatrix} = \begin{pmatrix}S_{11} & S_{12} & S_{13} & 0 & 0 & 0\\ S_{12} & S_{22} & S_{23} & 0 & 0 & 0\\ S_{13} & S_{23} & S_{33} & 0 & 0 & 0\\ 0 & 0 & 0 & S_{44} & 0 & 0\\ 0 & 0 & 0 & 0 & S_{55} & 0\\ 0 & 0 & 0 & 0 & 0 & S_{66}\end{pmatrix}\begin{pmatrix}\sigma_1\\ \sigma_2\\ \sigma_3\\ \sigma_4\\ \sigma_5\\ \sigma_6\end{pmatrix}$$

Hooke's law for orthotropic material can be written in terms of engineering constants. The engineering constants (Young modulus, Poisson ratio and shear modulus) are defined in term of stresses and strains. Young's modulus E_i, in direction i, measures the stiffness of of a material:

$$E_i = \frac{\sigma_{ii}}{\epsilon_{ii}}$$

Poisson's coefficient ν_{ij} is the signed ratio of transverse strain ϵ_{jj} on axial strain ϵ_{ii}:

$$\nu_{ij} = -\frac{\epsilon_{jj}}{\epsilon_{ii}}$$

Shear modulus G_{ij} is the elasticity coefficient for shear or tension force:

$$G_{ij} = \frac{\sigma_{ij}}{2\epsilon_{ij}}$$

Therefore, the relation between strain and stress becomes:

$$\begin{pmatrix}\epsilon_1\\ \epsilon_2\\ \epsilon_3\\ \epsilon_4\\ \epsilon_5\\ \epsilon_6\end{pmatrix} = \begin{pmatrix}\frac{1}{E_1} & -\frac{\nu_{12}}{E_1} & -\frac{\nu_{13}}{E_1} & 0 & 0 & 0\\ -\frac{\nu_{12}}{E_1} & \frac{1}{E_2} & -\frac{\nu_{23}}{E_2} & 0 & 0 & 0\\ -\frac{\nu_{13}}{E_1} & -\frac{\nu_{23}}{E_2} & \frac{1}{E_3} & 0 & 0 & 0\\ 0 & 0 & 0 & \frac{1}{G_{23}} & 0 & 0\\ 0 & 0 & 0 & 0 & \frac{1}{G_{13}} & 0\\ 0 & 0 & 0 & 0 & 0 & \frac{1}{G_{12}}\end{pmatrix}\begin{pmatrix}\sigma_1\\ \sigma_2\\ \sigma_3\\ \sigma_4\\ \sigma_5\\ \sigma_6\end{pmatrix} \tag{3.6}$$

3.2 Macromechanics of a unidirectional ply

Unidirectional plies are orthotropic materials. They are assumed to be homogeneous and sufficiently thin that though-thickness stresses are zero:

$$\sigma_3 = \sigma_4 = \sigma_5 = 0$$

Law (3.6) becomes:

$$\begin{pmatrix}\epsilon_1\\ \epsilon_2\\ \epsilon_6\end{pmatrix} = \begin{pmatrix}S_{11} & S_{12} & 0\\ S_{12} & S_{22} & 0\\ 0 & 0 & S_{66}\end{pmatrix}\begin{pmatrix}\sigma_1\\ \sigma_2\\ \sigma_6\end{pmatrix} = \begin{pmatrix}\frac{1}{E_1} & -\frac{\nu_{12}}{E_1} & 0\\ -\frac{\nu_{12}}{E_1} & \frac{1}{E_2} & 0\\ 0 & 0 & \frac{1}{G12}\end{pmatrix}\begin{pmatrix}\sigma_1\\ \sigma_2\\ \sigma_6\end{pmatrix} \tag{3.7}$$

and law (3.5)

$$\begin{pmatrix}\sigma_1\\ \sigma_2\\ \sigma_6\end{pmatrix} = \begin{pmatrix}C_{11} & C_{12} & 0\\ C_{12} & C_{22} & 0\\ 0 & 0 & C_{66}\end{pmatrix}\begin{pmatrix}\epsilon_1\\ \epsilon_2\\ \epsilon_6\end{pmatrix} \tag{3.8}$$

with

$$C_{11} = \frac{S_{22}}{-S_{12}^2 + S_{11} * S_{22}}$$
$$C_{12} = -\frac{S_{12}}{-S_{12}^2 + S_{11} * S_{22}}$$
$$C_{22} = \frac{S_{11}}{-S_{12}^2 + S_{11} * S_{22}}$$
$$C_{66} = \frac{1}{S_{66}}$$

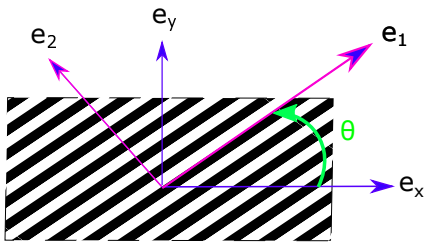

Figure 3.6: Ply in a rotated coordinate systems.

Because laminates are usually made of plies stacked with different angles, it is necessary to express laws (3.7) (3.8) when the fibre direction form an angle θ with e_1. The new coordinate system is represented in figure 3.6. Stresses in the old and new coordinate system are related by

$$\begin{pmatrix}\sigma_1\\ \sigma_2\\ \sigma_6\end{pmatrix} = \begin{pmatrix}c^2 & s^2 & 2sc\\ s^2 & c^2 & -2sc\\ -sc & sc & c^2 - s^2\end{pmatrix}\begin{pmatrix}\sigma_x\\ \sigma_y\\ \sigma_{xy}\end{pmatrix}$$

$$\begin{pmatrix}\epsilon_1\\ \epsilon_2\\ \epsilon_6\end{pmatrix} = \begin{pmatrix} c^2 & s^2 & sc \\ s^2 & c^2 & -sc \\ -2sc & 2sc & c^2-s^2\end{pmatrix}\begin{pmatrix}\epsilon_x\\ \epsilon_y\\ \epsilon_{xy}\end{pmatrix}$$

with $c = \cos(\theta)$ and $s = \sin(\theta)$.

3.3 Micromechanics of a unidirectional ply

The previous section studied Hooke's law for a homogenised bi-dimensional ply. The stress-strain relation only depends on 4 engineering constants E_1, E_2, ν_{12} and G_{12}. The rule of mixtures determines those constants on a representative volume element. A *representative volume element* (RVE) is the smallest volume which is statistically representative of the composite material (it includes a sampling of all micro structural heterogeneities occurring in the material) [24]. The coefficients are computed based on the properties of the fibres, the matrix and on FVF under the following assumptions:

- the material is free of voids
- the fibres and the matrix are homogeneous, linear elastic and isotropic elements
- fibres are continuous, parallel and the space between fibres is uniform
- perfect bound between the matrix and the fibres

Let $V_f = \frac{V_{fibre}}{V_{tot}}$ the fibre volume fraction with V_{fibre} the volume of fibre in the RVE and V_{tot} the total volume of the RVE, E_i, ν_i and G_i respectively the Young modulus, the Poisson ratio and the shear modulus of material $i = \{f, m\}$ with f the fibre and m the matrix. The rule of mixture states that:

$$\begin{aligned} E_1 &= E_f V_f + E_m(1-V_f) \\ E_2 &= \left(\frac{V_f}{E_f} + \frac{(1-V_f)}{E_m}\right)^{-1} \\ \nu_{12} &= V_f\nu_f + (1-V_f)\nu_m \\ G_{12} &= \left(\frac{V_f}{G_f} + \frac{1-V_f}{G_m}\right)^{-1} \end{aligned}$$

The proof can be found in appendix A.

This section has allowed to homogenize the different constituents of the composite materials into a continuous material and has explained how to determine the engineering constants of the homogeneous material depending on those of its components. The homogenised plies are components of the final laminate structure.

3.4 Macromechanics of a laminate

This section focusses on the Classical Lamination Theory (CLT). Based on the mechanical properties of the plies and the angles of the plies with respect to the main axes, the CLT predicts the mechanical properties and responses of a laminate shown with its axis coordinate system $(\boldsymbol{e}_x, \boldsymbol{e}_y, \boldsymbol{e}_z)$ on figure 3.7.

The plane Oxy is set on the mid-surface of the laminate. The CLT makes the following hypothesis: displacements are continuous and small along axis $\boldsymbol{e}_z$, the laminate is only loaded in its plane (σ_{xz}, σ_{yz}, σ_{zz} are negligible with respect to σ_x, σ_y, σ_{xy}) and a straight perpendicular line to the mid-surface remains straight, perpendicular and of same length after deformation ($\epsilon_{xz} = \epsilon_{yz} = \epsilon_z = 0$).
Denoting $\mathtt{u}_0$, $\mathtt{v}_0$ and $\mathtt{w}_0$ the displacements on the mid-surface in directions $\boldsymbol{e}_x$, $\boldsymbol{e}_y$ and $\boldsymbol{e}_z$ and $\mathtt{u}$, $\mathtt{v}$ and $\mathtt{w}$ the displacements in directions $\boldsymbol{e}_x$, $\boldsymbol{e}_y$ and $\boldsymbol{e}_z$, the goal is to determine displacements and deformations inside the laminate as a function of displacements and deformations on the mid-surface. Fix a point $\boldsymbol{C}$ situated outside the mid-surface of the laminate and perpendicular to a point $\boldsymbol{B}$ located on the mid-surface. The two points are separated by a distance z. After deformation, segment $\boldsymbol{BC}$ form an angle α with respect to the normal of the Oxy plane. The laminate is shown before and after deformation on figure 3.8.

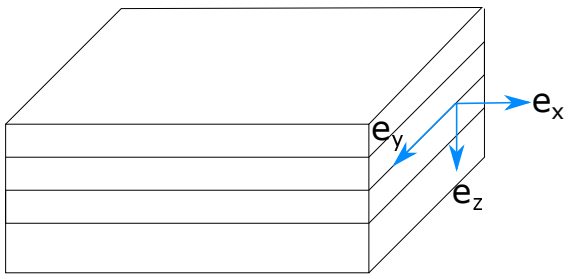

Figure 3.7: Laminate structure and coordinate system.

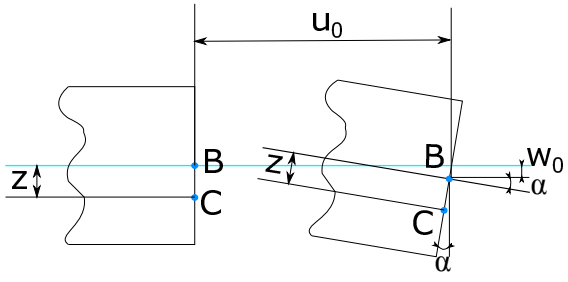

Figure 3.8: Laminate deformation in the Oxy plane.

Denoting the strains of the mid-surface by

$$\boldsymbol{\epsilon}_0 = \begin{pmatrix}\epsilon_x^0 & \epsilon_y^0 & 2\epsilon_{xy}^0\end{pmatrix}^T = \begin{pmatrix}\frac{\partial \mathtt{u}_0}{\partial x} & \frac{\partial \mathtt{v}_0}{\partial y} & \frac{\partial \mathtt{u}_0}{\partial y} + \frac{\partial \mathtt{v}_0}{\partial x}\end{pmatrix}^T$$

the mid-plane curvatures by

$$\boldsymbol{\kappa} = \begin{pmatrix}\kappa_x & \kappa_y & \kappa_{xy}\end{pmatrix}^T = \begin{pmatrix}-\frac{\partial^2 \mathtt{w}_0}{\partial x^2} & -\frac{\partial^2 \mathtt{w}_0}{\partial y^2} & -2\frac{\partial^2 \mathtt{w}_0}{\partial x \partial y}\end{pmatrix}^T$$

and the strains inside the laminate by

$$\boldsymbol{\epsilon} = \begin{pmatrix}\epsilon_x & \epsilon_y & 2\epsilon_{xy}\end{pmatrix}^T$$

the strains can be expressed as

$$\boldsymbol{\epsilon}(x,y,z) = \boldsymbol{\epsilon_0}(x,y) + z\boldsymbol{\kappa}(x,y)$$

The strain stress relation of a ply k with stiffness matrix $\boldsymbol{C}_k$ (in local axis $\boldsymbol{e}_x$ and $\boldsymbol{e}_y$) is given by

$$\boldsymbol{\sigma}_k(x,y,z) = \boldsymbol{C}_k\boldsymbol{\epsilon_0}(x,y) + z\boldsymbol{C}_k\boldsymbol{\kappa}(x,y)$$

Given a n ply laminate of thickness h, the resultant forces per unit length $\boldsymbol{N}(x,y)$ and the resultant moments $\boldsymbol{M}(x,y)$ are given by

$$\begin{pmatrix} \boldsymbol{N} \\ \boldsymbol{M} \end{pmatrix} = \begin{pmatrix} \boldsymbol{P} & \boldsymbol{Q} \\ \boldsymbol{Q} & \boldsymbol{R} \end{pmatrix} \begin{pmatrix} \boldsymbol{\epsilon}_0 \\ \boldsymbol{\kappa} \end{pmatrix} \tag{3.9}$$

with

$$P_{ij} = \sum_{k=1}^{n} (C_{ij})_k (h_k - h_{k-1})$$

$$Q_{ij} = \frac{1}{2}\sum_{k=1}^{n} (C_{ij})_k (h_k^2 - h_{k-1}^2)$$

$$R_{ij} = \frac{1}{3}\sum_{k=1}^{n} (C_{ij})_k (h_k^3 - h_{k-1}^3)$$

for $i,j = 1,2,6$. Furthermore, $h_k = -\frac{h}{2} + \sum_{u=1}^{k} t_u$ for $k = 1,...,n$ and $h_0 = -\frac{h}{2}$ with t_k the thickness of ply k and $\sum_{u=1}^{n} t_u = h$. The whole development can be found in appendix B. Knowing the forces and moment applied allow to compute the curvatures and strains of the mid-surface. Once the curvatures and strains are known, they can be plugged in to evaluate the strains and stress at any point in the laminate.

If the stresses applied on the object become too large, the composite objects might be damaged or break. It is important to predict when this might happen to design composite materials and use them safely afterwards.

3.5 Failure and damage mechanisms

Failure can occur in composite due to breakage of the fibres, of the matrix, of the link between the fibres or due to delamination between the different plies. Tsai-Wu is a failure criterion which generalises the Von Mises criterion, used to predict the damage point of isotropic material, to anisotropic materials. Tsai-Wu predicts failure when

$$\sum_{i=1}^{6} F_i\sigma_i + \sum_{i=1}^{6}\sum_{j=1}^{6} F_{ij}\sigma_i\sigma_j = 1$$

with F_{ij} fourth order rank tensor and F_i second order rank tensor [9].

Let's first consider a ply under plane stress. Tsai-Wu criterion becomes

$$F_1\sigma_1 + F_2\sigma_2 + F_6\sigma_6 + F_{11}\sigma_1^2 + F_{22}\sigma_2^2 + F_{66}\sigma_6^2 + 2F_{12}\sigma_1\sigma_2 = 1$$

where parameters F_i and F_{ij} can be expressed using the five strength parameters of the unidirectional ply. First apply traction along the direction of fibres until the material reaches failure. Letting $(\sigma_1^T)_{failure} > 0$ the stress at failure, the failure criterion becomes

$$F_1(\sigma_1^T)_{failure} + F_{11}(\sigma_1^T)_{failure}^2 = 1 \tag{3.10}$$

Apply compression in the direction of the fibres until the material reaches failure. Letting $-(\sigma_1^C)_{failure}$ the stress at failure, the failure criterion becomes

$$-F_1(\sigma_1^C)_{failure} + F_{11}(\sigma_1^C)_{failure}^2 = 1 \tag{3.11}$$

Solving equations (3.10) and (3.11) in terms of F_1 and F_{11} gives

$$F_1 = \frac{1}{(\sigma_1^T)_{failure}} - \frac{1}{(\sigma_1^C)_{failure}} \qquad F_{11} = \frac{1}{(\sigma_1^T)_{failure}(\sigma_1^C)_{failure}}$$

Similarly, letting $(\sigma_2^T)_{failure}$ and $-(\sigma_2^C)_{failure}$ respectively the traction and compression stresses in direction $\boldsymbol{e}_y$ at rupture, F_2 and F_{22} can be expressed as

$$F_2 = \frac{1}{(\sigma_2^T)_{failure}} - \frac{1}{(\sigma_2^C)_{failure}} \qquad F_{22} = \frac{1}{(\sigma_2^T)_{failure}(\sigma_2^C)_{failure}}$$

Apply pure shear stress until the material reaches failure. Letting $(\sigma_6)_{failure} > 0$ the shearing stress at failure, the failure criterion becomes

$$F_6(\sigma_6)_{failure} + F_{66}(\sigma_6)_{failure}^2 = 1 \tag{3.12}$$

Then apply the opposite shear stress until the material reaches failure. Letting $-(\sigma_6)_{failure}$ the shearing stress at failure, the failure criterion becomes

$$-F_6(\sigma_6)_{failure} + F_{66}(\sigma_6)_{failure}^2 = 1 \tag{3.13}$$

Solving equations (3.12) and (3.13) in terms of F_6 and F_{66} gives

$$F_6 = 0 \qquad\qquad F_{66} = \frac{1}{S_6^2}$$

In order to determine F_{12}, apply equal tensile loads along the two material axes until the material reaches failure. Letting $\sigma_1 = \sigma_2 = S$ the stresses at failure, the failure criterion becomes

$$(F_1 + F_2)S + (F_{11} + F_{22} + 2F_{12})S^2 = 1 \tag{3.14}$$

After replacing F_1, F_2, F_{11} and F_{22} by their expression, equation (3.14) becomes

$$F_{12} = \frac{1}{2S^2} - \frac{1}{2S}\left(\frac{1}{(\sigma_1^T)_{failure}} - \frac{1}{(\sigma_1^c)_{failure}} + \frac{1}{(\sigma_2^T)_{failure}} - \frac{1}{(\sigma_2^C)_{failure}}\right) - \frac{1}{2}\left(\frac{1}{(\sigma_1^T)_{failure}(\sigma_1^C)_{failure}} + \frac{1}{(\sigma_2^T)_{failure}(\sigma_2^C)_{failure}}\right)$$

A laminate is made of several plies. Once the laminate is loaded, some of its plies may fail. Once a ply has failed, the stiffness and strength properties of the ply decrease. The stress-strain diagram of the laminate can be estimated in several steps. First, the loads are applied to the laminate and the local strains and stresses are computed inside each ply. The Tsai-Wu criterion allow to estimate whether the ply has failed. If the ply has failed, its stiffness and strength decrease and some loads are transferred to the other plies. Increasing the loads until all ply have failed allow to plot the stress-strain curve of the laminate.

This chapter has highlighted the effect of the FVF on the mechanical properties of a ply. It has also expressed the dependence of the angle of the ply on the stiffness and compliance matrices. Finally, the Tsai-Wu criterion has been presented and expressed for a ply. A way to compute failure has been presented for the whole laminate, taking into account the Tsai-Wu criterion of the plies. Until now, all properties have been considered constant. In real life applications, this is not the case. The next chapter explains how to model variabilities.

Chapter 4

Modelling uncertainties

The manufacturing of composites is subject to many uncertainties impacting their properties (fibre volume fraction, voids, fibre orientations...) which, in turn, affect the mechanical responses. Those properties are usually modelled using second order random fields and used afterwards in structure analysis. For instance, FVF fields and fibre orientations are modelled using a normal distribution respectively in [13, 58] and [38, 52, 39] while articles [38, 10] states that local permeability follow a log normal distribution.

This chapter defines second order random fields, explains how to model them using expansions and how to numerically represent them based on Galerkin projection method.

4.1 Definition and modelling of random fields

Consider $\Omega \subset \mathbb{R}^3$ a computation field (for instance, the surface of the composite object) and a probability space $(\Theta, \mathcal{F}, \mathbb{P})$. A mechanical property which is spatially distributed over Ω may be modelled using a second order random process.

A *second order random process* $u(\boldsymbol{x}, \theta)$ is a set of random variables on a probability space $(\Theta, \mathcal{F}, \mathbb{P})$ such that

$$u(\boldsymbol{x}, \cdot) \in \mathcal{L}^2(\Theta \times \Omega) \Leftrightarrow E[u^2] < \infty$$

and $\forall \boldsymbol{x} \in \Omega$, $u(\boldsymbol{x}, \cdot) : \Theta \to \mathbb{R}$ is a random variable. Any second order random process can be decomposed as

$$u(\boldsymbol{x}, \theta) = \bar{u}(\boldsymbol{x}) + u_0(\boldsymbol{x}, \theta)$$

with $E[u(\boldsymbol{x}, \theta)] = \bar{u}(\boldsymbol{x})$ and $u_0(\boldsymbol{x}, \theta)$ a zero mean random process.
$u(\boldsymbol{x}, \theta)$ is completely determined by its mean value $\bar{u}(\boldsymbol{x})$ and its covariance function $C(\boldsymbol{x}, \boldsymbol{y})$. The covariance function gives the effect of $u(\boldsymbol{x}, \theta)$ on its neighbourhood, links the deviations of the random field at $\boldsymbol{x}$ and $\boldsymbol{y}$ and describes the variation of $u(\boldsymbol{x}, \theta)$ about its mean value $\bar{u}(\boldsymbol{x})$.
Many covariance functions decrease monotonously with respect to the geodesic distance between $\boldsymbol{x}$ and $\boldsymbol{y}$. The *geodesic path* between two points on a composite is the shortest path on a curve belonging to the surface of the object. Covariance functions decreasing with the geodesic distance between $\boldsymbol{x}$ and $\boldsymbol{y}$ can reflect the fact that a mechanical property at a point $\boldsymbol{x}$ will probably be more similar to the same mechanical property of a point $\boldsymbol{y}$ that is close to $\boldsymbol{x}$ than at a point $\boldsymbol{y}$ that is far from $\boldsymbol{x}$. Covariance functions may be isotropic or anisotropic. An *isotropic function* $f_{iso}(\boldsymbol{x}, \boldsymbol{y})$ is a function which does not depend on the direction in which it is evaluated, it is invariant under rotation. More formally, an isotropic function possess the following property:

$$f_{iso}(\boldsymbol{x}, \boldsymbol{y}) = f(\boldsymbol{Q}\boldsymbol{x}, \boldsymbol{Q}\boldsymbol{y})$$

for any orthogonal matrix $\boldsymbol{Q}$. A function which is not isotropic is called *anisotropic*. Isotropic covariance functions model isotropic uncertainties such as FVF when fibres are randomly oriented in the plane. Anisotropic covariance functions model anisotropic uncertainties such as fibre orientations [52]. For instance, one can choose the following covariance function :

$$C(\boldsymbol{x}, \boldsymbol{y}) = \begin{cases} \sigma^2 \left(1 - \frac{d(\boldsymbol{x}, \boldsymbol{y})}{l_{c,Cov}}\right)^2 & \text{if } d(\boldsymbol{x}, \boldsymbol{y}) < l_{c,Cov} \\ 0 & \text{else} \end{cases}$$

with $d(\boldsymbol{x}, \boldsymbol{y})$ the isotropic or anisotropic geodesic distance between $\boldsymbol{x}$ and $\boldsymbol{y}$ and $l_{c,Cov}$ the covariance characteristic length.

Now that the field is totally defined, the goal is to discretise it on the composite surface.

4.2 Karhunen-Loève expansion

Karhunen-Loève expansion states that any second order Gaussian random process is a convergent infinite series

$$u(\boldsymbol{x}, \theta) = \bar{u}(\boldsymbol{x}) + \sum_{i=1}^{\infty} \sqrt{\lambda_i} \xi_i(\theta) \phi_i(\boldsymbol{x})$$

with $\xi_i(\theta)$ standard normal uncorrelated variables, $\lambda_i \in [0, \infty)$ and $\phi_i(\boldsymbol{x}) : \Omega \to \mathbb{R}$ the eigenvalues and eigenfunctions obtained by solving the Fredholm integral equation of the second kind

$$\int_\Omega C(\boldsymbol{x}, \boldsymbol{y})\phi_i(\boldsymbol{y})d\boldsymbol{y} = \lambda_i \phi_i(\boldsymbol{x}) \tag{4.1}$$

with $C(\boldsymbol{x}, \boldsymbol{y})$ the covariance function associated with the random field [21, 4, 33].
Let $C(\boldsymbol{x}, \boldsymbol{y}) : D \times D \to \mathbb{R}$ denote a continuous, symmetric, positive definite and real-valued function. Then, by definition, for any set of points $\boldsymbol{x}_i$ and $\boldsymbol{y}_i$, $C(\boldsymbol{x}, \boldsymbol{y})$ is such that

$$\sum_{i,j=1}^{N} a_i a_j C(\boldsymbol{x_i}, \boldsymbol{x_j}) \geq 0$$

for N finite, $x_i \in \Omega$ and $a_i \in \mathbb{R}$ $(i = 1, ..., N)$. Furthermore, if $C(x, y)^2$ is a *square-integrable function* :

$$\int_\Omega \int_\Omega C(\boldsymbol{x}, \boldsymbol{y})^2 d\mu(\boldsymbol{x})d\mu(\boldsymbol{y}) < \infty$$

Then C can be expressed by the converging series

$$C(\boldsymbol{x}, \boldsymbol{y}) = \sum_{k=1}^{\infty} \lambda_k \phi_k(\boldsymbol{x})\phi_k(\boldsymbol{y}) \tag{4.2}$$

where $\int_\Omega \phi_i(\boldsymbol{x})\phi_j(\boldsymbol{x})d\boldsymbol{x} = \delta_{ij}$ ($\delta_{ij} = 1$ if $i = j$ and $\delta_{ij} = 0$ if $i \neq j$). The eigenvalues and eigenfunctions in equation (4.2) can be found by solving equation (4.1) [30, 25, 37]. For some covariance functions, an analytical solution exists.

4.2.1 Analytical resolution of two classical examples

The random field described by the covariance function

$$C(x_1, x_2) = \sigma^2 e^{-\frac{|x_1 - x_2|}{b}} \tag{4.3}$$

defined on the domain $[-a; a]$ with $a = \frac{1}{2}$ and $b \neq 0$, can be expressed as infinite series by solving equation (4.1) analytically. The eigenvalues and functions are given by

$$\lambda_i = \frac{2\sigma^2 c}{c^2 + \omega_i^2} \qquad \phi_i(x) = \frac{\cos(\omega_i x)}{\sqrt{a + \frac{\sin(2\omega_i a)}{2\omega_i}}} \qquad c - \omega \tan(\omega a) = 0$$

and

$$\lambda_i = \frac{2\sigma^2 c}{c^2 + \omega_i^2} \qquad \phi_i(x) = \frac{\sin(\omega_i x)}{\sqrt{a - \frac{\sin(2\omega_i a)}{2\omega_i}}} \qquad \omega + c \tan(\omega a) = 0$$

for $c = \frac{1}{b}$ and $i = 1, 2, ...$ [55]. The covariance function and its associated eigenvalues and functions are shown on figures 4.1 and 4.2 for $b = \sigma = 1$. Small eigenvalues correspond to eigenfunctions with high frequencies. The influence of the eigenfunction on the series is weighted by the corresponding eigenvalue. Therefore, eigenfunctions corresponding to small eigenvalues do not influence much the series. As shown on figure 4.3, the large eigenvalues give the general trend of the field while small eigenvalues allow to simulate the rapid and small changes observed in experimental data.

Analytical solutions also exist in bi-dimensional cases. For example, the random field described by the covariance function

$$C(x_1, y_1, x_2, y_2) = \sigma^2 e^{-\frac{|x_1 - x_2|}{b_x}} e^{-\frac{|y_1 - y_2|}{b_y}}$$

defined on the domain $[-\frac{l_x}{2}; \frac{l_x}{2}] \times [-\frac{l_y}{2}; \frac{l_y}{2}]$ with $b_x \neq 0$ and $b_y \neq 0$, can be expressed as infinite series by solving equation equation (4.1) analytically:

$$\lambda_n \phi_n(x_1, y_1) = \int_{-\frac{l_x}{2}}^{\frac{l_x}{2}} \int_{-\frac{l_y}{2}}^{\frac{l_y}{2}} C(x_1, x_2, y_1, y_2)\phi_n(x_2, y_2)dx_1 dy_1 \tag{4.4}$$

Assuming the eigenfunctions and values solution of equation (4.4) are separable,

$$\phi_n(x_1, y_1) = \phi_i^{(x)}(x_1)\phi_j^{(y)}(y_1)$$
$$\lambda_n = \lambda_i^{(x)}\lambda_j^{(y)}$$

where the $\lambda_i^{(x)}, \lambda_j^{(y)}, \phi_i^{(x)}(x_1)$ and $\phi_j^{(y)}(y_1)$ are obtained as solutions of equation (4.1) expressed in terms of the covariance function (4.3). Some eigenvalues and weighted eigenfunctions are shown on figure 4.4. As in the one-dimensional case, adding terms to the expansion adds smaller variations with higher frequencies (see figure 4.5).

However, for many covariance functions, the Fredholm equation (4.1) can not frequently be solved analytically. The Galerkin projection method allows to solve the Fredholm equation numerically.

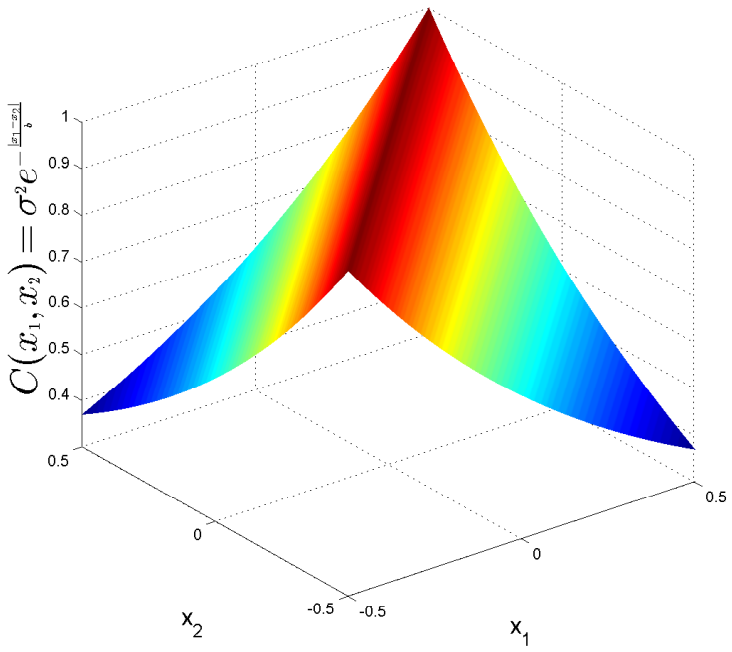

Figure 4.1: Covariance function $C(x_1, x_2) = \sigma^2 e^{-\frac{|x_1 - x_2|}{b}}$ with $b = 1$ and $\sigma = 1$

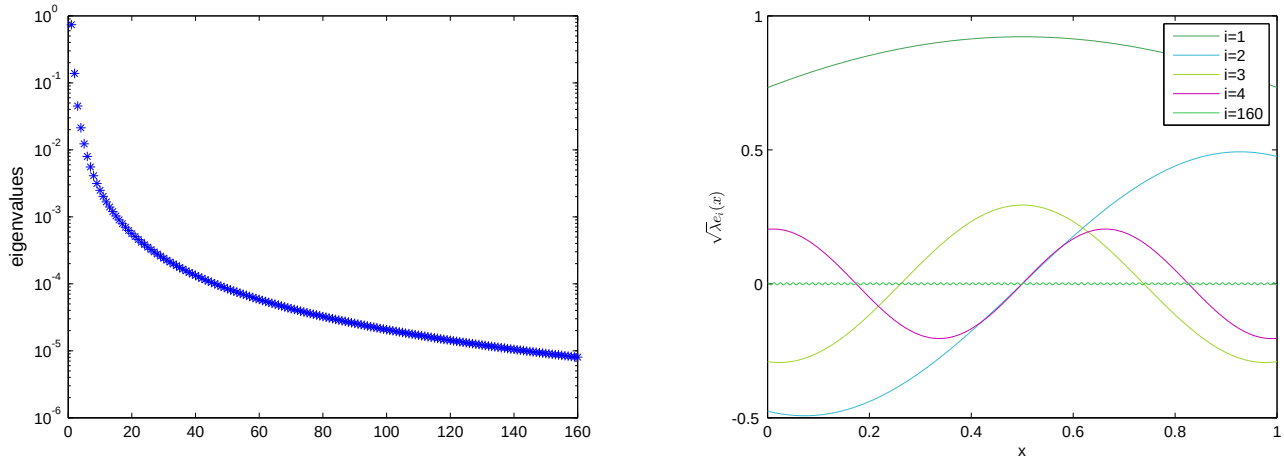

(a) First 160 eigenvalues.

(b) First 160 eigenfunctions.

Figure 4.2: Eigenvalues and eigenfunctions obtained by analytically solving the Fredholm equation using the covariance function $C(x_1, x_2) = \sigma^2 e^{-\frac{|x_1 - x_2|}{b}}$ with $b = 1$ and $\sigma = 1$.

4.3 Galerkin projection method

To solve the Fredholm equation numerically, the 3D surface is meshed with finite elements (triangles) and an approximation of the Fredholm equation is obtained using the Galerkin projection method [21, 4, 57]. The created *mesh* Ω_h is a set of *elements* Ω^e, in our case triangles, covering the surface Ω. The vertex of the elements are called *nodes*. The sides of the elements are called *edges*.

Let $h_j(\boldsymbol{x}) \in \mathcal{L}^2(\Omega_h)$ a square integrable function over the mesh. For instance, $h_j(\boldsymbol{x})$ can be a constant function by element equal to one over element j of Ω_h and zero elsewhere. It might also be a linear function by element equal to one on a node j of Ω_h and zero on the other nodes. Let's define $\mathcal{V}_h \subset \mathcal{L}^2(\Omega_h)$ as the set of shape functions associated with the mesh and N its dimension. The Fredholm equation of the second kind becomes:

$$\int_{\Omega_h} C(\boldsymbol{x}, \boldsymbol{y}) \hat{\phi}_i(\boldsymbol{y}) d\boldsymbol{y} = \hat{\lambda}_i \hat{\phi}_i(\boldsymbol{x})$$

where $\phi_i(\boldsymbol{x}) \approx \hat{\phi}_i(\boldsymbol{x}) = \sum_{j=1}^{N} d_j^i h_j(\boldsymbol{x})$ (d_j being the coordinates of $\hat{\phi}(\boldsymbol{x})$ in $\mathcal{V}_h$) and $\hat{\lambda}_i$ is the eigenvalue associated with $\hat{\phi}_i(\boldsymbol{x})$. Due

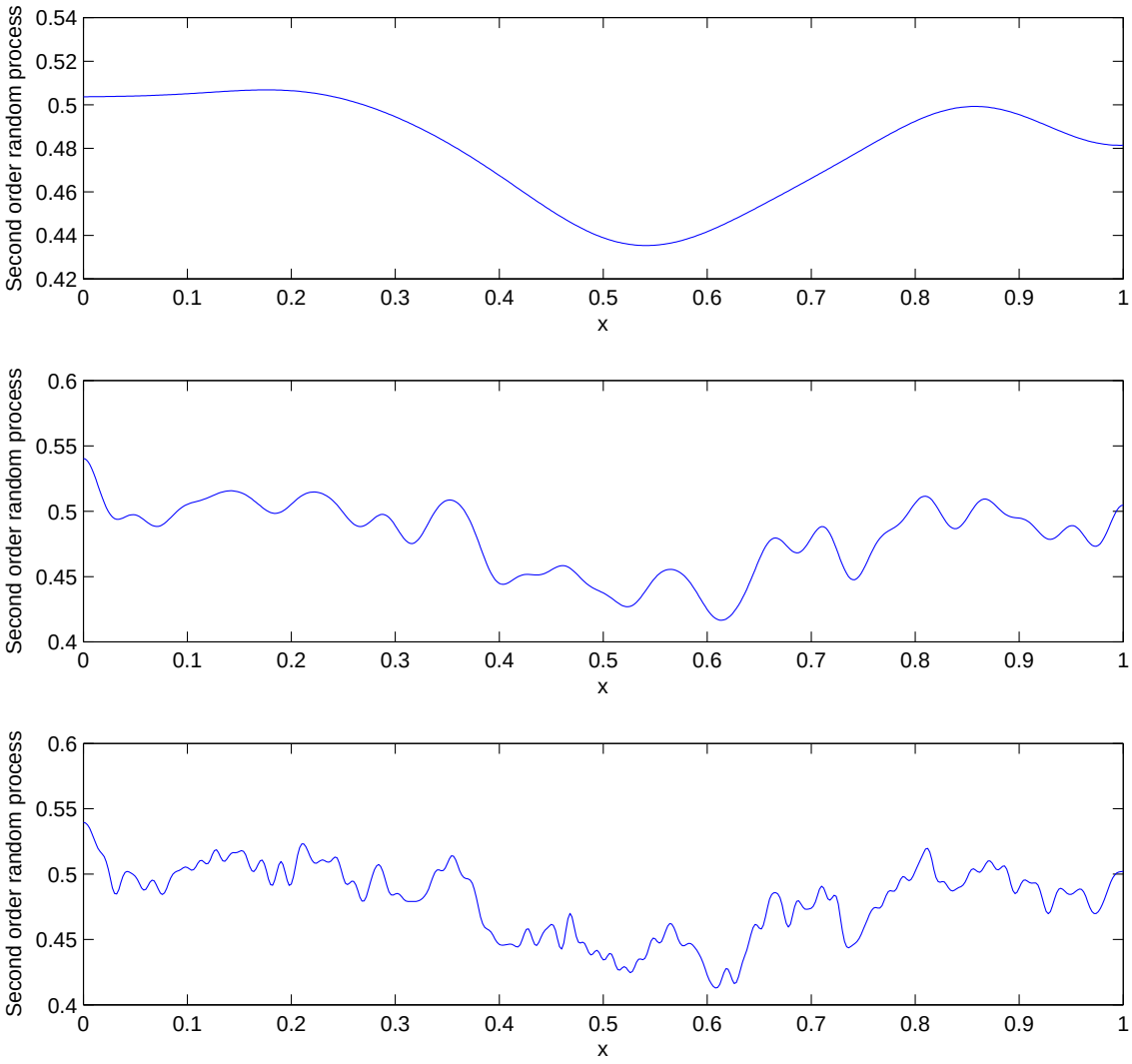

Figure 4.3: Second order random field with covariance function $C(x_1, x_2) = \sigma^2 e^{-|x_1 - x_2|}$ with $b = 1$ and $\sigma = 1$. Up to down, the largest 10, 50 and 160 eigenvalues are used to compute the field.

to the discretization, the solution of equation (4.1) will be an approximation of the exact solution. The residual r is given by:

$$r(\boldsymbol{x}) = \sum_{j=1}^{N} d_j^i \left(\int_\Omega Cov(\boldsymbol{x}, \boldsymbol{x}') h_j(\boldsymbol{x}') d\boldsymbol{x}' - \hat{\lambda}_i h_j(\boldsymbol{x}) \right)$$

In Gallerkin method, coefficients d_j^i are chosen such that the residual becomes orthogonal to the subspace of $L^2(\Omega)$ spanned by the basis functions $\{h_j\}_{j=1}^N$, meaning

$$\int_\Omega r(\boldsymbol{x}) h_j(\boldsymbol{x}) dx = 0 \quad \forall j = 1, ..., N$$

In matrix notation, this equation can be written as $\boldsymbol{A}\boldsymbol{d} = \lambda \boldsymbol{B}\boldsymbol{d}$ with

$$A_{i,j} = \int_\Omega h_i(\boldsymbol{x}) \int_\Omega C(\boldsymbol{x}, \boldsymbol{y}) h_j(\boldsymbol{y}) d\boldsymbol{y} d\boldsymbol{x} \qquad B_{i,j} = \int_\Omega h_i(\boldsymbol{x}) h_j(\boldsymbol{x}) d\boldsymbol{x} \tag{4.5}$$

Function $C(\boldsymbol{x}, \boldsymbol{y})$ is symmetric and positive definite. Therefore, matrix $\boldsymbol{A}$ is symmetric and positive definite. Some possible covariance functions are given in [46]. In order to reduce computation times, one may choose a covariance function such that the covariance function becomes zero when the distance between its two points gets greater than the covariance characteristic length.
Using a quadrature rule, the integrals (4.5) can be expressed as :

$$A_{i,j} = \sum_{p=1}^{Q} \sum_{q=1}^{Q} w_p w_q C(\boldsymbol{x}_p, \boldsymbol{x}_q) h_i(\boldsymbol{x}_p) h_j(\boldsymbol{x}_q) \qquad B_{i,j} = \sum_{p=1}^{Q} w_p h_i(\boldsymbol{x}_p) h_j(\boldsymbol{x}_p) \tag{4.6}$$

where w_p and w_q are some weights and $\boldsymbol{x}_p$ and $\boldsymbol{x}_q$ are some quadrature points. Let's give two examples of quadrature rules. For instance, on may take the barycentre of the triangle as quadrature point. Another possible solution is to choose quadrature points shown on figure 4.6(a).

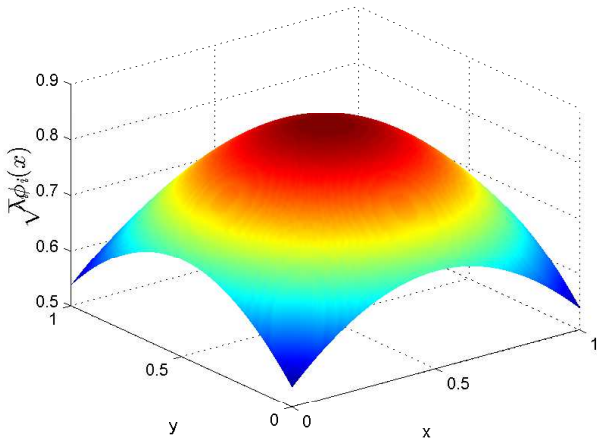

(a) First weighed eigenfunction.

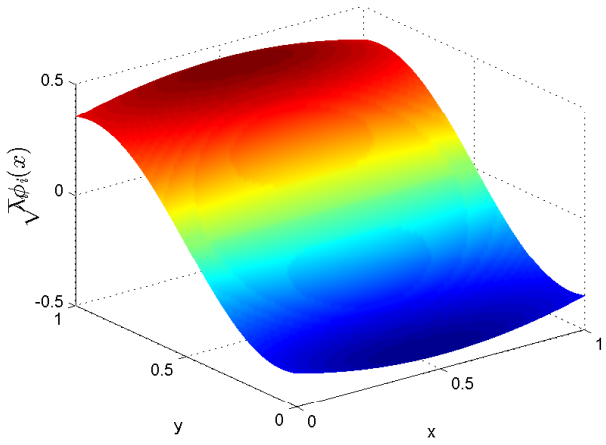

(b) Second weighed eigenfunction.

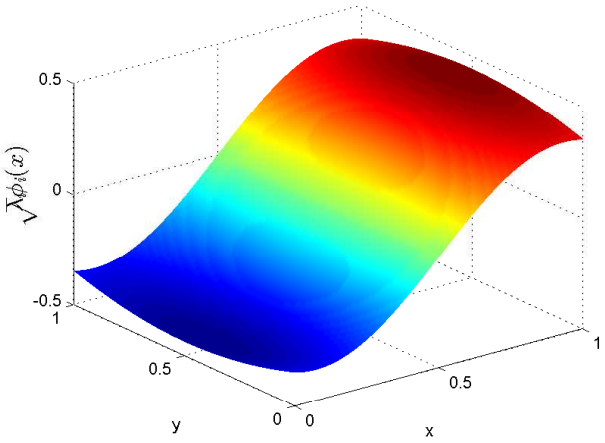

(c) Third weighed eigenfunction.

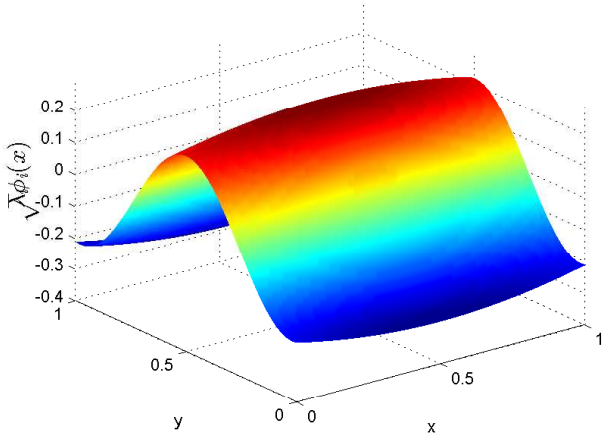

(d) Fourth weighed eigenfunction.

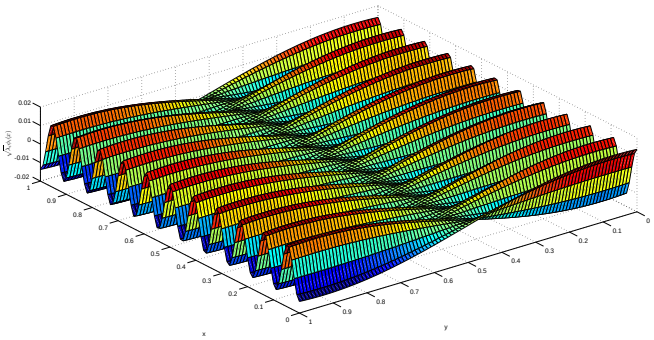

(e) 160^{th} weighed eigenfunction.

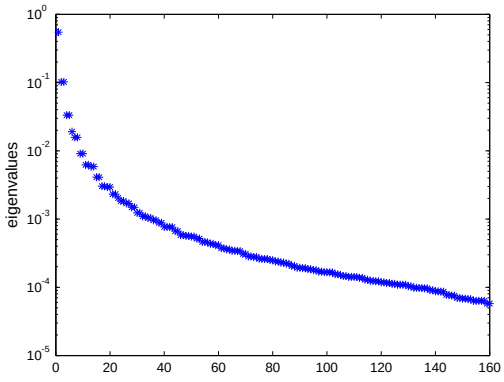

(f) 160 first eigenvalues.

Figure 4.4: Eigenvalues and eigenfunctions obtained by solving analytically the Fredholm equation using the covariance function $C(x_1, y_1, x_2, y_2) = \sigma^2 e^{-\frac{|x_1 - x_2|}{b_x}} e^{-\frac{|y_1 - y_2|}{b_y}}$ $b_x = b_y = 1$ and $\sigma = 1$.

Further details about basis functions and the aforementioned quadrature rules can be found in Appendix C. The quadrature points of figure 4.6(a) are chosen to refine the mesh. Distance computation methods will estimate distances on the refined mesh (see figure 4.6(b)). The quality of the new mesh is comparable to the quality of the old mesh as the new triangles are similar to the initial triangle.

Once equation $\boldsymbol{Ad} = \lambda \boldsymbol{Bd}$ is solved and the eigenvalues and eigenfunctions are computed, the second order random field can be approximated by :

$$\hat{u}(\boldsymbol{x}, \theta) = \bar{u}(\boldsymbol{x}) + \sum_{i=1}^{N} \sqrt{\hat{\lambda}_i} \hat{\phi}_i(\boldsymbol{x}) \xi_i(\theta)$$

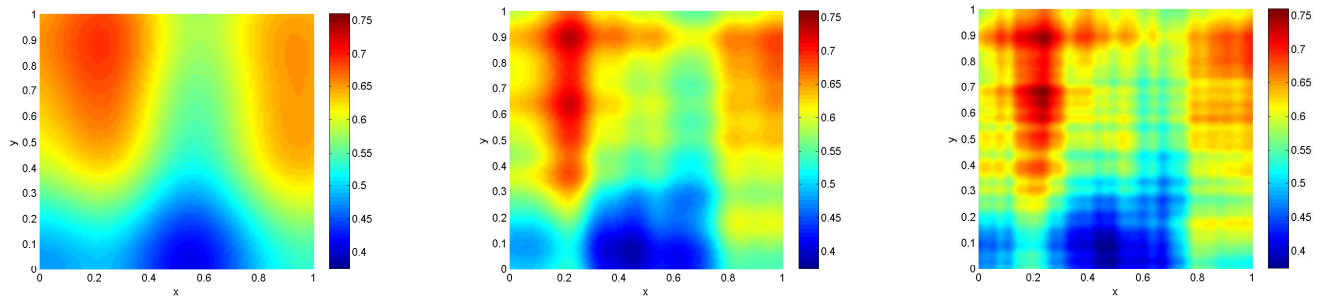

(a) Random field expansion with 10 terms.

(b) Random field expansion with 50 terms.

(c) Random field expansion with 160 terms.

Figure 4.5: Second order 2D random field with covariance function $C(x_1, y_1, x_2, y_2) = \sigma^2 e^{-\frac{|x_1-x_2|}{b_x}} e^{-\frac{|y_1-y_2|}{b_y}}$ with $b_x = b_y = 1$ and $\sigma = 1$.

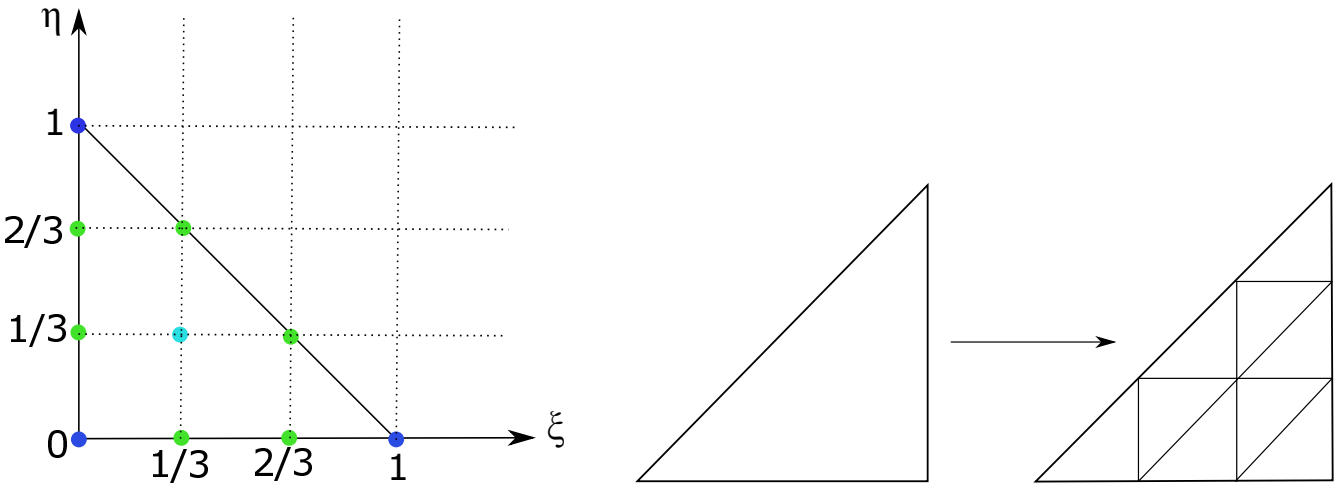

(a) The light blue point is the quadrature point for the one-point quadrature rule. The ten points are used as quadrature points for the ten-points quadrature rule.

(b) Procedure to refine the mesh

Figure 4.6: Refining the mesh. The new nodes are the quadrature points of the ten-point quadrature rule.

The main elements in this chapter are the definition of second order random processes and their description by means of the Karhunen-Loève expansion. Karhunen-Loève expansion involves the solutions of the Fredholm equation. As shown in two examples, this equation can sometimes be solved analytically. The field obtained after solving the Fredholm equation has a global trend upon which smaller, rapid changes occur. In order to obtain similar fields when no analytical solutions of the Fredholm equation exists, the field can be described by a discrete expansion. Such descriptions involves the values of the covariance function between discrete points. The covariance function often depends on the distance between them. Composite surfaces are manifolds. The distances between points on non planar surfaces can not be computed using euclidean norm. The euclidean distance will be replaced by the shortest path on 3D surfaces. This has not previously been done in the literature.

Chapter 5

Distance computations

The first section, mainly based on [50], links the shortest path to the isotropic and anisotropicle Eikonal equation.
The second section describes the Fast Marching Method (FMM). The FMM approximates the isotropic geodesic distance between two points by solving the isotropic Eikonal equation. The Anisotropic Fast Marching Method (AFMM), described in section 3, solves the anisotropic Eikonal equation and estimates anisotropic geodesic distances. The algorithms used to solve the isotropic and anisotropic Eikonal equations are respectively based on [6, 45, 50] and on [29].

5.1 Eikonal equation

Let's consider an object of surface Ω and a point A on its surface. The goal is to evaluate the geodesic distance between A and any point on Ω. A way to compute all distances with respect to A is to start from A and evaluate the distance of all points which are closest. In other word, this method consists in finding the *level set* or *front*, the set of all points $\boldsymbol{x} \in \mathcal{L}_C$ such that the geodesic distance takes constant value $T(\boldsymbol{x}) = C$.
The level set curve separates the region into points of distances smaller than C (and whose distance is known) and points of unknown distances larger than C. By moving the front outwards, i.e. finding level sets with constant values $C_n > C_{n-1} > ... > C_1 > C$, the method allow to progressively compute geodesic distances from A to any point in space. For example, see the left figure in figure 5.1.
The position of level set $\mathcal{L}_C$ as a function of its distance value C can be assimilated to the wave propagation as a function of time. This analogy allows to transform the front motion problem into a boundary value problem (see figure 5.1).

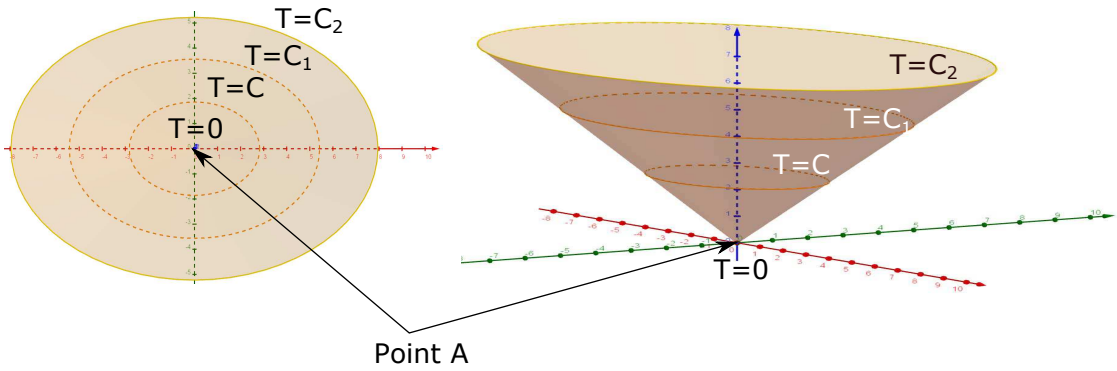

Figure 5.1: Transformation of the front position problem into a boundary value problem.

The boundary value problem takes into account that some region of the object are harder to cross than others. The minimal distance between A and $\boldsymbol{x} \in \Omega$, $T(\boldsymbol{x})$, satisfies the anisotropic Eikonal equation[23, 48]

$$\begin{cases} \sqrt{\nabla T^T(\boldsymbol{x}) \boldsymbol{D} \nabla T(\boldsymbol{x})} = 1, & \boldsymbol{x} \in \Omega \setminus \{A\} \\ T(A) = T_A = 0, & A \in \Omega \end{cases} \tag{5.1}$$

with $\boldsymbol{D}$ a symmetric, positive-definite matrix. Equation (5.1) is a non-linear partial differential equation modelling interface propagation. The goal is to solve the anisotropic Eikonal equation to find $T(\boldsymbol{x})$ for all $\boldsymbol{x} \in \Omega$. These values, in turn, give the distance between A and any point on the surface Ω.
In the isotropic case, the speed function is the same in all directions, $\boldsymbol{D}$ is the identity matrix and the minimal distance are obtained by travelling orthogonally to level sets. Equation (5.1) reduces to the Eikonal equation

$$\begin{cases} |\nabla T(\boldsymbol{x})| = 1, & \boldsymbol{x} \in \Omega \setminus \{A\} \\ T(A) = T_A = 0, & A \in \Omega \end{cases} \tag{5.2}$$

5.2 Fast marching method (FMM)

Starting from point A, whose distance is zero, the Fast Marching Method (FMM) finds an approximate solution to equation (5.2). The FMM finds the solution of the Eikonal equation by propagating the information from smaller values of T to larger ones and moving

the front outwards. The solution is build by starting at A and finding increasing values of T. The "building zone" is a narrow band surrounding the front. This band is moved outwards by freezing the distance values of nodes belonging to the band and adding new nodes inside the building zone. This way, the FMM computes T values at every node of the triangular mesh. As the level set moves outwards, the algorithm computes the minimal distance associated with every node.

For instance, consider the problem of finding all distances with respect to A, coloured in pink, on a planar grid. The situation is illustrated on figure 5.2. The distance value corresponding to A is zero. The algorithms computes possible values for the distance between A and its neighbours. The nodes whose distances have been updated are coloured in blue. By definition, distances can only grow when going away from the source. Therefore, the smallest value among the blue dots must be correct. Its value can be frozen. The update scheme is thus always applied outwards and grey nodes with unknown distance values are progressively updated. The algorithm never recomputes distances corresponding to nodes coloured in pink.

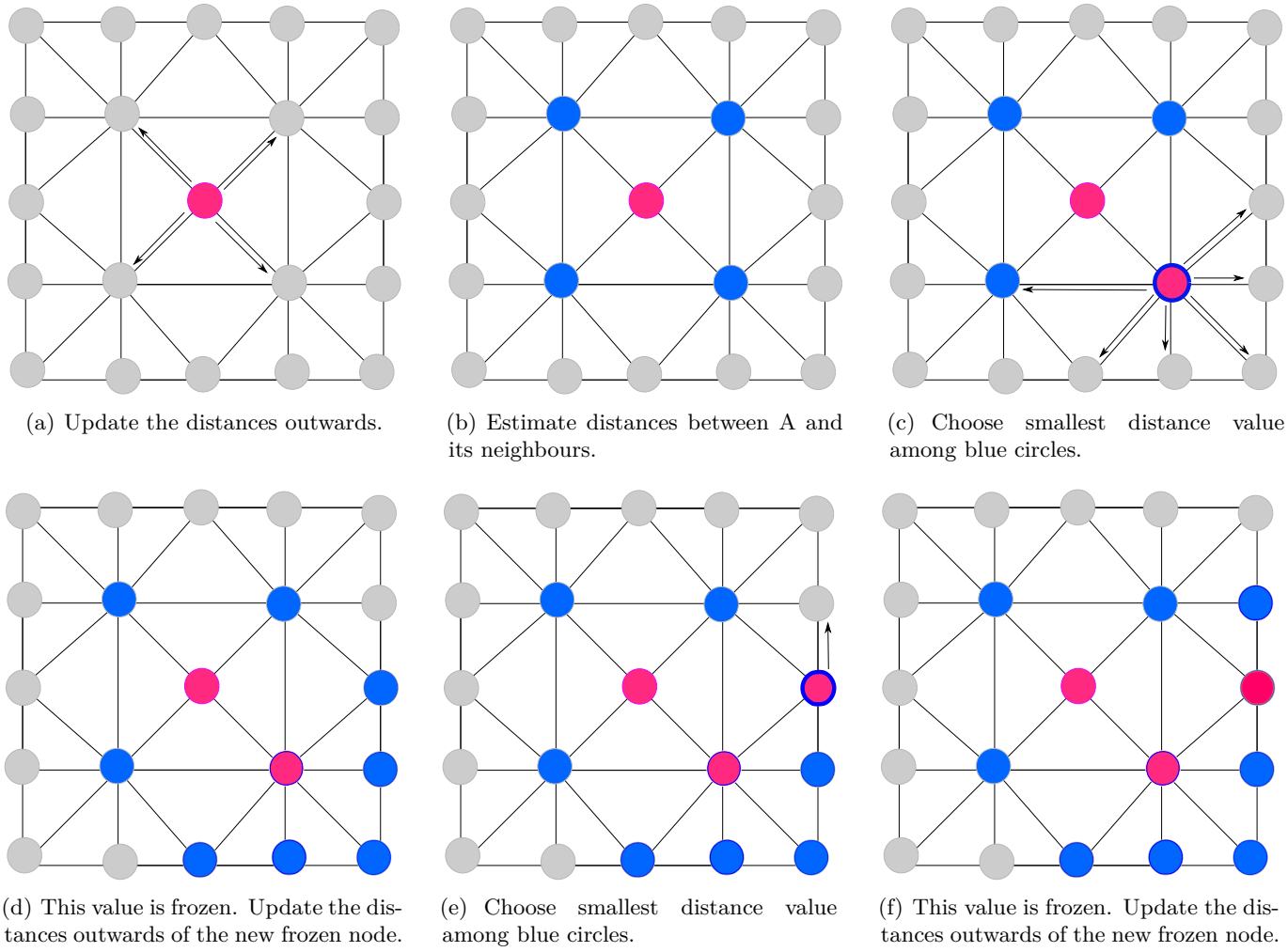

(a) Update the distances outwards.

(b) Estimate distances between A and its neighbours.

(c) Choose smallest distance value among blue circles.

(d) This value is frozen. Update the distances outwards of the new frozen node.

(e) Choose smallest distance value among blue circles.

(f) This value is frozen. Update the distances outwards of the new frozen node.

Figure 5.2: Example of FMM procedure.

the previous example showed that FMM uses three sets of nodes. Nodes can be tagged as Frozen, Close and Far. *Frozen nodes*, in pink, are the set of nodes whose distances have already been computed and will not change during subsequent steps. Every *Close node*, in blue, is one grid point away from a frozen node. This set contains nodes whose distance have been computed but might change in subsequent steps. *Far nodes*, in grey, are the set of nodes whose distances have never been computed.

When the FMM starts, it tags the origin, the starting node, in the Frozen set and fix its T-value to zero. All nodes one grid point away from the origin are labelled as Close. The remaining nodes are tagged as Far. Close and Far nodes are given infinite distance values. The algorithm then updates the distance between every node in the Close set and the origin. The update scheme proceeds as follows:

- Let $minNode$ the node in the set Close with the smallest T-value,
- Add $minNode$ to the set Frozen, remove it from the set Close,
- Tag all neighbours M of $minNode$ that are not in the set Frozen as Close,
- Update the T-values of all neighbours using a local update scheme,
- If some distances remain unknown, start the loop again.

Algorithm 2 summarizes the whole Fast Marching Procedure.

The FVF algorithm uses a local update scheme to compute new distance values. Let's take the same example as previously to show how the local update procedure works. The different steps of the exemple are shown on figure 5.3. As the algorithm starts, A

Algorithm 1 Fast Marching Method

procedure FMM($Nodes$)
  Initialize:
  $Frozen$:= starting node with value $T = 0$
  $Close$:= all points one grid point ($T = \infty$) away from the initial condition in Frozen
  Far := all other grid points ($T = \infty$)
  while $Frozen! = Nodes$ **do**
    for all $node \in Close$ **do**
      $T[node] \leftarrow$ LocalUpdate
    $minNode \leftarrow \min_{node \in Close} T[node]$
    $Frozen \leftarrow Frozen \cup \{minNode\}$ with $T[minNode]$ known
    $Close \leftarrow Close \setminus \{minNode\}$
    M := set of neighbours to minNode belonging to the far set
    $Close \leftarrow Close \cup M$
    $Far \leftarrow Far \setminus M$

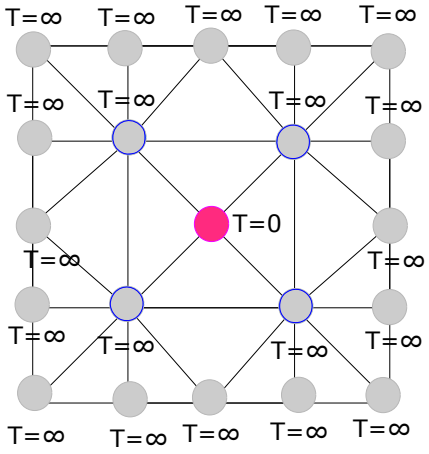

(a) Initialisation of the algorithm.

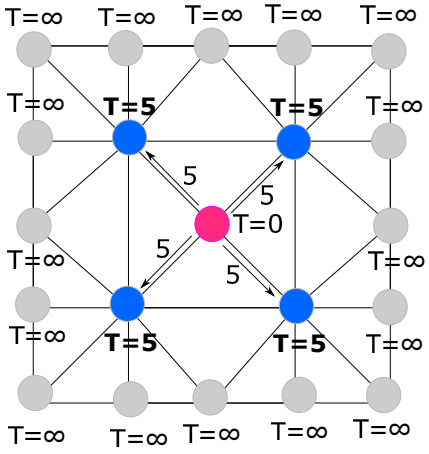

(b) Estimate distances between A and its neighbours.

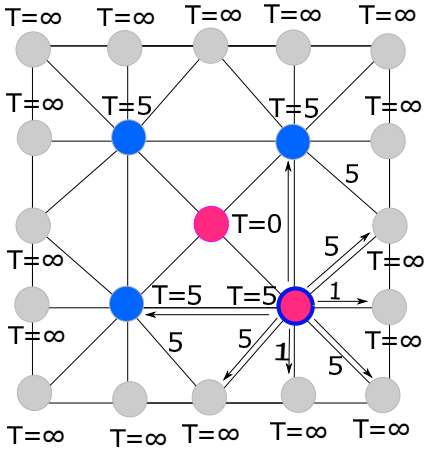

(c) Choose smallest distance value among blue circles.

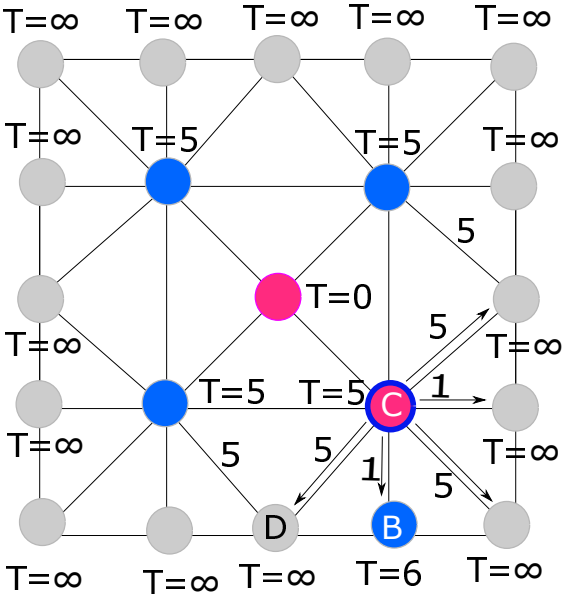

(d) This value is frozen. Update a new distance using the T-value of the newly frozen node and the length of the edge.

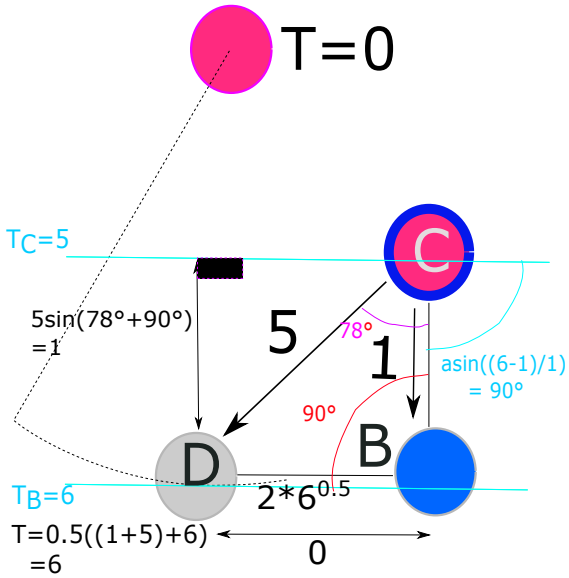

(e) Update a new distance using T-values of two nodes and the lengths of the edges.

Figure 5.3: Examples of local isotropic distance updates.

has zero T-value and all other nodes have infinite T-values. Because only T_A is known, the distance between a neighbour of A and A is the length of the edge between them.

Then, for instance, node B is updated. Because only node C is known, the T-value at node B is given by the sum of T_C and the length of the edge between B and C.
Let's illustrate a local update scheme when two nodes are known. In order to clarify the procedure, only the node involved are kept on the figure. The first step is to try to evaluate the direction of the tangent at the level set going through the node D with unknown T-value. Two parallels to the tangent are traced at nodes B and C. The angle between the parallel at node C of smallest T-value $T_C = 5$ and segment CB is estimated by $\arcsin\left(\frac{T_B - T_C}{|CB|}\right) = 90°$. Finally, the distance H between nodes C and D and the distance h between B and D are evaluated perpendicularly to the parallels at node C and B:

$$H = 5\sin(78° + 90°) = 1$$
$$h = 2\sqrt{6}\sin(90° - 90°) = 0$$

The T-value associated with node D is obtained by averaging the distances when going from node C to node D and from node B to node D:

$$T = \frac{(H + T_c) + (h + T_B)}{2} = \frac{(1 + 5) + 6}{2} = 6$$

More formally, the distance is computed using a local update scheme summarized in algorithm 2. To explain the local update scheme, let's first consider an acute triangle ABC with A and B belonging to the Frozen set and α, β and γ the angles at nodes A, B and C. Let's also assume that the distance T_B is larger than the distance T_A. The triangle is shown on figure 5.4.

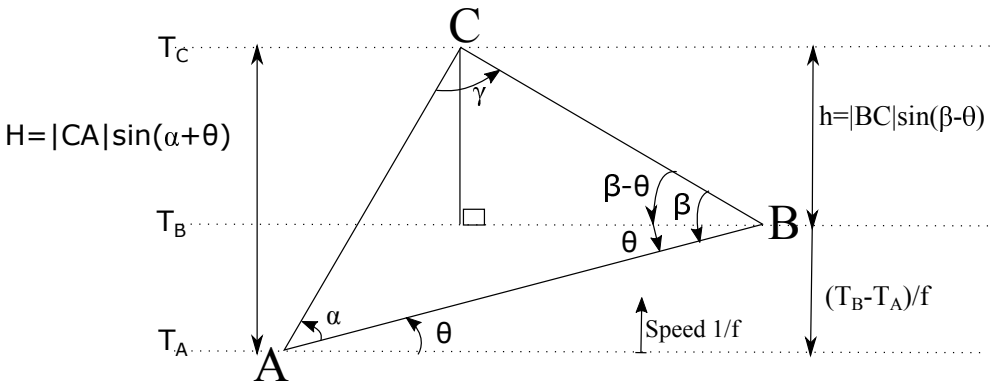

Figure 5.4: Updating T_C from T_A and T_B. Modified from [6].

By definition, the front moves outwards. Indeed, the further away a point is from the origin, the largest the distance between the point and the origin. Therefore, the level set must first pass on A, then on B and finally on C. To ensure the last, the following conditions must be satisfied:

- the level set can propagates from A to B with difficulty $f = 1 : T_B - T_A \leq |AB|$;
- the level goes through B before $C : \theta \leq \beta$;
- the vertical line from C to the level set of value T_B belongs to the triangle. This allows to compute T_C based on T_A and T_B : $\theta + \alpha \leq \frac{\pi}{2}$.

If those 3 conditions are not satisfied, update T_C based only on T_A or only on T_B. Algorithm 2 summarises the update scheme for the general case $T_B \geq T_A$ or $T_A \geq T_B$.

Algorithm 2 Local Update of the distance T

```
1:  procedure LocalUpdate(A,B,C)
2:      if T_A − T_B ≤ f|AB| then
3:          θ = arcsin((T_B − T_A)/|AB|)
4:          if max(0, β − π/2) ≤ θ ≤ π/2 − α or β − π/2 ≤ θ ≤ min(0, π/2 − α) then
5:              h = |BC| sin(β − θ)
6:              H = |AC| sin(α + θ)
7:              T_C = min{T_C, ((T_A+H)+(T_B+h))/2}
8:          else
9:              T_C = min{T_C, T_A + |AC|, T_B + |BC|}
10:     else
11:         T_C = min{T_C, T_A + |AC|, T_B + |BC|}
```

In case of obtuse triangles, split the obtuse angle γ by adding a new point M at the middle of the opposite segment. Estimate $T_M \approx \frac{T_A + T_B}{2}$ and compute T_C in triangle AMC.

In the anisotropic case, the speed evolves depending on the direction of travel. The algorithm solving the isotropic Eikonal equation takes into account that the gradient direction coincides with the characteristic direction. This is not always true in the anisotropic case. Using algorithms 1 and 2 may therefore lead to inaccurate distance's values [8].

5.3 Anisotropic fast marching method (AFMM)

In order to solve anisotropic eikonal equation (5.1), Konukoglu et. al. [29] adapted FMM. They developed a recursive fast marching approach. Their algorithm includes a correction scheme to deal with the difference of direction between the gradient and the characteristic direction. Apart from the correction scheme and the local update procedure, the AFMM is very similar to the FMM.

For instance, consider the problem of finding all anisotropic distances with respect to A on a planar grid. As previously, node A is coloured in pink and the algorithm computes possible values for the anisotropic distances between A and its neighbours. The nodes whose distances have been updated are coloured in blue.
The smallest value among the blue dots, node B, is coloured in pink. However, contrarily to the isotropic case, this value might be inexact. The update scheme is again applied outwards and a new smallest value, corresponding to node C, is selected among the blue nodes. From this moment, represented on figure 5.5(a), the AFMM might differ from the FMM algorithm.
When T_B was computed, the distance of C was still unknown and the characteristic direction was perhaps not contained by node A. In order to obtain the smallest anisotropic distance, the characteristic must be contained by the Known neighbourhood of node B. Therefore, the distance of node B needs to be recomputed. If the distance remains the same, the algorithms proceeds as in the FMM. Otherwise, T_B is updated and surrounded in green.
The algorithm computes the anisotropic distances of other neighbours of C. The neighbours of C that were previously coloured in grey are coloured in blue.
If some nodes are surrounded in green, the algorithm selects the node surrounded in green with the smallest anisotropic distance and "un-surrounds" it. It then restarts the loop and updates distances of Known, Close and Far nodes.

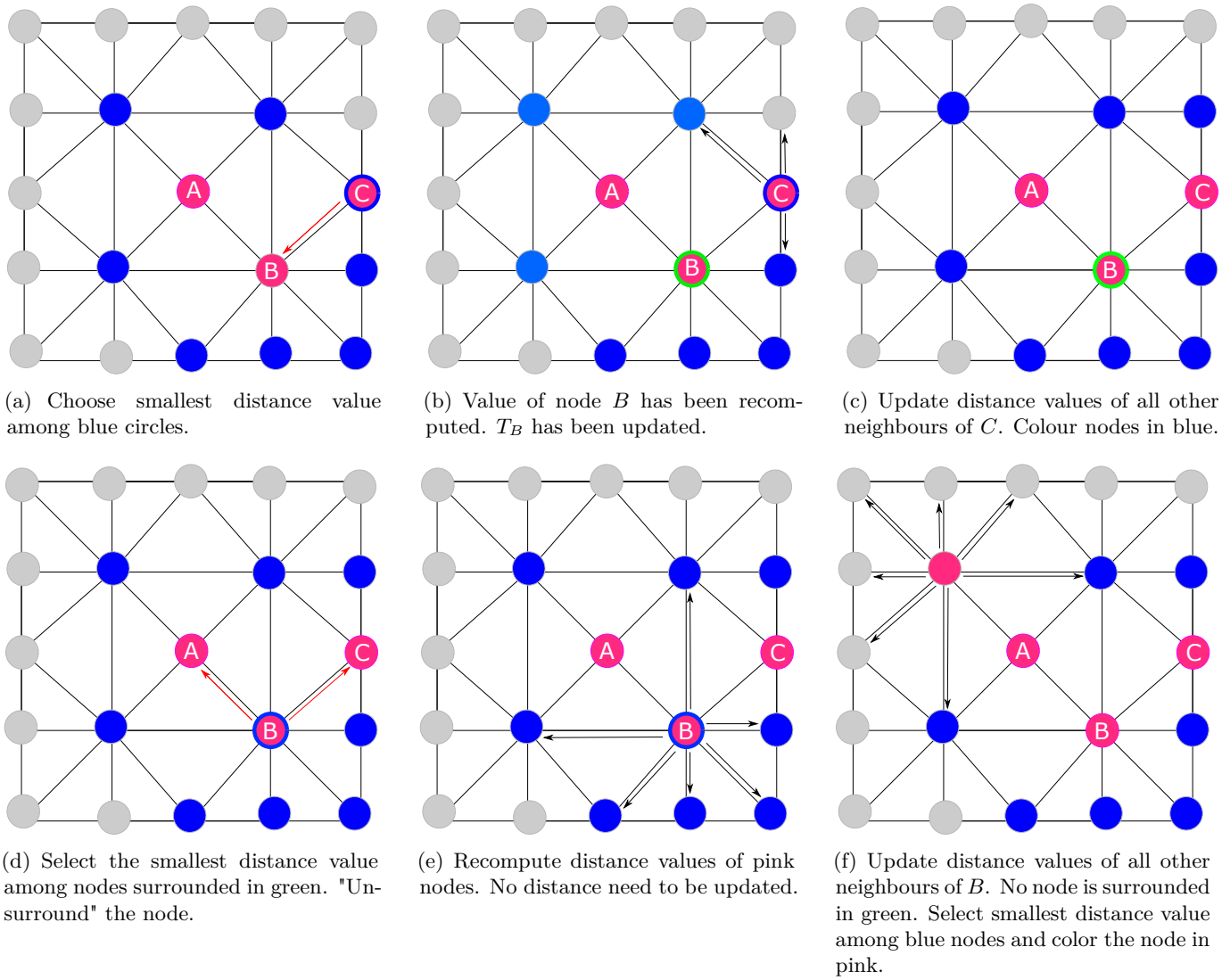

(a) Choose smallest distance value among blue circles.

(b) Value of node B has been recomputed. T_B has been updated.

(c) Update distance values of all other neighbours of C. Colour nodes in blue.

(d) Select the smallest distance value among nodes surrounded in green. "Unsurround" the node.

(e) Recompute distance values of pink nodes. No distance need to be updated.

(f) Update distance values of all other neighbours of B. No node is surrounded in green. Select smallest distance value among blue nodes and color the node in pink.

Figure 5.5: Example of AFMM procedure.

Like in the FMM, at initialisation, node A is set as Frozen and its distance set to 0. All nodes one grid point away from the origin are labelled as Close. The remaining ones are Far. Close and Far nodes are given infinite T-values.
As shown in the example, the recursive correction appears in the beginning of the main loop. Before computing T-values of nodes belonging to the Close set, the distances between Frozen nodes and the origin are recomputed. If the obtained anisotropic distance is smaller than the old one, the node is added to the Changed set. The *Changed list* contains known nodes whose T-values have been changed. Every time the main loop restarts, the algorithm checks whether the Changed list is empty. If the Changed list is empty, it selects the smallest T-value node, $minNode$, in the Close set, remove the node from the Close set and add it to the Frozen set. If the Changed list is not empty, it selects and removes the smallest T-value node, $minNode$, from the Changed set. The whole procedure

is summarized in algorithm 3.

Algorithm 3 Anisotropic Fast Marching Method

procedure AFMM(Nodes)
  Initialize:
  $Frozen$:= starting node with value $T = 0$
  $Close$:= all points one grid point ($T = \infty$) away from the initial condition in Frozen
  Far := all other grid points ($T = \infty$)
  $Changed := \phi$
  for all $node \in Close$ **do**
    $T[node] \leftarrow$ LocalUpdate
  while $Frozen! = Nodes$ **do**
    if $Changed$!= ϕ **then**
      $minNode \leftarrow \min_{node \in Changed} T[node]$
      $Changed \leftarrow Changed \setminus \{minNode\}$
    else
      $minNode \leftarrow \min_{node \in Close} T[node]$
      $Frozen \leftarrow Frozen \cup \{minNode\}$ with $T[minNode]$ known
      $Close \leftarrow Close \setminus \{minNode\}$
    $\mathcal{N}(minNode)$:= all nodes one grid point away from $minNode$
    for all $node \in Frozen \cap \mathcal{N}(minNode)$ **do**
      $oldT := T[node]$
      $T[node] \leftarrow$ LocalUpdate
      if $T[node] < oldT$ **then**
        $Changed \leftarrow Changed \cup \{node\}$
    for all $node \in \mathcal{N}(minNode) \setminus Frozen$ **do**
      if $node \in Far$ **then**
        $Far \leftarrow Far \setminus \{node\}$
        $Close \leftarrow Close \cup \{node\}$
      $T[node] \leftarrow$ LocalUpdate

In order to find the distance between node X and the origin, algorithm 3 uses a local update scheme on a triangle XYZ. Because the distances are anisotropic with respect to the fibre direction, local coordinate systems are defined in every triangle. The first axis corresponds to the fibre direction. Its origin is the first node of the triangle. The second axis is perpendicular to the fibre direction. The axis system is shown on figure 5.6 for a triangle $X_1X_2X_3$ with X_1 the first node of the triangle.
Now that the axis system has been defined, it becomes possible to compute anisotropic distances. Let's now first consider a triangle XYZ where T_Y and T_Z are known. In order to compute the anisotropic distance between X and the origin, the AFMM assumes that, if the direction of travel at a mesh point X is $\boldsymbol{a}$, the direction of motion does not change until the level set has reached the opposite edge YZ at point $\tilde{x}$ (see figure 5.7). Because the direction $\boldsymbol{a}$ is unknown, the algorithm tries to find point $\tilde{x} = p(Y - Z) + Z$ on segment YZ that minimises the anisotropic distance T_X. The method is based on distance interpolation between nodes:

$$f_{2D}(X, Y, Z) = \min_{p \in [0,1]} pT_Y + (1 - p)T_Z + ||\tilde{x}X||_M$$

where $||x||_M = \sqrt{xMx}$ is the anisotropic norm of x [49]. The analytical solution of this constraint optimisation problem is given in Appendix D.
When only T_Y is known, the algorithm gives the following anisotropic distance:

$$f_{1D}(X, Y) = T_Y + ||YX||_M$$

The method is similar for T_Z known and T_Y unknown. The local update procedure is summarized in algorithm 4.

The AFMM approximates distances. In order to analyse the error between the exact and the AFMM based distances, the AFMM is applied on a circle with diameter 2 mm. The fibres are considered parallel to direction $\boldsymbol{e}_x$ and the exact anisotropic distance between two points $\boldsymbol{x}$ and $\boldsymbol{y}$ is given by

$$d(\boldsymbol{x}, \boldsymbol{y}) = \sqrt{(x_1 - y_1)^2 + 2(x_2 - y_2)^2}$$

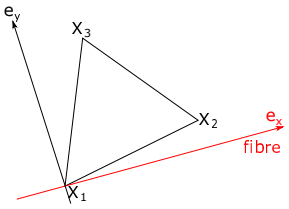

Figure 5.6: Axis system used for the local update of anisotropic distances.

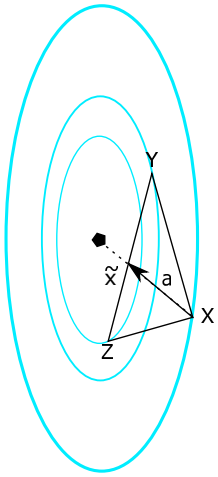

Figure 5.7: Updating T_X from T_Y and T_Z.

Algorithm 4 Local Update of Anisotropic distances T

```
procedure LocalUpdate(X,Y,Z)
    if T_Y known then
        if T_Z known then
            T_X = min{T_X, f_2D(X, Y, Z)}
        else
            T_X = min{T_X, f_1D(X, Y)}
    else if T_Z known then
        T_X = min{T_X, f_1D(X, Z)}
```

Three different meshes with increasing fineness are considered (figures 5.8(b), 5.9(b) and 5.10(b)). Those are obtained by refining the original meshes (figures 5.8(a), 5.9(a) and 5.10(a)). The characteristics of all meshes are written in table 5.1.
Anisotropic level sets with respect to the origin $\boldsymbol{x}_0 = (0; 0)$ and relatives errors between the AFMM based distances $d_{AFMM}(\boldsymbol{x}, \boldsymbol{y})$ and the exact anisotropic distances $d_{exact}(\boldsymbol{x}, \boldsymbol{y})$

$$\epsilon_{ani}(\boldsymbol{x}, \boldsymbol{y}) = \frac{|d_{AFMM}(\boldsymbol{x}, \boldsymbol{y}) - d_{exact}(\boldsymbol{x}, \boldsymbol{y})|}{d_{exact}}$$

are shown on figures 5.8(c,d), 5.9(c,d), 5.10(c,d). The algorithm gives relatively accurate results. The level sets are ellipses centred at the origin with axis corresponding to the axis of the plane. The ratios between their semi-major and semi-minor axis are approximately $\sqrt{2}$. The largest error occur near the source points. The errors decrease as the fineness of the mesh increases.

	Original mesh		**Refined mesh**	
	Number of nodes	Number of elements	Number of nodes	Number of elements
Circle $l_c = 0.1$	1710	1779	15026	29664
Circle $l_c = 0.2$	434	467	3696	7200
Circle $l_c = 0.3$	198	221	1633	3132
Chair	3100	5964	27174	53676

Table 5.1: Characterisation of the different meshes.

Now that the efficiency of the AFMM has been shown on a 2D case, the AFMM will be applied on a chair. The mesh of the chair, given on figure 5.11(a) was refined as shown on figure 5.11(b). The dimensions of the chair, indicated in mm, are shown on both figures. Informations about the characteristics of the original and the refined meshes can be found in table 5.1. In figure 5.12, the fibres are considered parallel to direction $\boldsymbol{e}_x$ and the exact anisotropic distance between two points $\boldsymbol{x}$ and $\boldsymbol{y}$ is given by

$$d(\boldsymbol{x}, \boldsymbol{y}) = \sqrt{5(x_1 - y_1)^2 + (x_2 - y_2)^2}$$

On figure 5.13, the fibres are still parallel to direction $\boldsymbol{e}_x$ but the anisotropic distance becomes

$$d(\boldsymbol{x}, \boldsymbol{y}) = \sqrt{(x_1 - y_1)^2 + 2(x_2 - y_2)^2}$$

The results obtained on the circle highlight the relation between mesh fineness and small distance computation errors. Those on the chair show the efficiency of the distance computation method on 3D surface for different anisotropic norms.

Once distances have been computed, the Gaussian random field can be produced. The discrete field's values will be different from the values of the original field at the discrete points. This difference is generated by various errors, among which the distance computation errors.

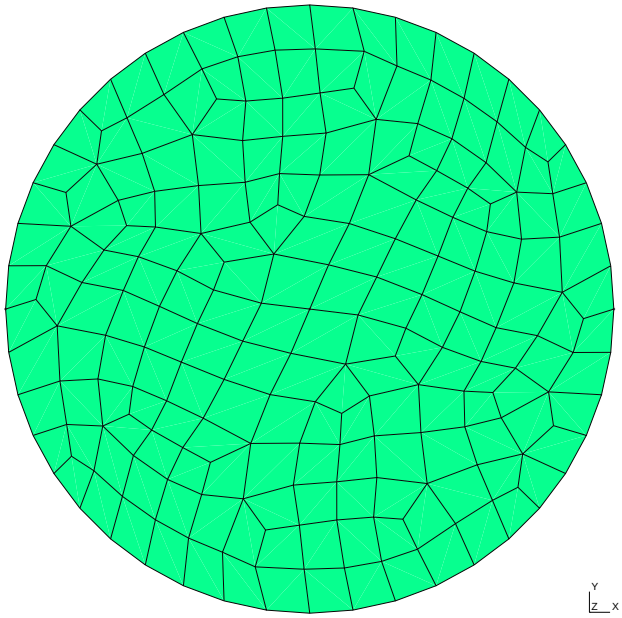

(a) Initial mesh.

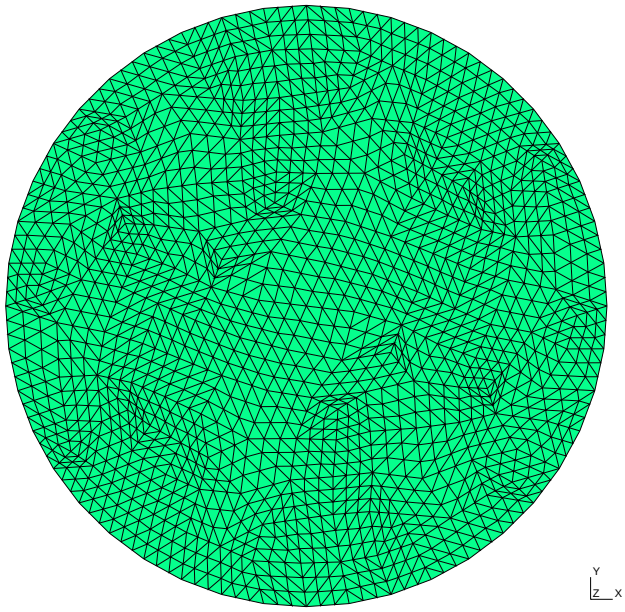

(b) Refined mesh.

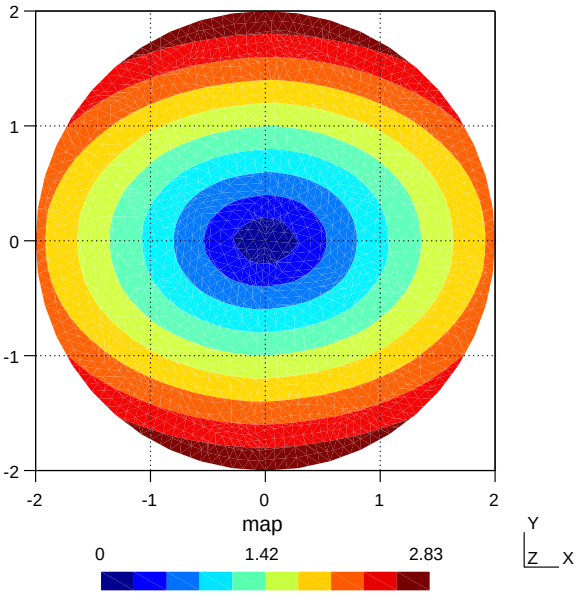

(c) Anisotropic distance computed with AFMM.

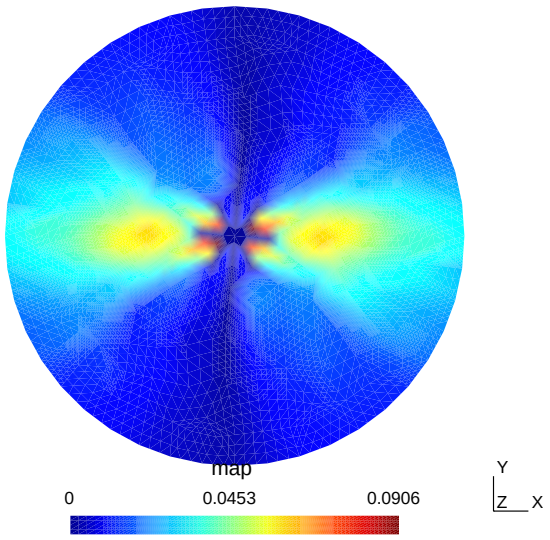

(d) Relative error between the distances computed by AFMM and the exact anisotropic distances.

Figure 5.8: Circle with mesh fineness $l_c = 0.3$. Anisotropic distance norm $d(\boldsymbol{x}, \boldsymbol{y}) = \sqrt{(x_1 - y_1)^2 + 2(x_2 - y_2)^2}$. Fibres parallel to $\boldsymbol{e}_x$ axis.

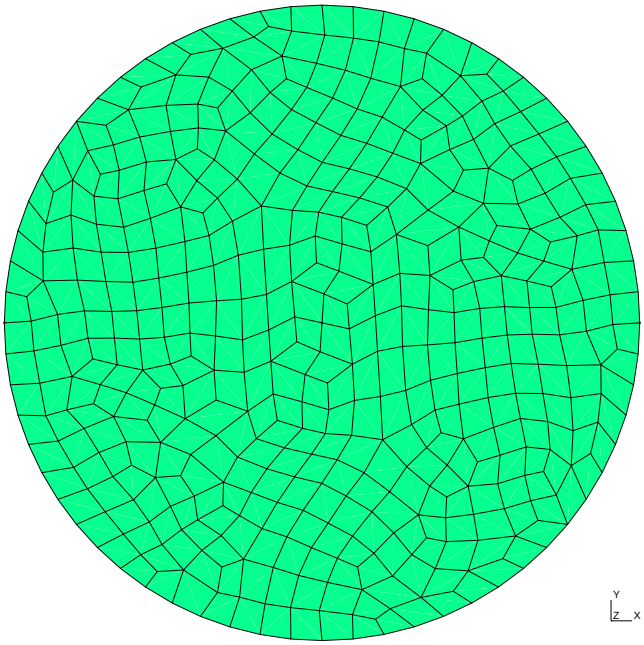

(a) Initial mesh.

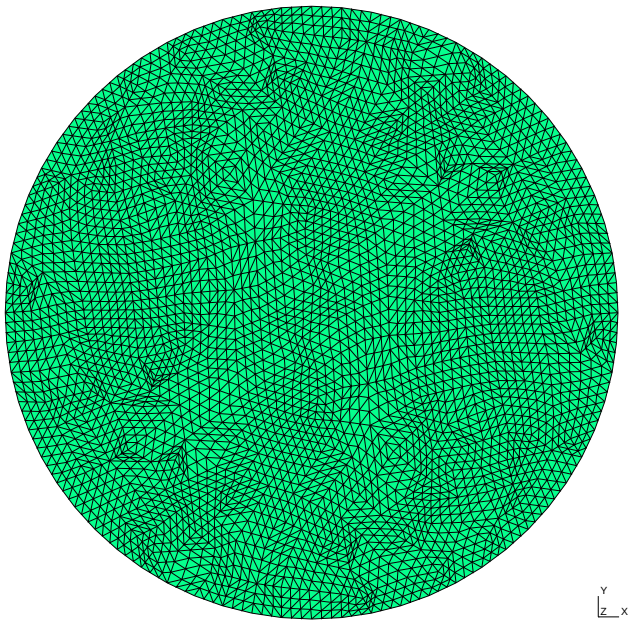

(b) Refined mesh.

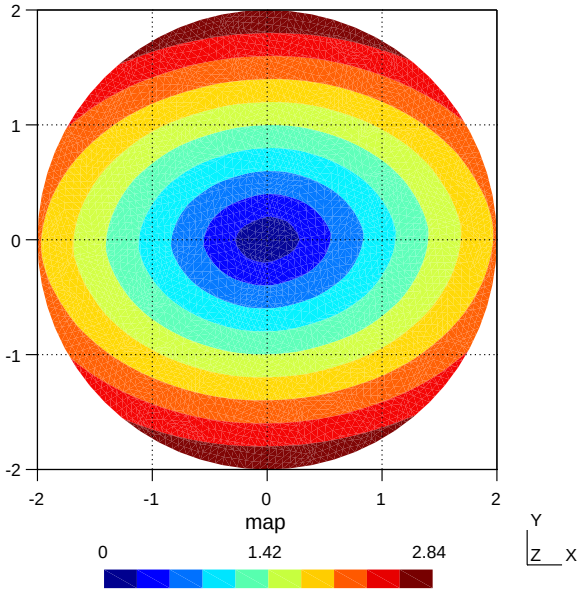

(c) Anisotropic distance computed with AFMM.

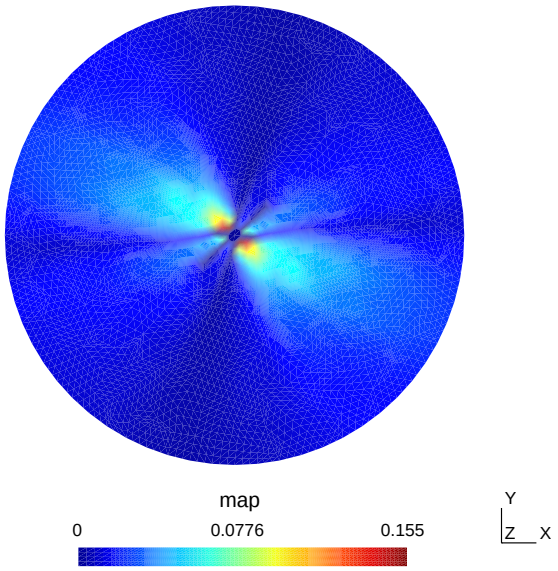

(d) Relative error between the distances computed by AFMM and the exact anisotropic distances.

Figure 5.9: Circle with mesh fineness $l_c = 0.2$. Anisotropic distance norm $d(\boldsymbol{x}, \boldsymbol{y}) = \sqrt{(x_1 - y_1)^2 + 2(x_2 - y_2)^2}$. Fibres parallel to $\boldsymbol{e}_x$ axis.

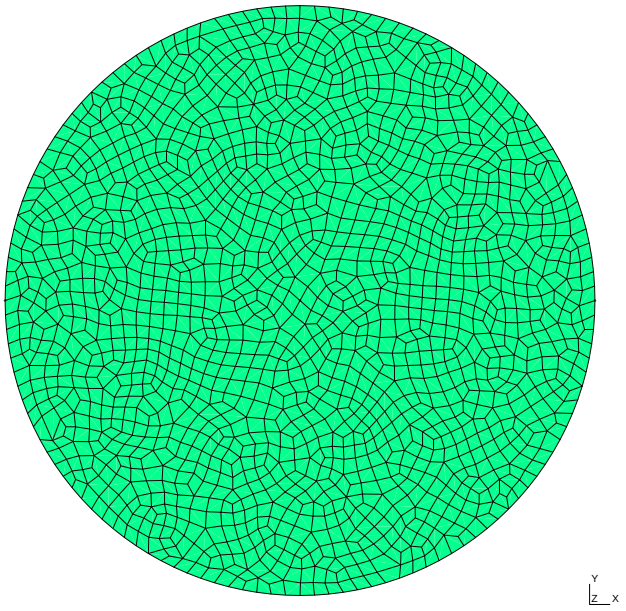

(a) Initial mesh.

(b) Refined mesh.

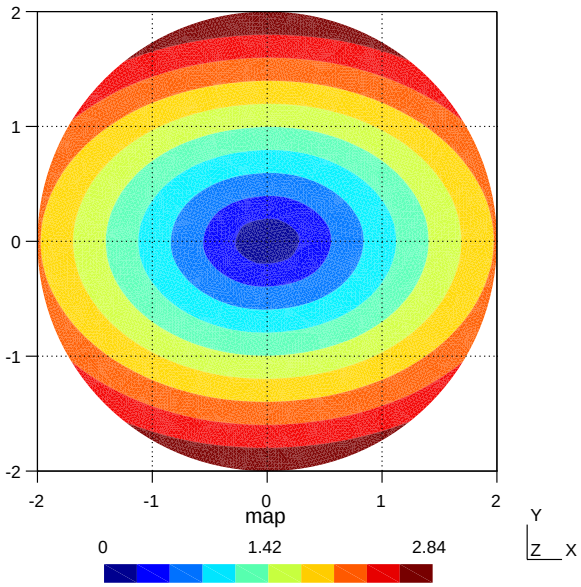

(c) Anisotropic distance computed with AFMM.

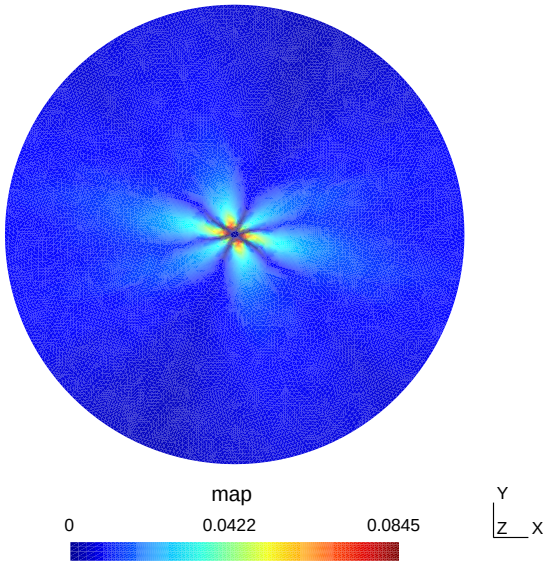

(d) Relative error between the distances computed by AFMM and the exact anisotropic distances.

Figure 5.10: Circle with mesh fineness $l_c = 0.1$. Anisotropic distance norm $d(\boldsymbol{x}, \boldsymbol{y}) = \sqrt{(x_1 - y_1)^2 + 2(x_2 - y_2)^2}$. Fibres parallel to $\boldsymbol{e}_x$ axis.

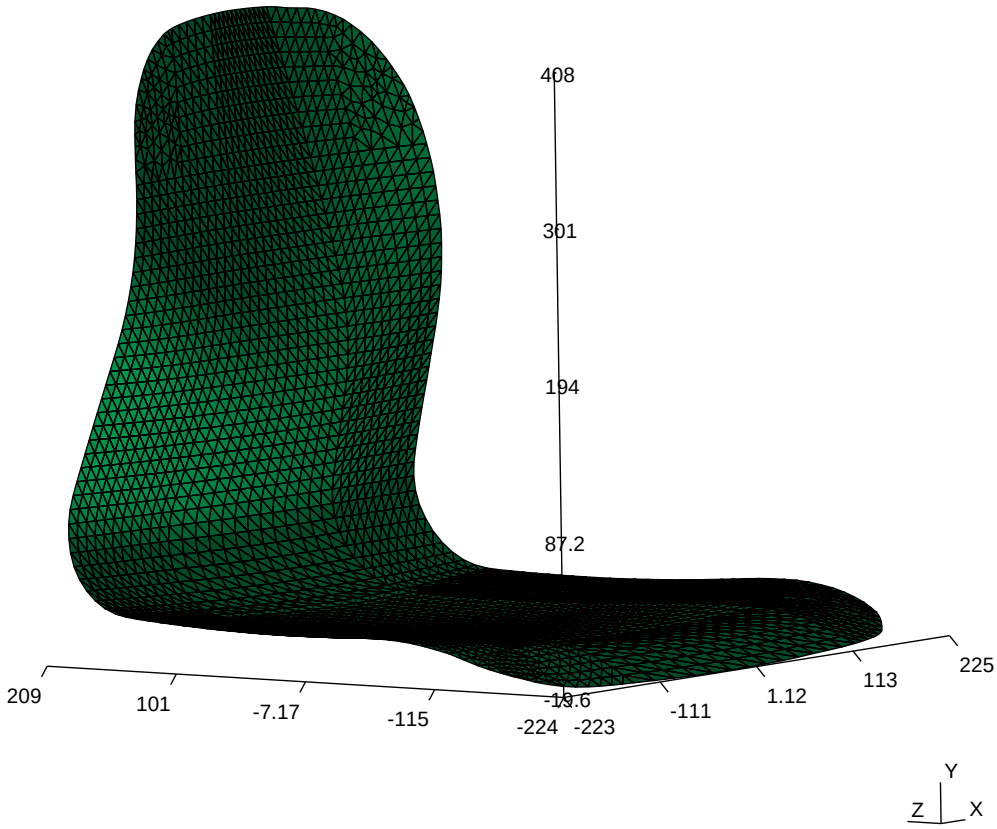

(a) Initial mesh.

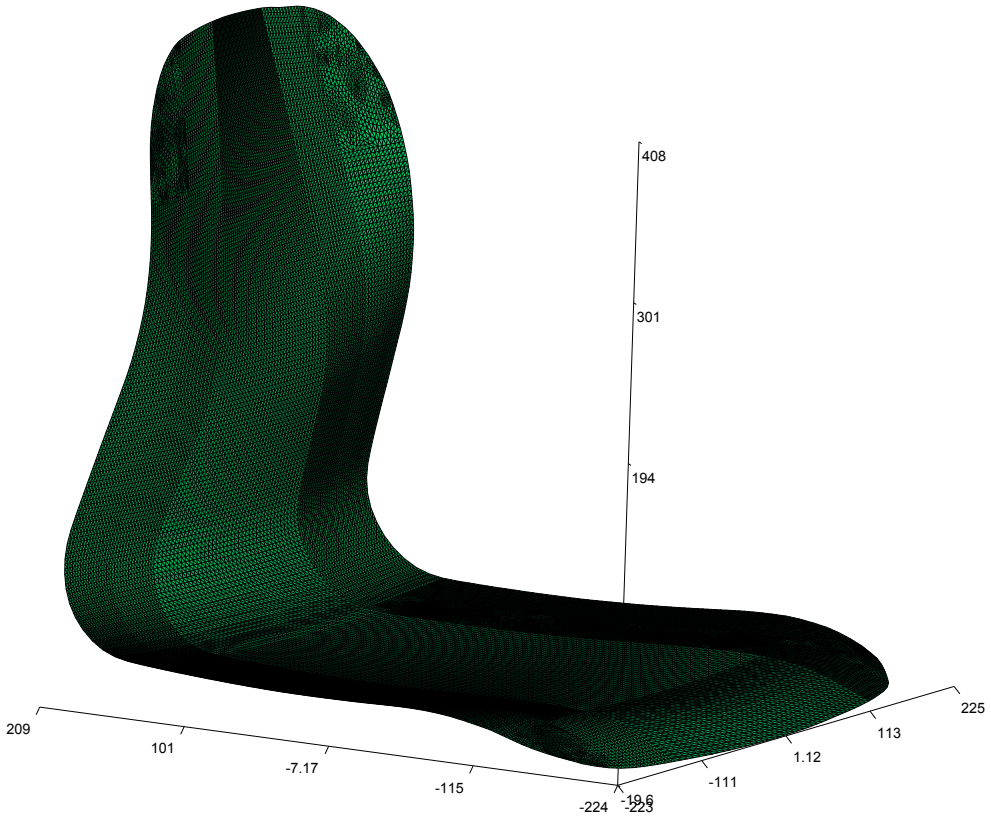

(b) Refined mesh.

Figure 5.11: Initial and refined finite element mesh on a chair.

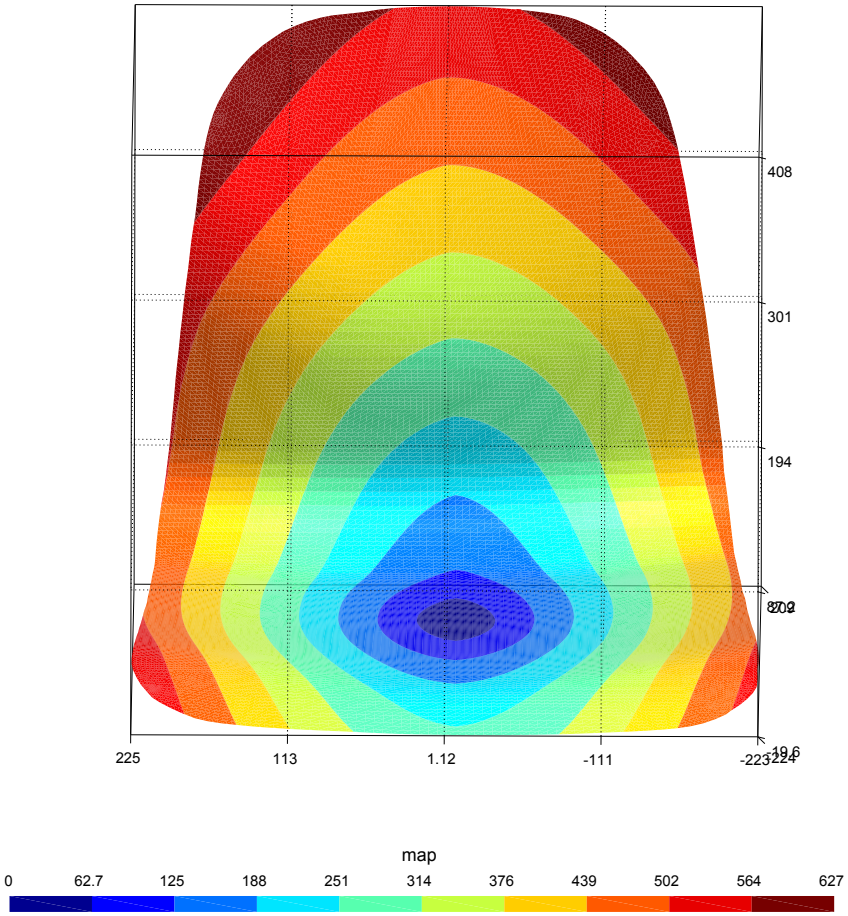

(a) Front view.

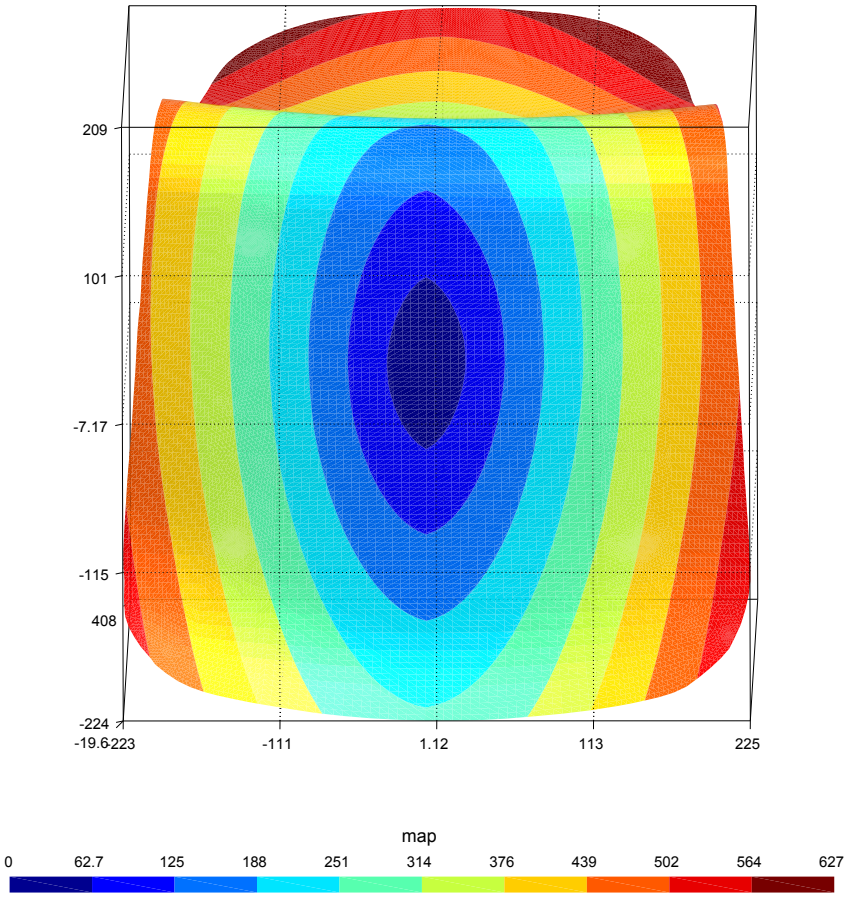

(b) View from under.

Figure 5.12: Anisotropic distance on a chair $d(\boldsymbol{x}, \boldsymbol{y}) = \sqrt{5(x_1 - y_1)^2 + (x_2 - y_2)^2}$

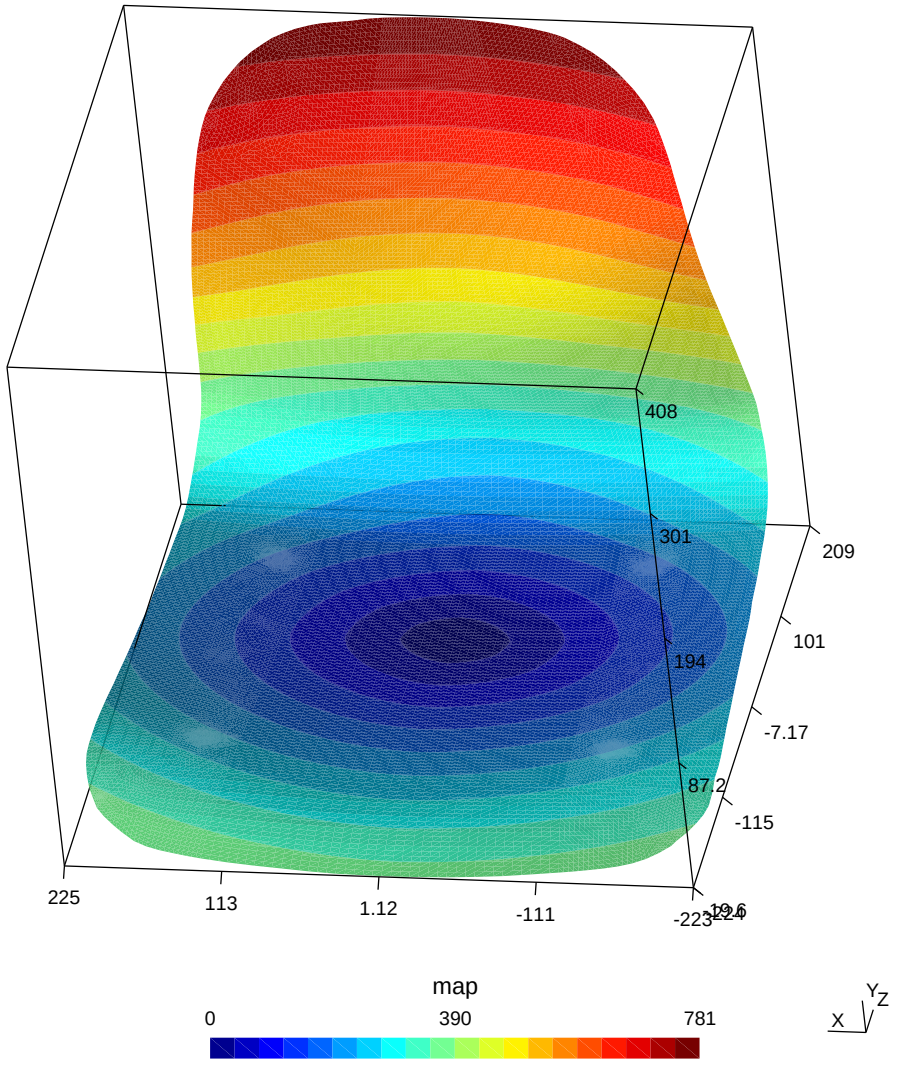

Figure 5.13: Anisotropic distance on a chair $d(\boldsymbol{x}, \boldsymbol{y}) = \sqrt{(x_1 - y_1)^2 + 2(x_2 - y_2)^2}$.

Chapter 6

Error analysis

A series of approximations have been made in order to estimate the FVF field. The original second order random field is continuous. In order to be represented numerically, the eigenfunctions are approximated by a sum of basis functions defined on the mesh. Due to this approximation, the discrete random field is defined by a truncated series. Furthermore, the integrals in the Fredholm equation are computed numerically using a quadrature rule.

Due to these approximations, the discrete values of the field are different from those of the original FVF field at the same points. Let $\epsilon(\boldsymbol{x}, \theta) = u(\boldsymbol{x}, \theta) - \hat{u}(\boldsymbol{x}, \theta)$ the approximation error. The error variance (normalized variance of the approximation error) is given by [4] :

$$\epsilon_\sigma(\boldsymbol{x}) = \frac{Var[u(\boldsymbol{x}, \theta) - \hat{u}(\boldsymbol{x}, \theta)]}{Var[u(\boldsymbol{x}, \theta)]}$$

The mean error variance is defined as the weighed integral of the error variance:

$$\bar{\epsilon}_\sigma = \frac{1}{|\Omega|} \int_\Omega \epsilon_\sigma(\boldsymbol{x}) d\boldsymbol{x}$$

with $|\Omega| = \int_\Omega d\boldsymbol{x}$. The variance of the discretized field is given by $Var[\hat{u}(x, \theta)] = \sum_{i=1}^{M} \hat{\lambda}_i \hat{\phi}_i^2(x)$. The error variance is thus given by [54]:

$$\epsilon_\sigma(x) = 1 - \frac{\sum_{i=1}^{M} \lambda_i \phi_i^2(x)}{\sigma^2(x)}$$

Let a constant variance over the field, the mean error variance becomes

$$\bar{\epsilon}_\sigma = 1 - \frac{1}{|\Omega|} \frac{1}{\sigma^2} \sum_{i=1}^{M} \lambda_i$$

Consider two approximated Gaussian random fields on circles with mesh characteristics given in table 5.1. The first, $\hat{u}_{exact}(\boldsymbol{x}, \theta)$, is computed using an exact distance. Its associated mean error variance is denoted $\bar{\epsilon}_{\sigma,exact}$. The second, $\hat{u}_{FMM}(\boldsymbol{x}, \theta)$ or $\hat{u}_{AFMM}(\boldsymbol{x}, \theta)$, is computed using the FMM or the AFMM based distance. Its associated mean error variance is denoted $\bar{\epsilon}_{\sigma,FMM}$ or $\bar{\epsilon}_{\sigma,AFMM}$. Both fields are generated using the covariance function

$$C(\boldsymbol{x}, \boldsymbol{y}) = \begin{cases} 0 & \text{if } dist(\boldsymbol{x}, \boldsymbol{y}) > l_{c,Cov} \\ \sigma^2 \left(1 - \frac{dist(\boldsymbol{x}, \boldsymbol{y})}{l_{c,Cov}}\right) & \text{else} \end{cases} \tag{6.1}$$

The errors will depend on the distance computation methods, the mesh fineness, the covariance characteristic length and the quadrature rules.

Let's first consider constant basis functions with one-point quadrature rule. Three random fields are shown on figure 6.1 for $l_{c,Cov} = 0.5$.
The errors are shown on figure 6.2 for $l_{c,Cov} = 0.5$ and $l_{c,Cov} = 0.25$. The mean error variance decreases as the number of terms in the series increases. The smallest error occurs when the number of eigenvalues used in the expansion is equal to the number of elements in the mesh. When the number of elements increases, the smallest error decreases. The relative difference between errors obtained using exact distance and FMM type distance converges slowly to zero. The relative errors when using 90% of the eigenvalues are shown on table 6.1.

$l_{c,Cov}$	0.5	0.25
l_c		
0.1	2.17%	6.15%
0.2	5.43 %	9.96%
0.3	7.03 %	9.97%

Table 6.1: Relative errors w.r.t. the mesh fineness and the covariance characteristic length using constant basis functions, 1 point quadrature rule and 90% of the eigenvalues.

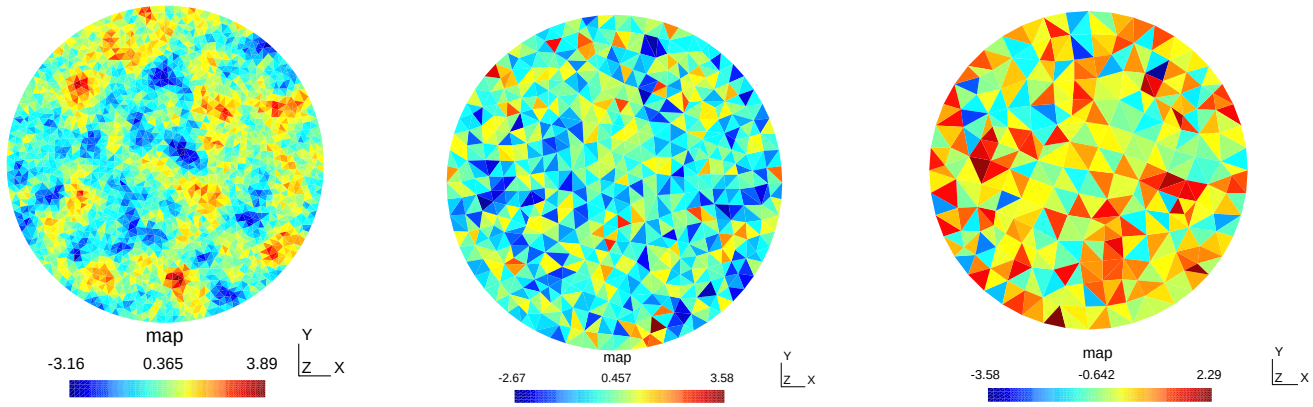

(a) $l_c = 0.1$ (b) $l_c = 0.2$ (c) $l_c = 0.3$

Figure 6.1: FVF using a 1-point quadrature rule, constant basis functions and covariance characteristic length $l_{c,Cov} = 0.5$.

Due to the slow decrease of the relative error, almost all eigenvalues and eigenfunctions should be used to compute the Gaussian random field. The evolution of the graphs only slightly depends on the covariance characteristic length. When the covariance characteristic length is greater, the error drops quicker at the beginning of the graph. Contrarily, the drop in the relative error happens more smoothly at the end of the graph.
The covariance function can be estimated back from the eigenvalues and eigenfunctions computed. The obtained covariance function is compared with the true covariance function with characteristic length $l_{c,Cov} = 0.5$ in figure 6.3 and with characteristic length $l_{c,Cov} = 0.25$ in figure 6.4. The covariance functions obtained fit very well the initial covariance functions, especially for meshes with great fineness.

Let's finally consider linear basis functions with ten-points quadrature rule. Three random fields are shown on figure 6.5 for $l_{c,Cov} = 0.5$.

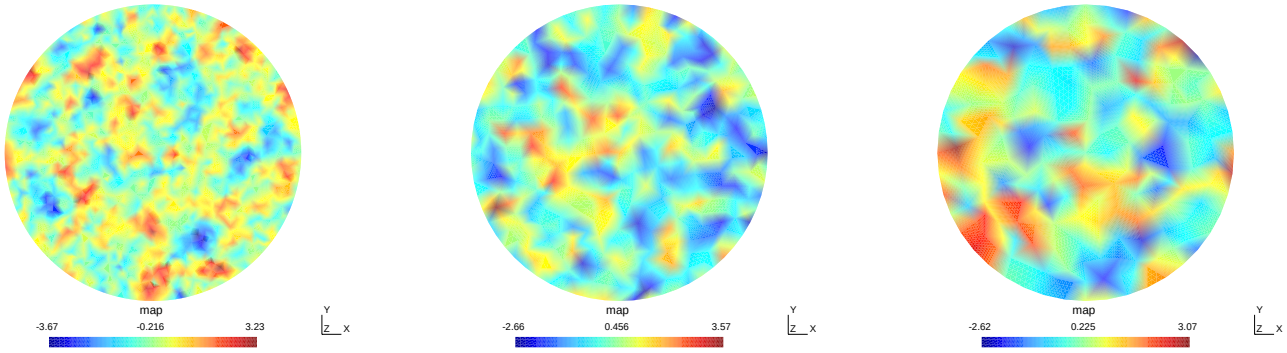

(a) $l_c = 0.1$ (b) $l_c = 0.2$ (c) $l_c = 0.3$

Figure 6.5: FVF using a 10-point quadrature rule, linear basis functions and covariance characteristic length $l_{c,Cov} = 0.5$.

The errors are shown on figure 6.6 for $l_{c,Cov} = 0.5$ and $l_{c,Cov} = 0.25$. The errors are worse than in the previous case but the relative errors behave as in the previous case. The relative errors when using 90% of the eigenvalues are shown on table 6.2.

$l_{c,Cov}$	0.5	0.25
l_c		
0.1	2.94%	3.74%
0.2	3.69 %	4.08%
0.3	4.33 %	2.21%

Table 6.2: Relative errors w.r.t. the mesh fineness and the covariance characteristic length using linear basis functions and 10 points' quadrature rule.

The covariance function is estimated back from the eigenvalues and eigenfunctions computed. The obtained covariance function is compared with the true covariance function with characteristic length $l_{c,Cov} = 0.5$ on figure 6.7 and with characteristic length $l_{c,Cov} = 0.25$ on figure 6.8. Again, the obtained covariance fits relatively well the true covariance function. However, the differences between the true and recomputed covariance function are greater, especially for small distances. The error increases when the co-

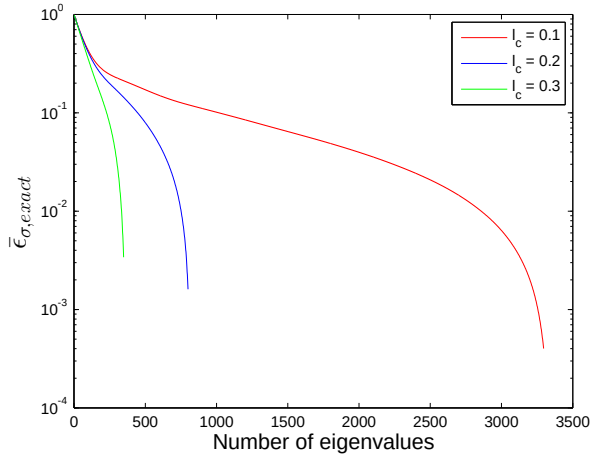

(a) Euclidean norm ($l_{c,Cov} = 0.5$)

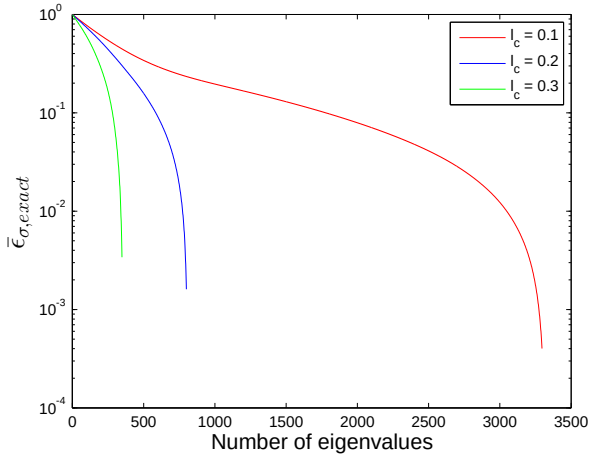

(b) Euclidean norm ($l_{c,Cov} = 0.25$)

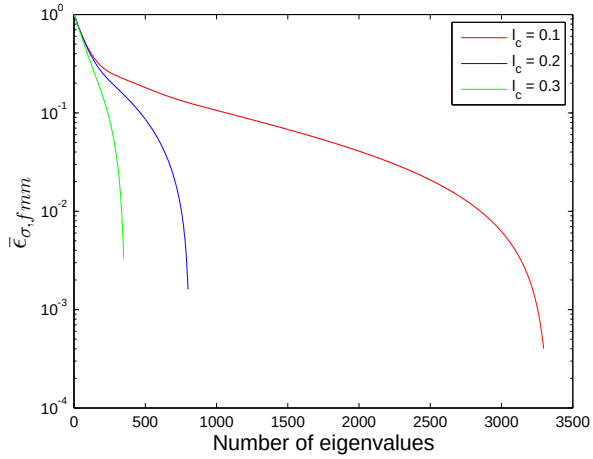

(c) FMM ($l_{c,Cov} = 0.5$)

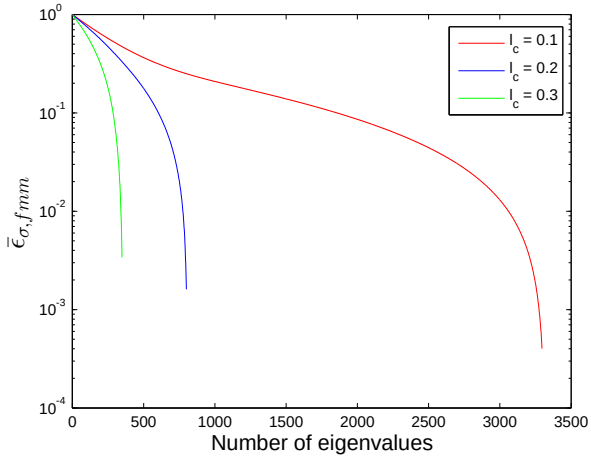

(d) FMM ($l_{c,Cov} = 0.25$)

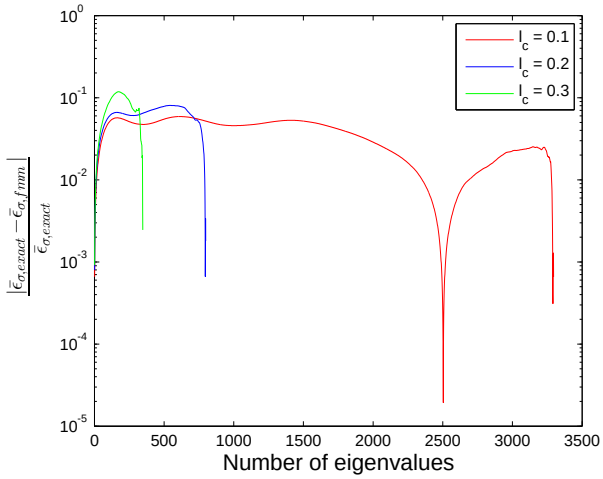

(e) $\frac{|\bar{\epsilon}_{\sigma,FMM} - \bar{\epsilon}_{\sigma,exact}|}{\bar{\epsilon}_{\sigma,exact}}$ for $l_{c,Cov} = 0.5$

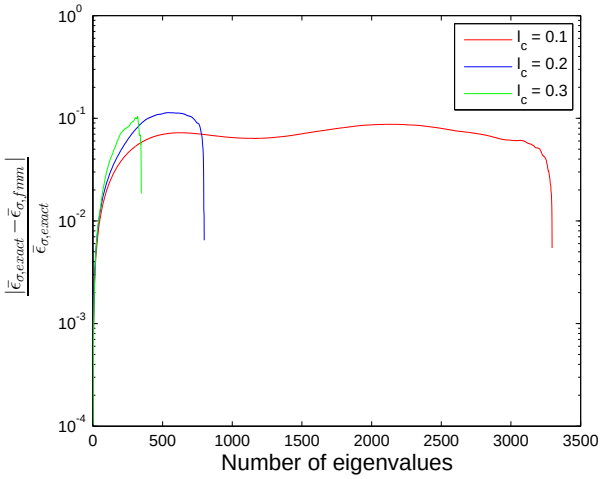

(f) $\frac{|\bar{\epsilon}_{\sigma,FMM} - \bar{\epsilon}_{\sigma,exact}|}{\bar{\epsilon}_{\sigma,exact}}$ for $l_{c,Cov} = 0.25$

Figure 6.2: Comparison of the errors made when computing the exact distances, using euclidean norm, and approximating distances using FMM, constant basis functions and 1 point quadrature rule.

variance characteristic length is smaller.

Due to this analysis and taking into account the long computation times induced by the new method, only the first method will be used in the next chapter to create the random field on 3D surfaces.

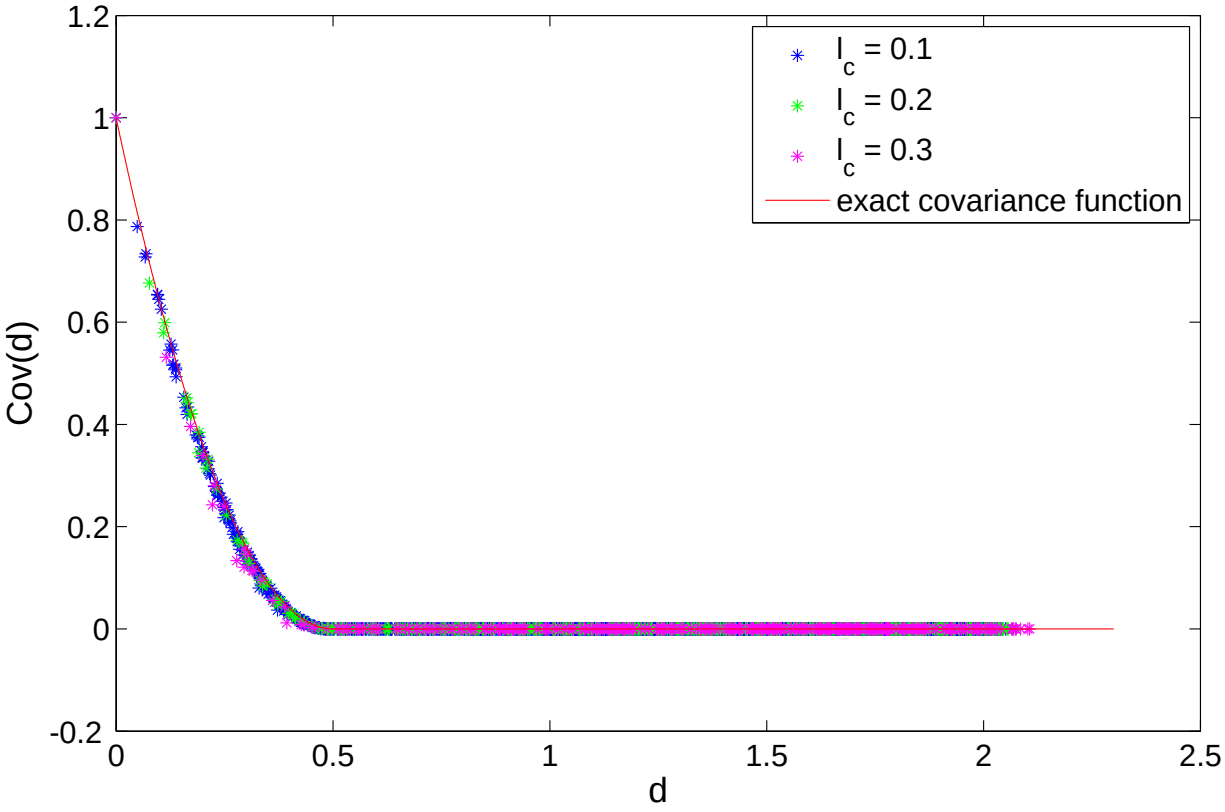

Figure 6.3: Reconstruction of the covariance function of characteristic length $l_{c,Cov} = 0.5$ using constant basis functions and 1 quadrature point.

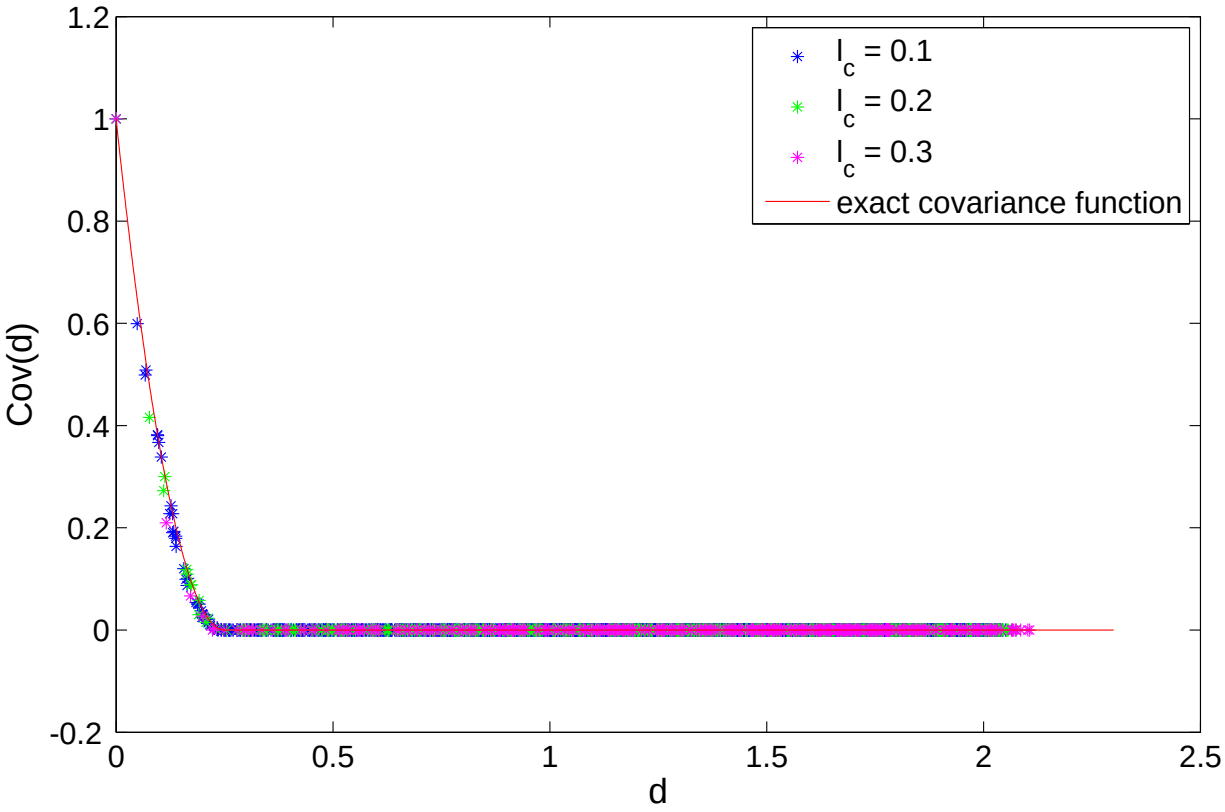

Figure 6.4: Reconstruction of the covariance function of characteristic length $l_{c,Cov} = 0.25$ using constant basis functions and 1 quadrature point.

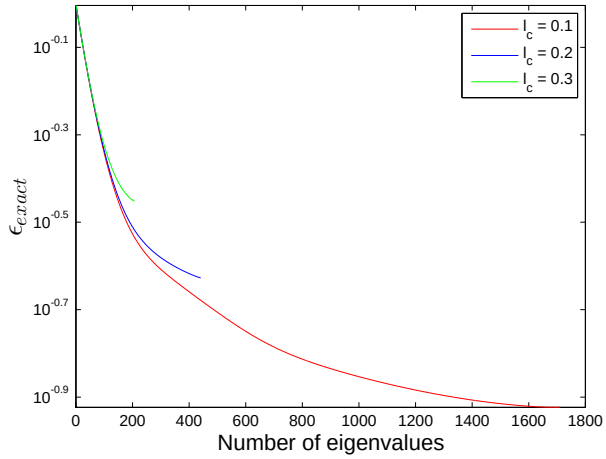

(a) Euclidean norm ($l_{c,Cov} = 0.5$)

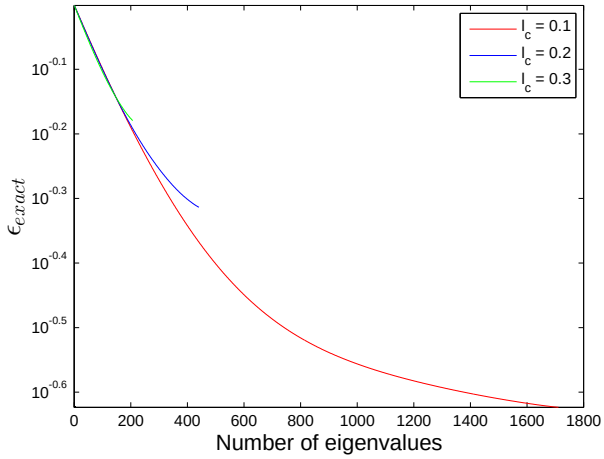

(b) Euclidean norm ($l_{c,Cov} = 0.25$)

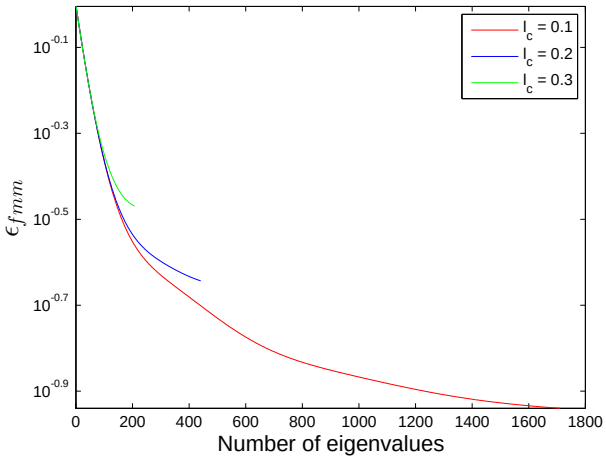

(c) FMM ($l_{c,Cov} = 0.5$)

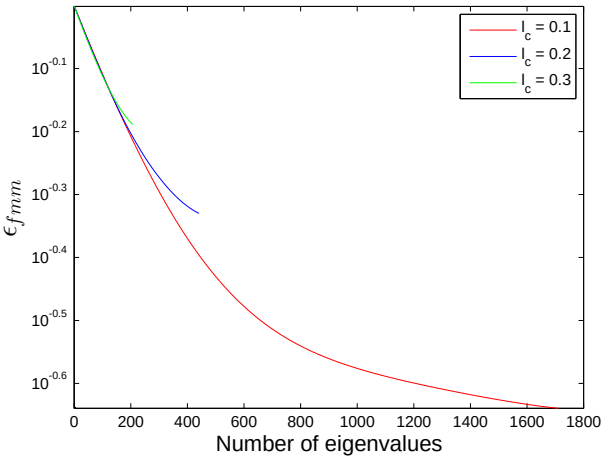

(d) FMM ($l_{c,Cov} = 0.25$)

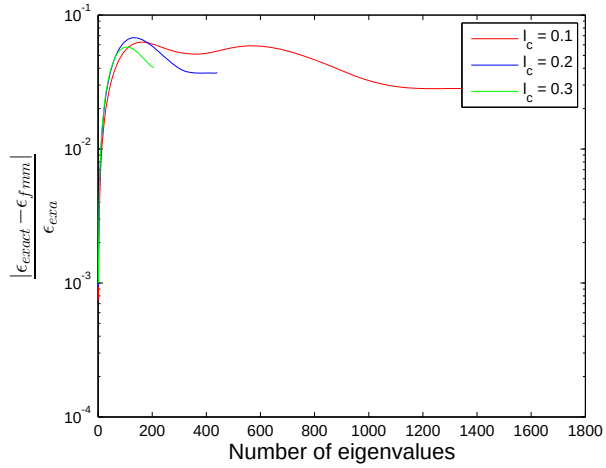

(e) $\frac{|\bar{\epsilon}_{\sigma,FMM} - \bar{\epsilon}_{\sigma,exact}|}{\bar{\epsilon}_{\sigma,exact}}$ for $l_{c,Cov} = 0.5$

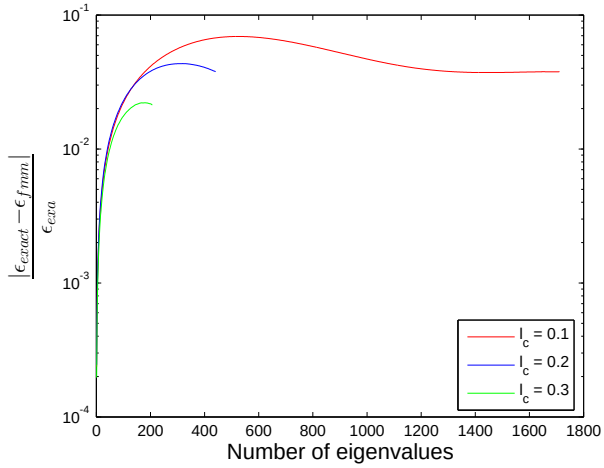

(f) $\frac{|\bar{\epsilon}_{\sigma,FMM} - \bar{\epsilon}_{\sigma,exact}|}{\bar{\epsilon}_{\sigma,exact}}$ for $l_{c,Cov} = 0.25$

Figure 6.6: Comparison of the errors made when computing the exact distances, using euclidean norm, and approximating distances using FMM, linear basis functions and 10 points quadrature rule.

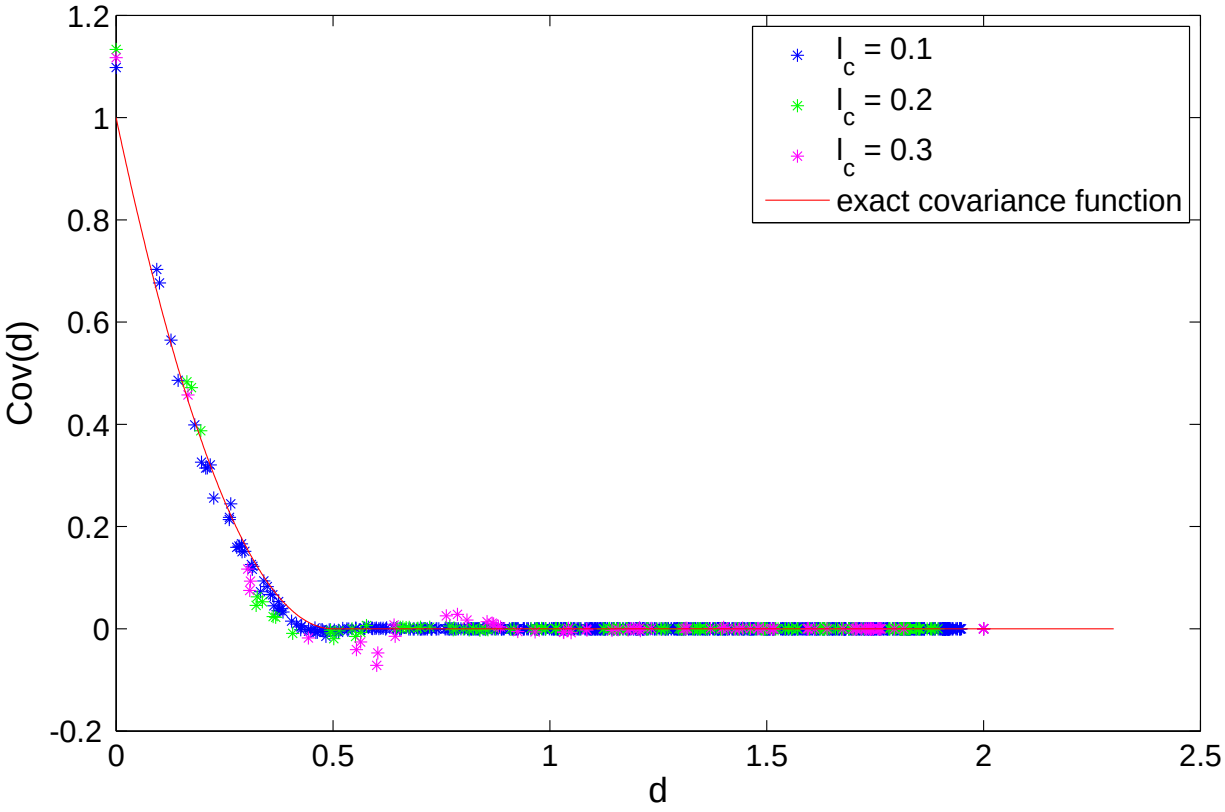

Figure 6.7: Reconstruction of the covariance function of characteristic length $l_{c,Cov} = 0.5$ using linear basis functions and 10 quadrature points.

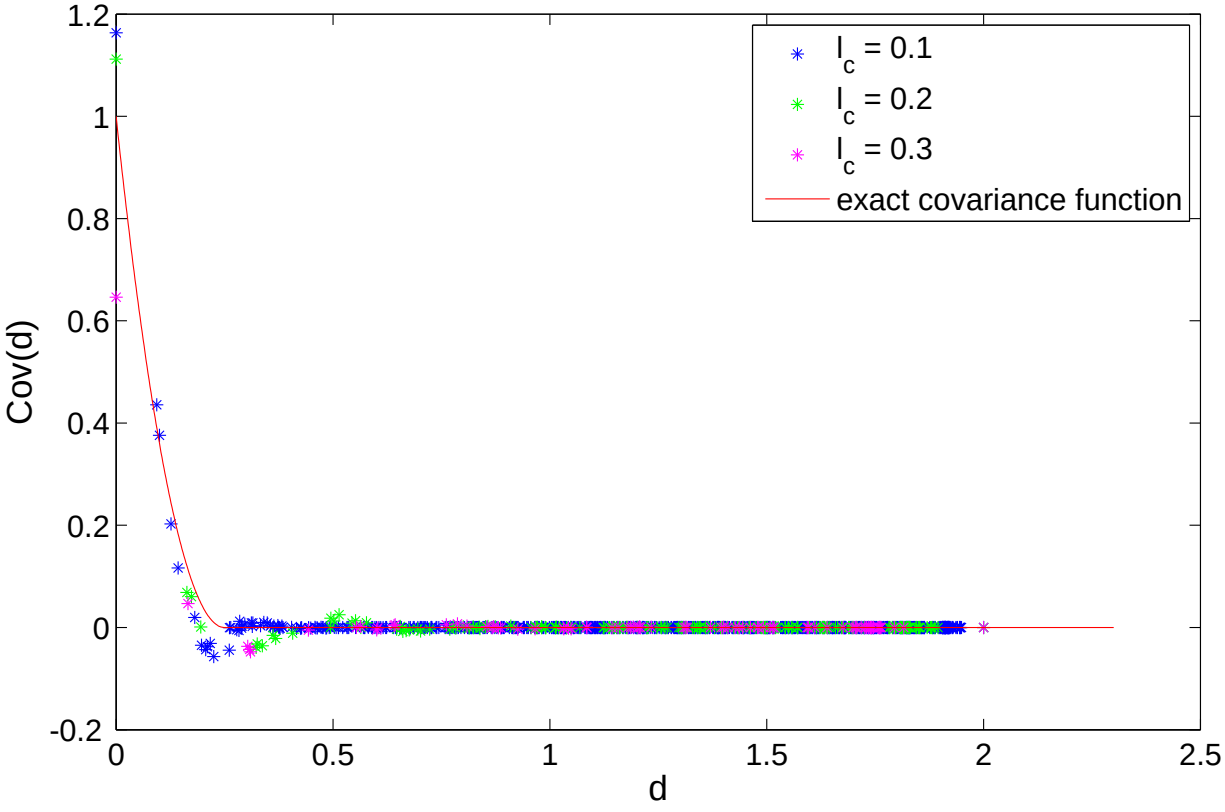

Figure 6.8: Reconstruction of the covariance function of characteristic length $l_{c,Cov} = 0.25$ using linear basis functions and 10 quadrature points.

Chapter 7

Numerical solution and industrial applications

The goal of this thesis is to analyse the mechanical responses of a loaded composite object whose properties are uncertain. The first section describes the different programs used in the analysis and explains how they were used in the framework of this thesis. The second section details the methods used to obtain the mechanical responses of the composite object. It also presents my personal contribution to the program. The third and the fourth sections present results obtained with the program. The third section analyses the mechanical responses of a chair with variable FVF. The fourth section analyses the mechanical responses of the same chair. In this section, the FVF is constant but the angle of the plies with respect to the main direction are uncertain.

7.1 Various software used

Many programs do interact in order to produce the desired mechanical analysis. Let's present them in a few words.
`Samcef` is a 3D finite element software which models and simulates mechanical and thermal responses of objects [53]. `Samcef` is used to mesh the surface of the composite object, define the loading case and compute the mechanical response of the composite object.
`Gmsh` is a free, 3D finite element mesh generator. Its four modules allow to define a geometry, mesh it, interface with solvers and visualise results [16]. `Gmsh` is used to mesh the surface of the composite object and represent the mechanical analysis on the surface of the composite object.
`Python` is an open-source programming language allowing multiple functionalities among which scientific programming, text editing and system administration [44]. Python was used to launch the jobs in `Samcef`.
`C++` is an object-oriented language allowing polymorphism, inheritance, interfaces and abstract classes. `C++` is the core of the program realised in this thesis. It interacts with `Samcef` and `Gmsh` and executes all steps, apart from the mechanical tests, needed to obtain the mechanical analysis of composite objects.
`Matlab` and `Octave` are scientific programming languages [35, 40]. They are used to plot numerical results outputted by `C++`.
`Bash` is a command language mostly used on Linux platforms. It allows to automatically create or delete folders and files. It was used to automatically execute binary files produced after compiling the `C++` global classes, run the `Python` file launching the `Samcef` mechanical analysis and store the results in folders.

Those programs are used to model the composite object, analyse its mechanical response and display the analysis. Let's see how the modelling and analysis are realised.

7.2 Workings of Cenaero's program and personal contribution to the program

In order to analyse the mechanical responses of composite objects with uncertain properties, the program must first generate a Gaussian random field. The composite surface is meshed and a Gaussian random field is defined on every element of the mesh. This field impacts the properties of final object. Every element is associated to a laminate. The properties of the laminate depends on the value of the Gaussian field on the triangle. When laminates have been defined for every triangle on the mesh, the program computes the mechanical responses of the composite object and exploits the results. This procedure is summarised in figure 7.1. My contributions are the mechanical analysis of composite objects whose properties are uncertain and the extension of the random field generation method.

Let's now detail every step in the procedure : the generation of the Gaussian random field, the computation of the properties of an element and the exploitation of the mechanical analysis.
The Gaussian random field is defined by its covariance function. Cenaero's program allows the user to choose between two covariance functions. The first is a Gaussian function depending on the isotropic or anisotropic distance $d(\boldsymbol{x}, \boldsymbol{y})$ between node $\boldsymbol{x}$ and node $\boldsymbol{y}$:

$$Cov(\boldsymbol{x}, \boldsymbol{y}) = \sigma^2 \exp\left(\frac{-d(\boldsymbol{x}, \boldsymbol{y})}{l_{c,Cov}}\right)$$

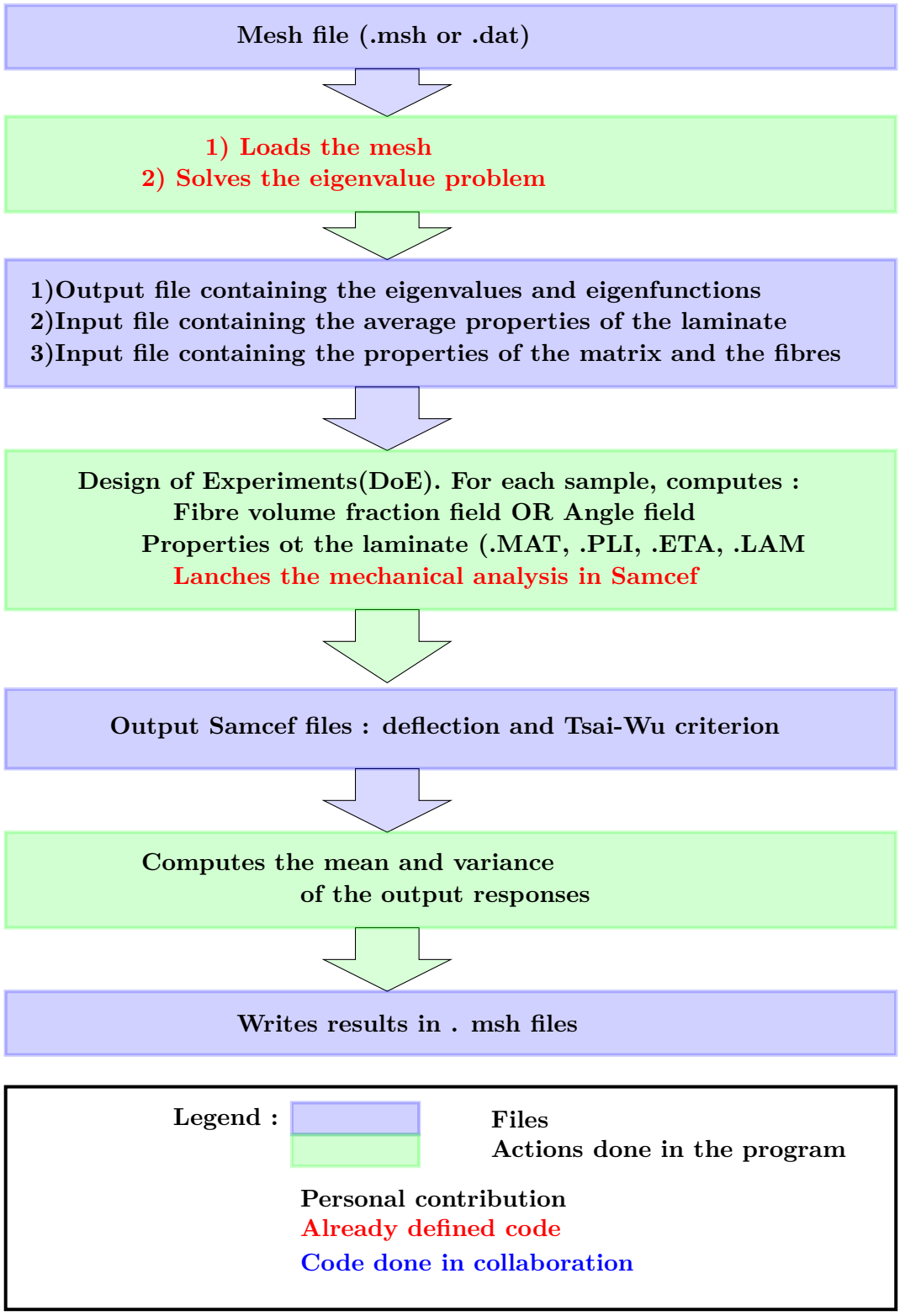

Figure 7.1: Summarised sequential diagram for the mechanical analysis of a composite object

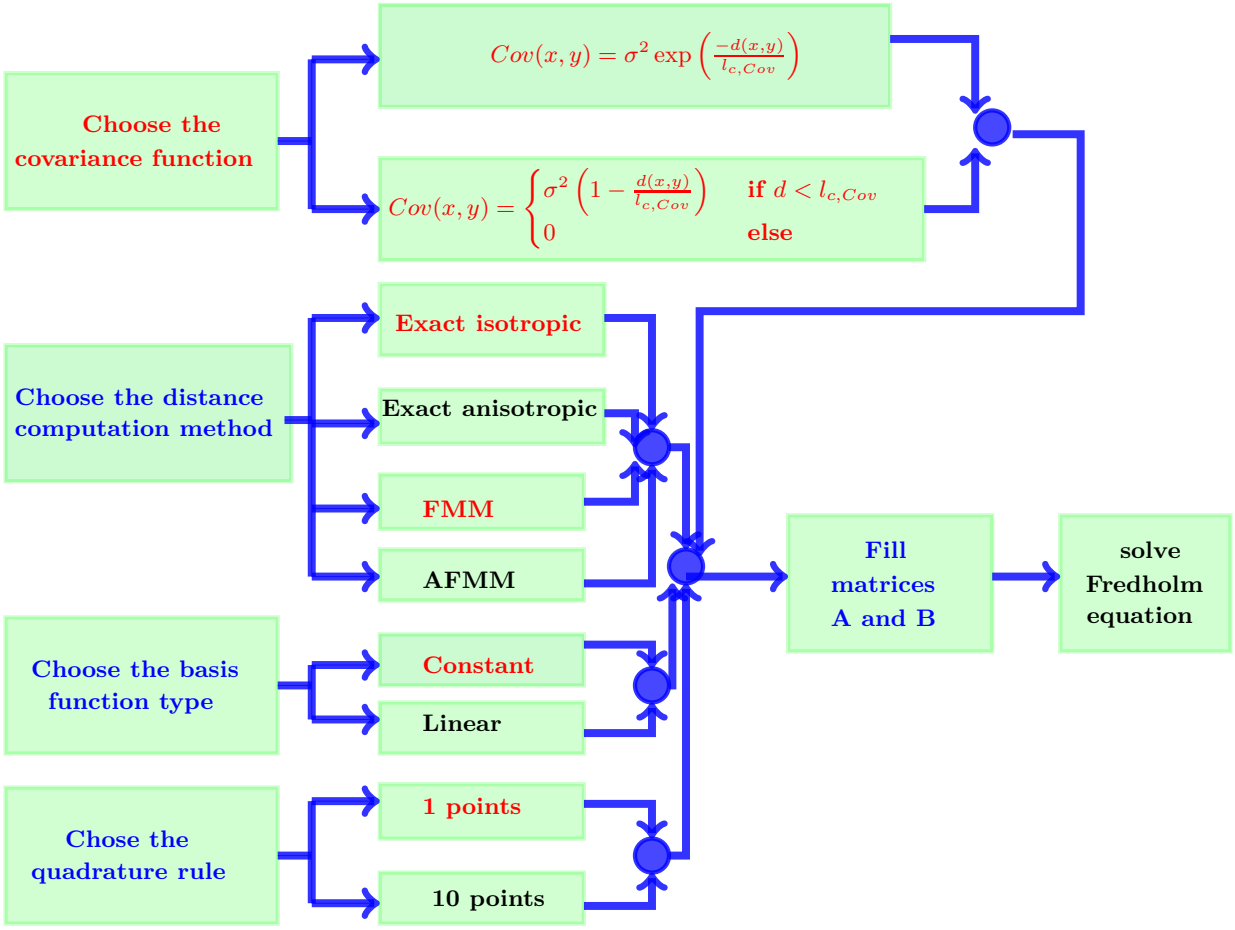

Figure 7.2: Summarised sequential diagram leading to the solution of the Fredholm Equation

The second covariance function approximates the Gaussian function by:

$$Cov(\boldsymbol{x}, \boldsymbol{y}) = \begin{cases} \sigma^2 \left(1 - \frac{d(\boldsymbol{x},\boldsymbol{y})}{l_{c,Cov}}\right)^2 & \text{if } d < l_{c,Cov} \\ 0 & \text{else} \end{cases} \tag{7.1}$$

The distances were first computed using Euclidean norm (2D surfaces) or FMM (2D and 3D surfaces). I extended the distance computation methods to allow anisotropic distance computations (either exact, for 2D surfaces, or approximate using AFMM, for 2D and 3D surfaces). Once the field has been totally described, a discrete random field can be obtained by solving the discrete second order Fredholm equation. This equation involves integrals defined in terms of basis functions and the covariance function. The basis functions were first defined constant and the integrals computed using one-point quadrature rule. Hoping to increase the accuracy, I defined linear basis functions and a 10-points quadrature rule. The first step is summarised in figure 7.2.
The Gaussian random field is defined on every element of the mesh. The user can either choose a variable FVF or add noise to the angles between the plies and the main direction. When the FVF varies, every element of the mesh is characterised by a different FVF. Every element is thus associated with a different composite material. The properties of this composite material are computed using the rule of mixtures. Every element is also associated with a ply stacking sequence. This ply stacking sequence is almost the same as the ply stacking sequence of the deterministic composite object. The only difference comes from the variable properties of the composite material. When the angles of the plies are uncertain, the angles of the ply stacking sequence associated with the element are different from the original angles. However, the material and thickness of the plies are the identical from the original ply stacking sequence. The second step is summarised by figures 7.3 (variable FVF) and 7.4 (variable angles of plies with respect to the main direction).
Several fields and the associated composite objects are defined. Once the mechanical analysis has been realised for all of them, a statistical analysis is made. It allows to check whether the materials respects the specifications in the average case. It also allows to give the fraction of objects that will not respect the specifications. The average case can be obtained by averaging the mechanical responses of the different objects on the mesh. The deviation with respect to the average is defined by computing the deviation of mechanical responses on the mesh. Finally, the convergence of the results is demonstrated by showing the evolution of the maximum variance on the mesh depending on the number of objects taken into account. This last step is summarised on figure 7.5.

Now that the program has been presented, it will be used to analyse the deflection and failure criterion of a reinforced panel with uncertain FVF.

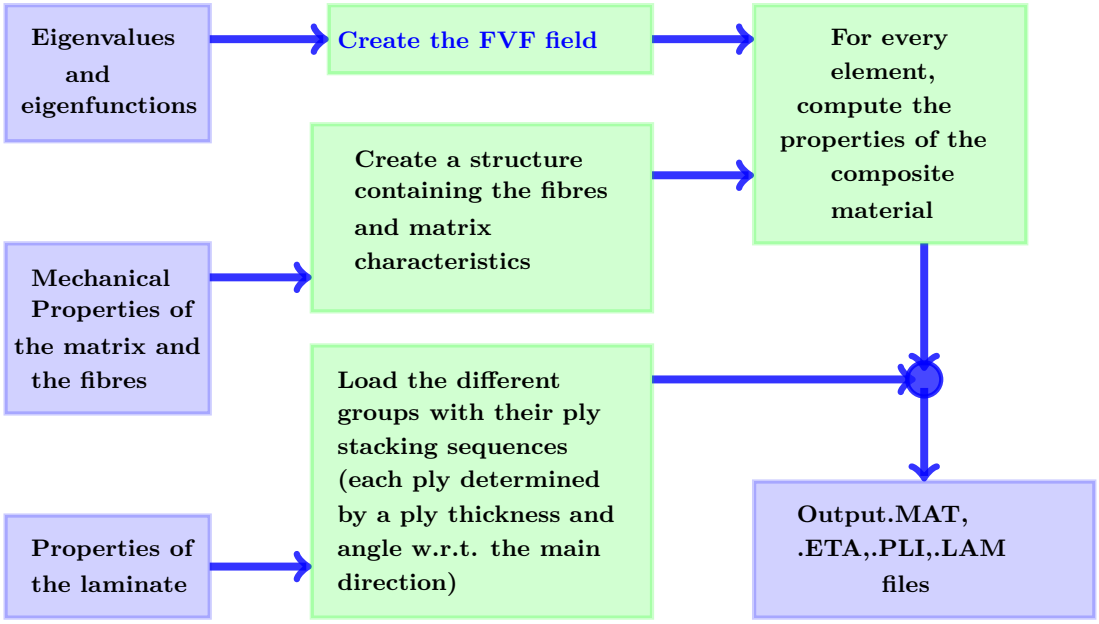

Figure 7.3: Summarised sequential diagram for the description of the laminate to `Samcef` when the FVF is uncertain.

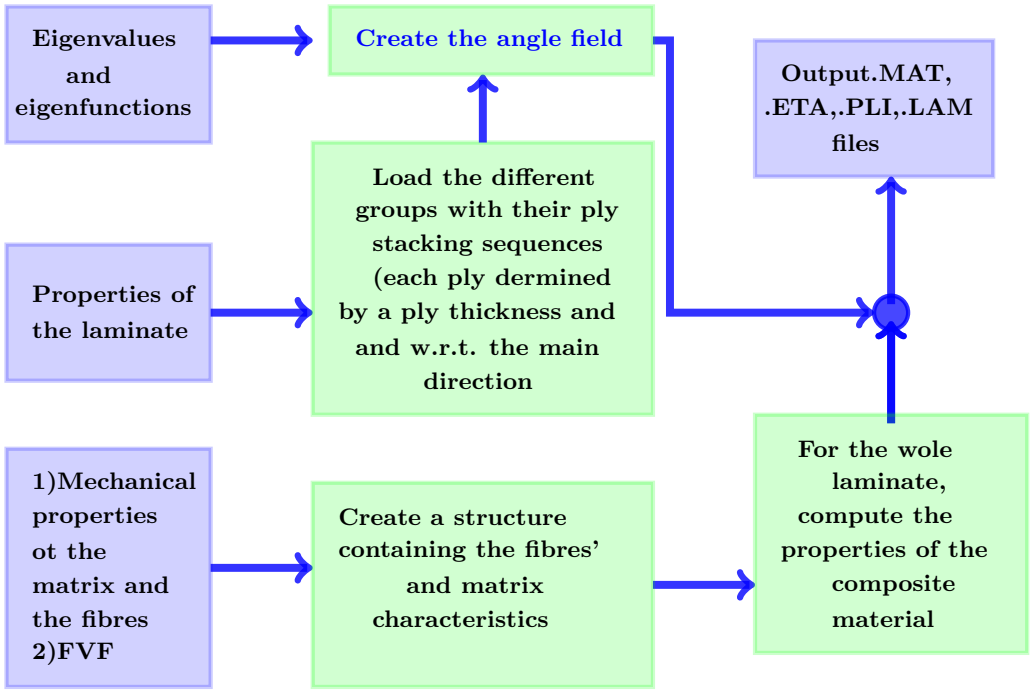

Figure 7.4: Summarised sequential diagram for the description of the laminate to `Samcef` when the angle of the plies w.r.t. the main direction are uncertain.

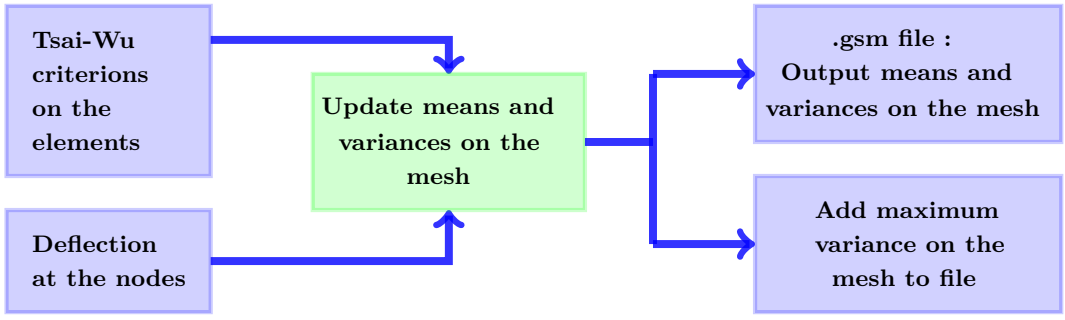

Figure 7.5: Summarised sequential diagram to obtain statistical analysis of the mechanical responses.

7.3 Analysis of the mechanical response of a chair whose FVF is uncertain

The second mechanical analysis is made on a composite chair whose geometry is shown on figure 7.6. It is made of 25 zones with different stacking sequences of unidirectional plies. Zones on the left, along the edge of the chair, have the same stacking sequence as zones on the right along the opposite edge. Strip zones have the same stacking sequence. Unidirectional plies take four possible orientations: 0°, 45°, 90°and 135°. The zones are made of different number of plies uniformly distributed over the four possible orientations. The number of plies per zone is given in table 7.1. The composite material is made of flax fibres and epoxy. Their properties, extracted from [56, 59], are given in table 7.2. After fixing the chair at four points on the seat (see figure 7.6), uniform pressures equivalent to 200 kg and 75 kg are applied to the seat and the back.

15	16	10	16	15
14	16	9	16	14
13	16	8	16	14
12	16	9	16	12
11	16	11	16	11

Table 7.1: Number of plies associated with each of the zones shown on figure 7.6.

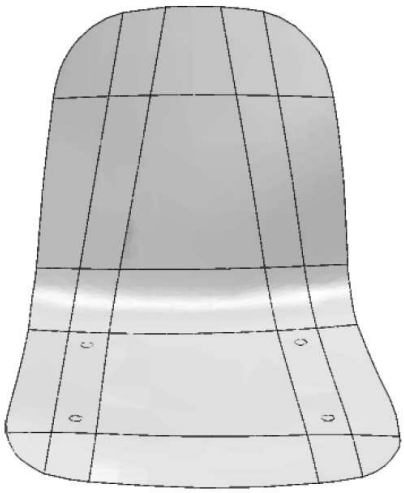

Figure 7.6: Geometry of a chair.

	Density $[Mg/m^3]$	Young modulus (GPa)	Poisson modulus	Shear modulus (GPa)	Tensile strength (GPa)	Compressive strength (GPa)
Flax fibre	1.4	60	0.2	25	0.5	0.83
Epoxy	1.1	3.45	0.35	1.277	0.049	0.049

Table 7.2: Mechanical properties of flax fibres and epoxy.

The goal is to analyse the effect of uncertain FVF on mechanical responses of the chair. The mean value of FVF is fixed to 0.5. The covariance function is given by equation (7.1). The covariance function is isotropic and the distance computed using FMM. The integration method uses constant basis functions and 1-point quadrature rule.
Some Gaussian random fields, with different covariance characteristic lengths $l_{c,Cov}$, are given on figure 7.7. The fields are close to the original Gaussian random fields. Indeed, as shown on figure 7.8, the mean error variance is low when using a large fraction of the eigenvalues. The zones in red represent the areas where the zero mean random process takes high values. The zones in blue represent the areas where it takes the smallest values. As $l_{c,Cov}$ increases, the area of similar values become larger. This in term, leads to larger resin rich zones and voids or resin poor zones. Increasing $l_{c,Cov}$ also impacts the computation time as it affects the sparsity of matrices involved in the generalised eigenvalue problem (see table 7.3).

$l_{c,Cov}$	50	75	100
Chair	98.74 %	97.42%	95.74 %

Table 7.3: Sparsity of $\boldsymbol{A}$ w.r.t. the covariance characteristic length $l_{c,Cov} = \{50, 75, 150\}$

Once the random field has been generated and the properties of the composite object have been computed, the chair is loaded. The mechanical analysis is then realised. The mean and variance of the deflection and Tsai-Wu criterion fields are analysed after 300 samples. The fields are shown on figure 7.9 when $l_{c,Cov} = 50$ and $\sigma^2_{FVF} = 0.05$. The maximum deflection occurs at the top of the chair and the maximum Tsai-Wu criterion near the fixation points. The maximum deflection is relatively important and the Tsai-Wu criterion reaches value higher than 1. There is thus a risk of failure at the back fixation points, where this criterion is the highest. Figure 7.9 also show the evolution of the variance with respect to the number of samples. As the convergence is observed, the number of samples should be sufficient. The analysis can be made again using different covariance characteristic lengths and variances. Table 7.4 shows that the uncertainty in the response increases with the characteristic length and the variance of FVF.

	σ^2_{FVF}	$l_{c,Cov} = 25$	$l_{c,Cov} = 50$	$l_{c,Cov} = 75$	$l_{c,Cov} = 100$	$l_{c,Cov} = 150$
Deflection	0.05	0.57%	0.57%	0.57%		
	0.1				1.05%	3.5%
Tsai-Wu criterion	0.05	1.49%	1.36%	1.49%		
	0.1				2.81%	3.7%

Table 7.4: Standard deviation of deflection and Tsai-Wu criterion over their mean value for 300 samples (in %).

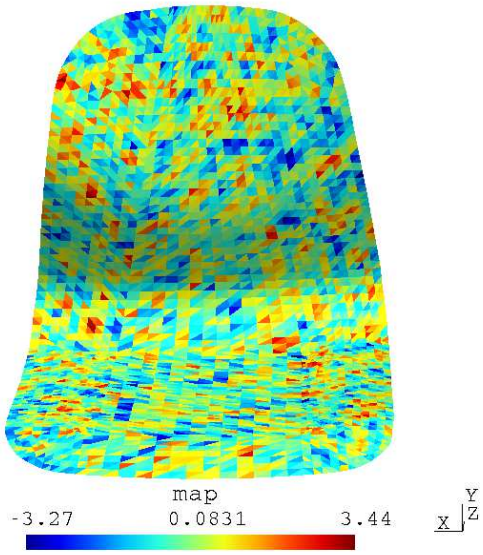

(a) $l_{c,Cov} = 25$

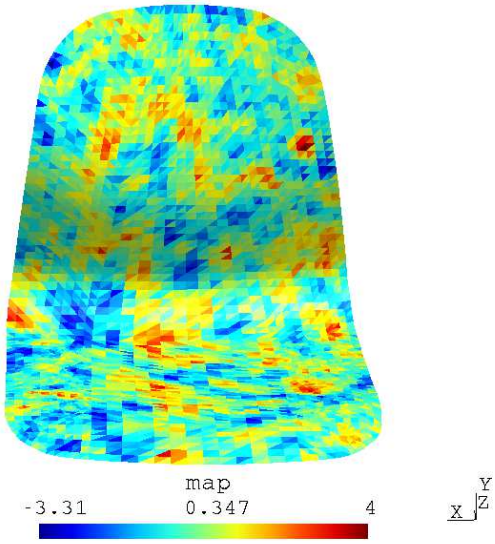

(b) $l_{c,Cov} = 50$

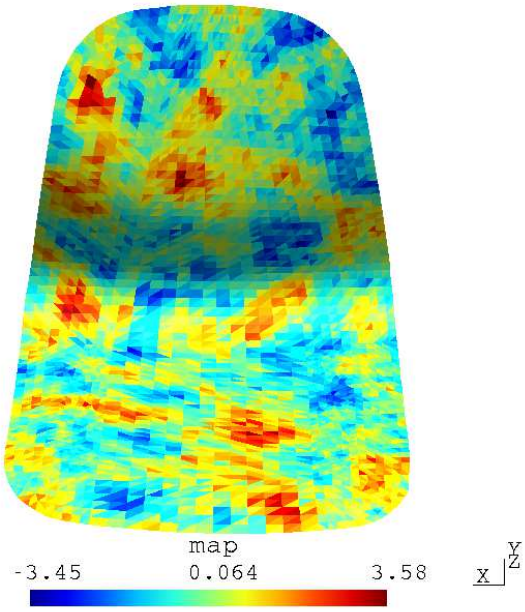

(c) $l_{c,Cov} = 75$

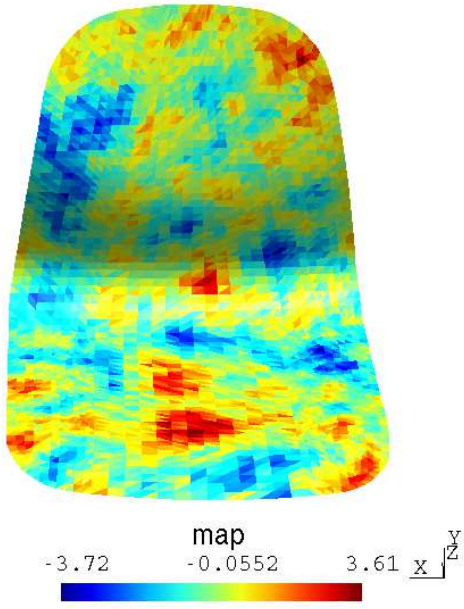

(d) $l_{c,Cov} = 100$

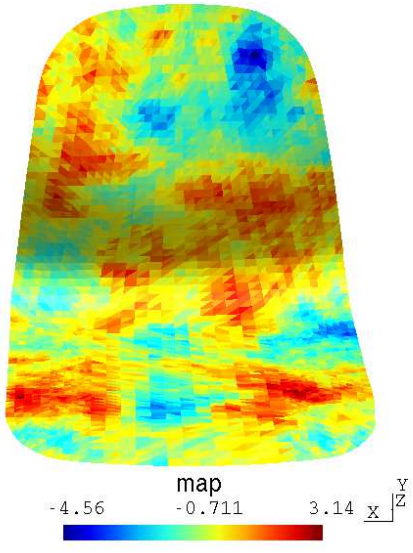

(e) $l_{c,Cov} = 150$

Figure 7.7: Random field with zero mean and standard deviation one. Up to down and left to right: the covariance characteristic length is given by $l_{c,Cov} = 25, 50, 75, 100, 150$

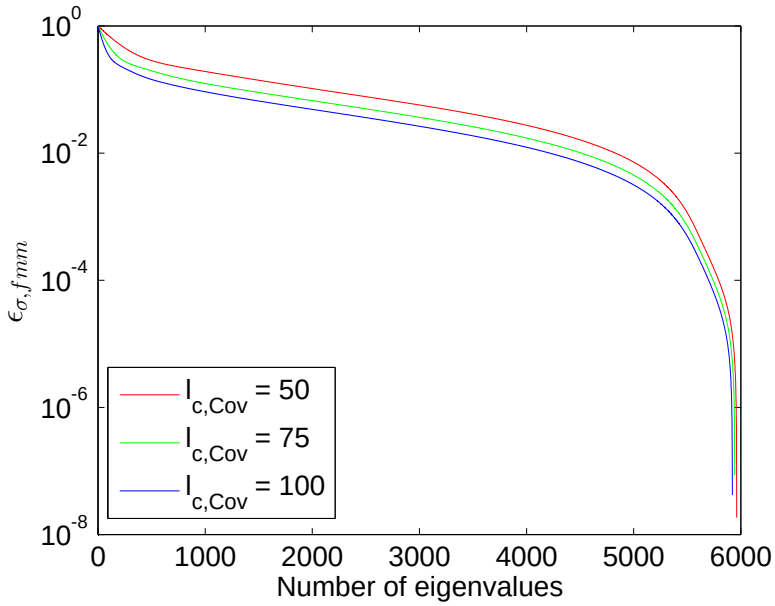

Figure 7.8: Mean error variance (chair with isotropic covariance function)

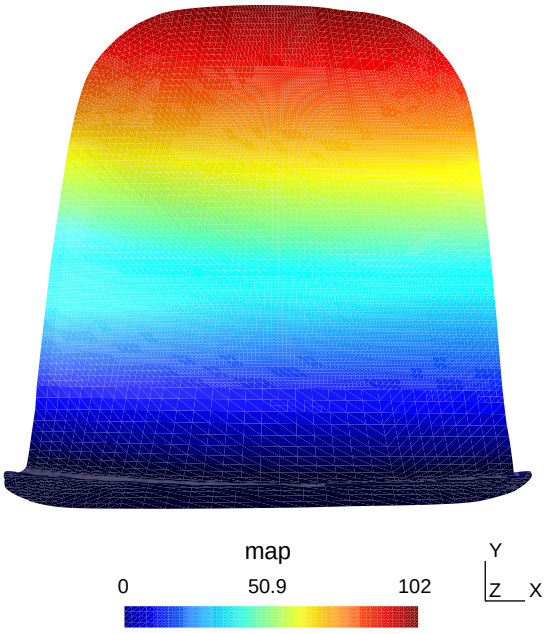

(a) Mean deflection (in mm)

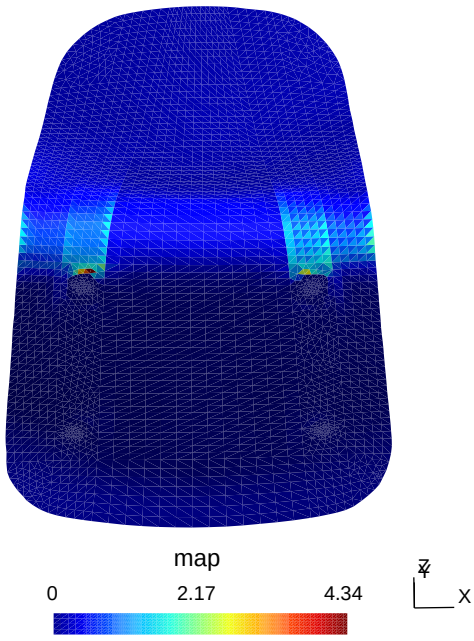

(b) Mean of Tsai-Wu Criterion

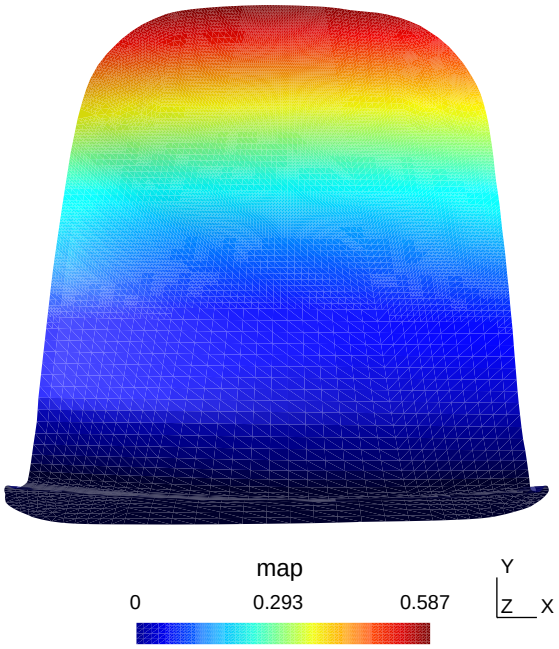

(c) Variance of deflection (in mm)

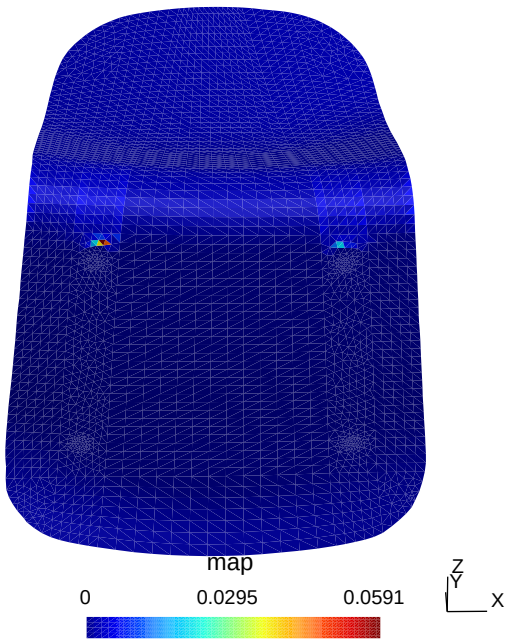

(d) Variance of Tsai-Wu criterion

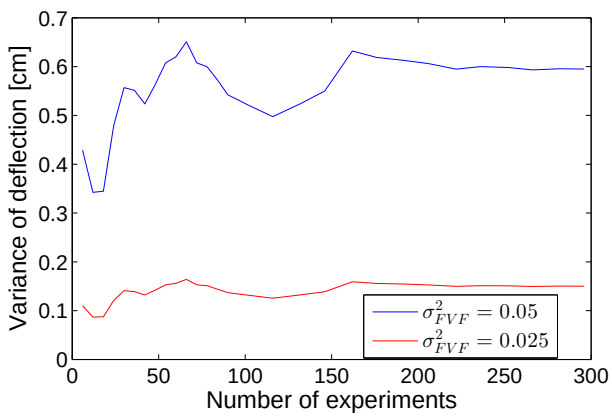

(e) Maximum variance of deflection w.r.t. the number of experiments (in mm)

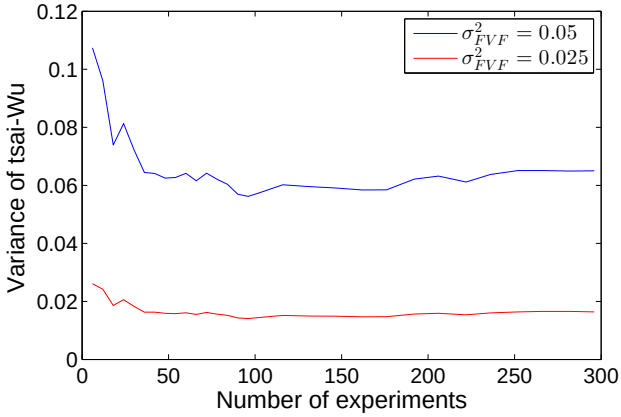

(f) Maximum variance of Tsai-Wu criterion w.r.t. the number of experiments

Figure 7.9: Maximum displacement and Tsai-Wu criterion for $l_{c,Cov} = 50$ and $\sigma^2_{FVF} = 0.05$ (chair application)

7.4 Analysis of the mechanical response of a chair whose plies's angles are uncertain

The third mechanical analysis is made on the chair shown on figure 7.6. This time, all plies take orientation 90°. The components of the composite and the loads remain the same but the FVF becomes constant. The FVF is set to 25% with 81.25% of fibres in the main direction. This time, the goal is to analyse the effect of uncertain angle of the plies on the mechanical response of the chair. The mean value of the angle is the one of the original ply. The covariance function, given by equation (7.1), is anisotropic and the distance computed using AFMM. The integration method uses constant basis functions and 1-point quadrature rule.
Some Gaussian random fields associated with distance $d(\boldsymbol{x}, \boldsymbol{y}) = \sqrt{(x_1 - y_1)^2 + 2(x_2 - y_2)^2}$ and different covariance lengths $l_{c,Cov}$, are given on figure 7.11. The fields are close to the original Gaussian random fields. Indeed, as shown on figure 7.10, the mean error variance is low when using a large fraction of the eigenvalues. As previously, zones in red (blue) represents the areas where the zero mean random process takes high (low) values. Those zones form ellipses with major axis in the direction of the fibres and minor axis perpendicular to the major axis. As $l_{c,Cov}$ grows, the ellipses grow. This, in term, leads to larger zones where fibre angles deviate in the same direction from the original angle. As previously, $l_{c,Cov}$ affects the sparsity of matrices involved in the generalised eigenvalue problem (see table 7.5). Results are similar to the FVF case.

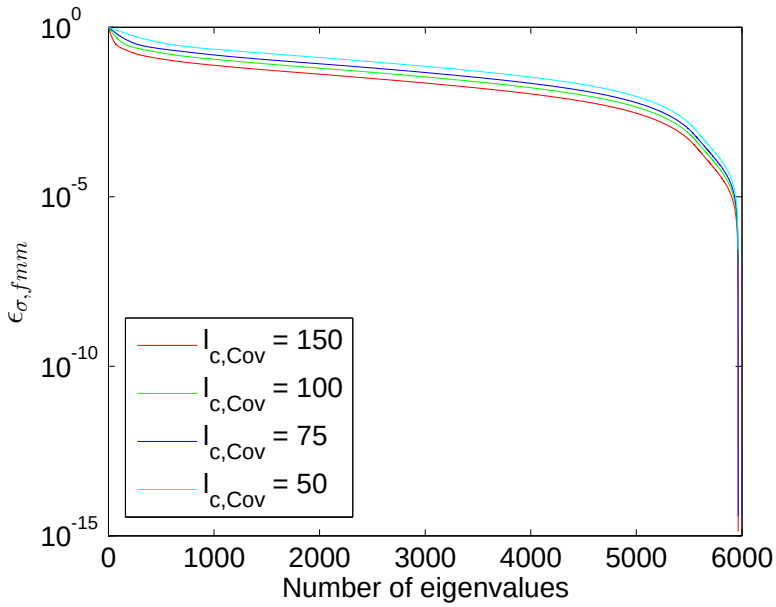

Figure 7.10: Mean error variance (chair with anisotropic covariance function)

$l_{c,Cov}$	50	75	100	150
Chair	99.06 %	98.1%	96.87%	93.87%

Table 7.5: Sparsity of $\boldsymbol{A}$ w.r.t. the covariance characteristic length $l_{c,Cov} = \{50, 75, 100, 150\}$

Once the angle of the plies have been computed, the chair is loaded and the mechanical analysis is realised. The mean and variance of the deflection and Tsai-Wu criterion fields are analysed after 400 samples. The fields are shown on figure 7.12 when $l_{c,Cov} = 50$ and $\sigma^2_{angle} = 5$. The maximum deflection occurs at the top of the chair and the maximum Tsai-Wu criterion near the fixation points. Figure 7.12 also show the evolution of the variance with respect to the number of samples. The convergence occurs later than in the uncertain FVF case. The analysis can be made again using different covariance characteristic lengths and variances. The larger the angle variance, the more samples are needed before convergence of the Monte Carlo method. Table 7.6 shows that the uncertainty grows depending on the variance of the angle. Even for relatively large angle, the uncertainty on the displacement remains negligible. The uncertainty on the failure criterion is more pronounced.

	$\sigma^2_{angle} = 1$	$\sigma^2_{angle} = 5$	$\sigma^2_{angle} = 10$
Deflection	0.032%	0.162%	0.32%
Tsai-Wu criterion	0.79%	3.617%	6.583%

Table 7.6: Standard deviation of deflection and Tsai-Wu criterion over their mean value for 400 samples and $l_{c,Cov} = 50$ (in %)

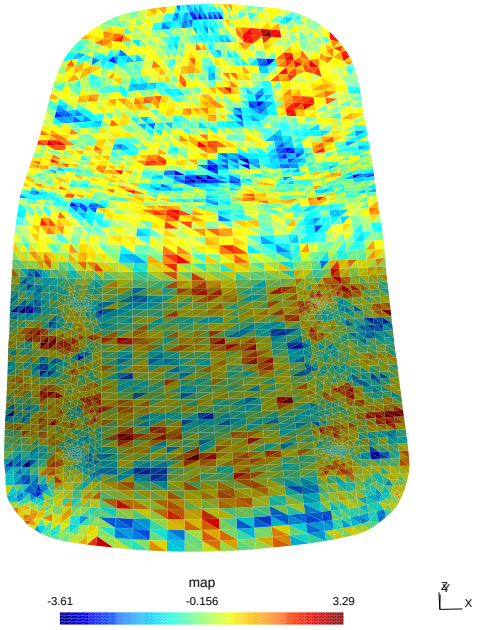

(a) $l_{c,Cov} = 50$

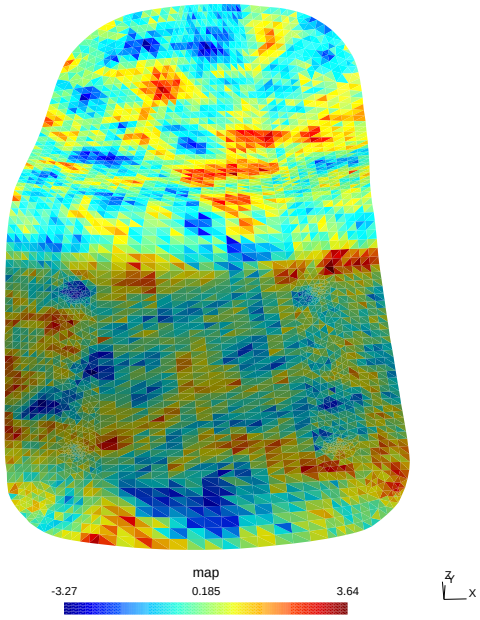

(b) $l_{c,Cov} = 75$

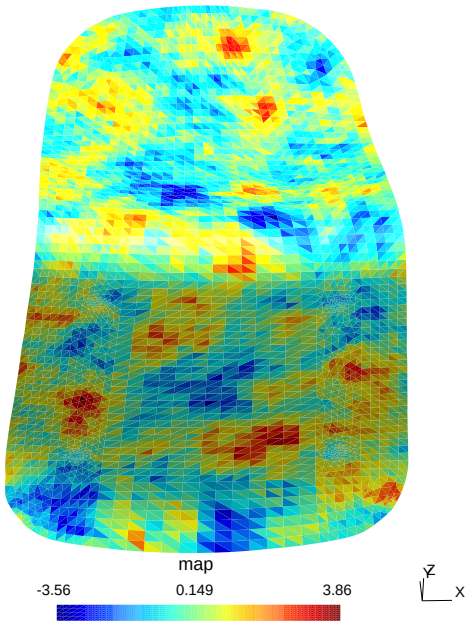

(c) $l_{c,Cov} = 100$

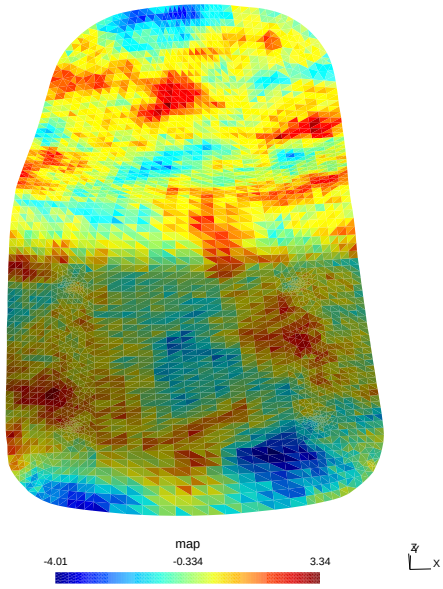

(d) $l_{c,Cov} = 150$

Figure 7.11: Random field with zero mean, standard deviation, fibres in direction y and anisotropic norm $d(\boldsymbol{x}, \boldsymbol{y}) = \sqrt{(x_1 - y_1)^2 + 2(x_2 - y_2)^2}$. Up to down and left to right: the covariance characteristic length is given by $l_{c,Cov} = 50, 75, 100, 150$

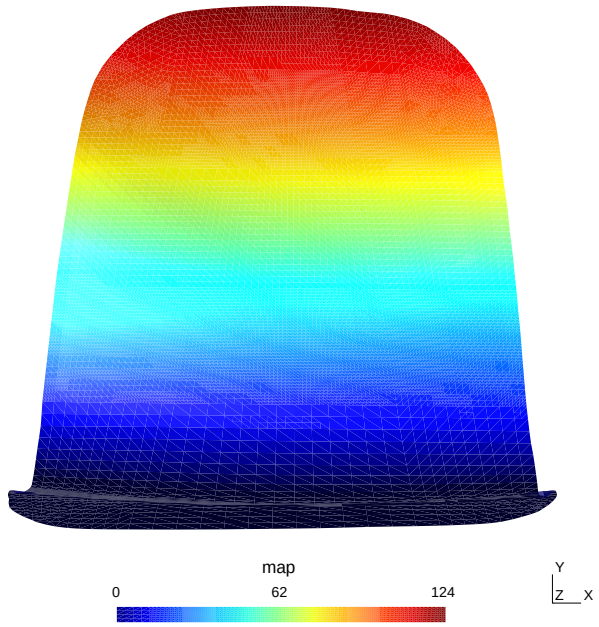

(a) Mean deflection (in mm)

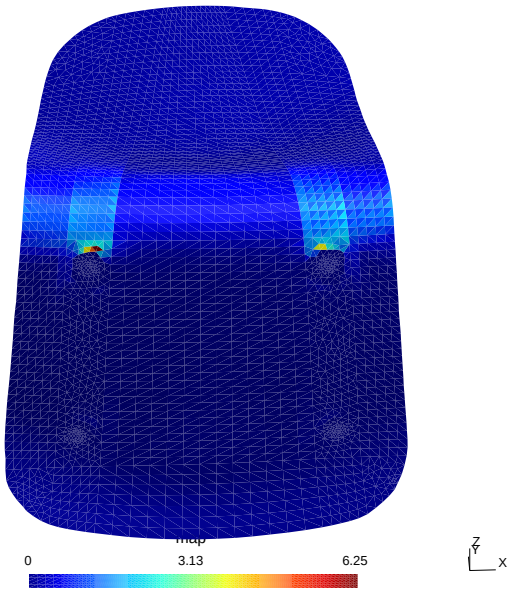

(b) Mean of Tsai-Wu Criterion

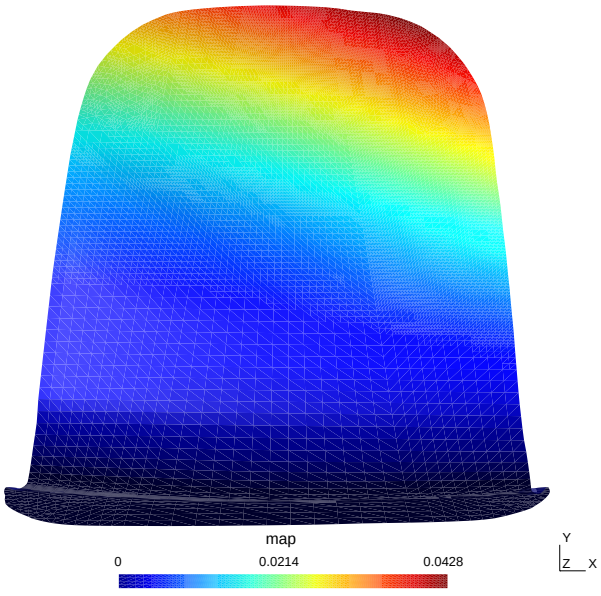

(c) Variance of deflection (in mm)

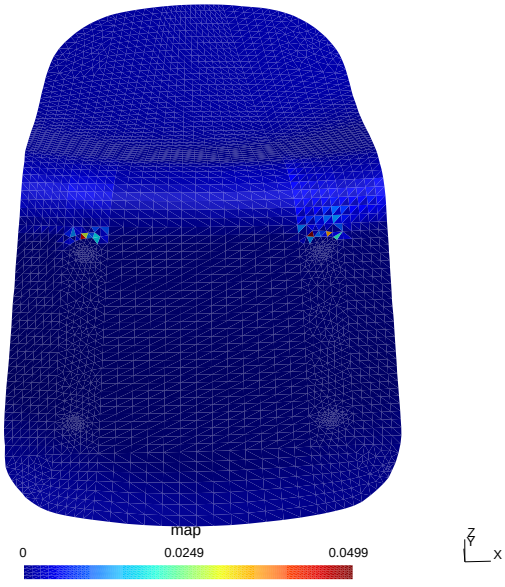

(d) Variance of Tsai-Wu criterion

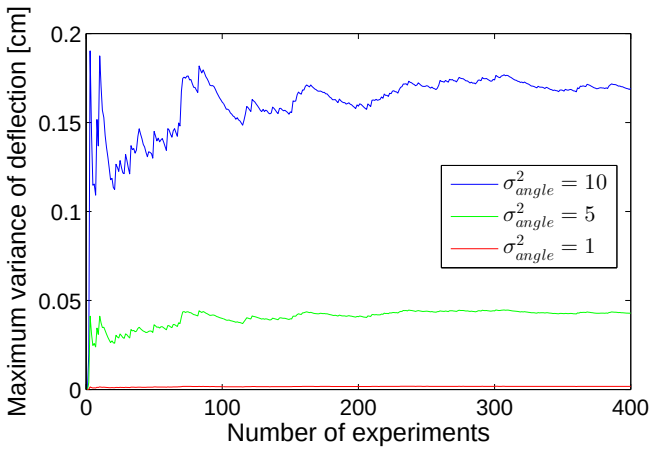

(e) Maximum variance of deflection w.r.t. the number of experiments (in mm)

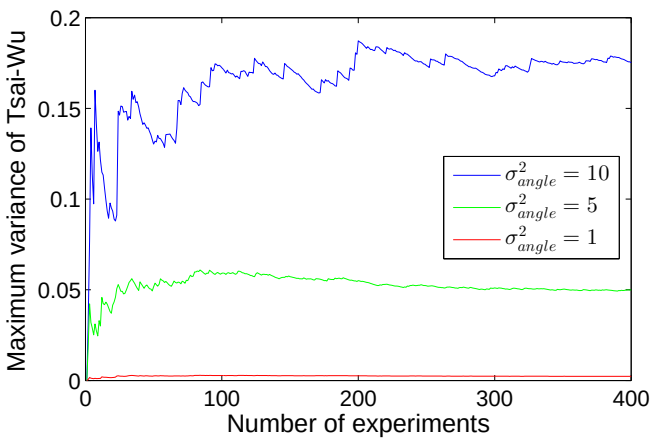

(f) Maximum variance of Tsai-Wu criterion w.r.t. the number of experiments

Figure 7.12: Maximum displacement and Tsai-Wu criterion for $l_{c,Cov} = 50$ and $\sigma^2_{angle} = 5$ (chair application)

Chapter 8

Conclusion

The goal of this thesis is to quantify the effect of uncertainties on the mechanical responses of composite objects. Composite objects are made of different components: the reinforcement and the matrix. The classical mechanical theories modelling heterogeneous materials involve homogenization methods. By analysing the object at different level scales (micro and macro scale of a ply and macro scale of the whole object) they give the mechanical laws describing the behaviour of a composite object, in this thesis a laminate, with known and deterministic properties. The stresses and strains inside the composite object are computed based on the forces and moments under which it is loaded. Taking into account the stresses and strains inside the laminate, the Tsai-Wu criterion allows to quantify the reliability of the object.

In real life, the fibre volume fraction, the angle of the plies and several other properties of the composite object are impacted by uncertainties. Those uncertainties appears during the manufacturing of the object, a complex process involving several steps. They can be generated using the Karhunen-Loève expansion, a series expansion. The larger terms in the series describe the general trend of the field. Smaller terms represent smaller noises with greater frequency. This was shown by determining analytically two random fields.

The uncertainties are evaluated at discrete points on a mesh. The discrete values are obtained by solving a generalized eigenvalue problem involving the numerical evaluation of integrals. One of the integrand involves the covariance function associated with the field. The covariance functions between two points is itself a function of the distance between those points. Because surfaces of composite objects are 3D surfaces, the distances can not be evaluated using Euclidean or exact anisotropic norms. Two algorithm, the Fast Marching Method and the Recursive Fast Marching Method, respectively allow to compute isotropic and anisotropic distances on the surface of the object. The AFMM gives relatively accurate results on 2D surfaces, especially for fine meshes and large distances. The AFMM method seems to perform well on 3D surfaces too.
Once the distances have been computed, the discrete field is evaluated by numerically computing the integrals. Two integration methods have been presented. The first method is a one-point quadrature rule involving constant basis functions. The second method is a ten-points quadrature rule involving linear basis functions. The second method gives inconclusive results with increased time and space complexity. Therefore, only the first method is used in subsequent analysis.

Finally, the goal of this thesis was achieved. Two statistical analysis were conducted on a chair with, one time, uncertain fibre volume fractions and, the other time, uncertain plies' angles. The convergence of the analysis were obtained when using a large number of sample chairs. Both analysis have revealed that the chair is not solid enough and would break at its fixation points. The deflection at the top of the chair is quite large too. Increasing the covariance characteristic length and the variance of the Gaussian random field increases the maximum value of the deflection and Tsai-Wu criterion. The same observations are true when the angle of the plies are variable. However, the effect of uncertain angles on deflection is much smaller than its effect on the Tsai-Wu criterion. The variance of the deflection remains negligible with respect to its maximum value, even for large variances of the field.

Several points are left to consider. Two important parameters of the covariance function associated with the field are the variance and the covariance characteristic length. The values used in this thesis were only chosen to illustrate the method. An other important choice in the computation of the angle field is the definition of the anisotropic distance. Experiments should be conducted to fit the covariance function and the definition of the anisotropic distance to real fields.

A discrete value of the Gaussian random field is associated with each element and thus the laminate defined on the element. All the plies of this laminate are associated with the same discrete value of the Gaussian random field. An interesting field of research would be to investigate what happens when each ply of an element is associated with distinct values of Gaussian random fields. For instance, when the Gaussian random field represents the variability of the angle of plies, the field depends on the direction of the fibres. As the laminate is usually made by stacking plies of different orientations, it would make sense to define an uncertain value for each ply of the element.

The design of the composite object could take into account the variability of the properties. It could be made by solving a constraint optimization problem. For instance, the problem could be to design the lightest object such that the Tsai-Wu criterion remains less than one.

The main contribution of this thesis is the use of the Recursive Fast Marching Method and the Fast Marching Method in the statistical analysis of the mechanical response of composite objects with uncertain properties. A large portion of the work is the creation of a programming interface between the different software.

Bibliography

[1] Florence Aeschelmann. http://news.bio-based.eu/fast-growth-of-based-polymers-production/. In *Bio-based News*, 10 Juni 2015.

[2] Eugene B Belov, Stepan Vladimirovitch Lomov, Ignaas Verpoest, Teo Peters, Dirk Roose, RS Parnas, K Hoes, and H Sol. Modelling of permeability of textile reinforcements: lattice boltzmann method. *Composites Science and Technology*, 64(7):1069–1080, 2004.

[3] Jean-Marie Berthelot. *Matériaux composites–Comportement mécanique et analyse des structures*. Paris, 2012.

[4] Wolfgang Betz, Iason Papaioannou, and Daniel Straub. Numerical methods for the discretization of random fields by means of the karhunen–loève expansion. *Computer Methods in Applied Mechanics and Engineering*, 271:109–129, 2014.

[5] Kenneth J Bowles and Stephen Frimpong. Void effects on the interlaminar shear strength of unidirectional graphite-fiber-reinforced composites. *Journal of composite materials*, 26(10):1487–1509, 1992.

[6] Michaël Bruyneel and Samih Zein. A modified fast marching method for defining fiber placement trajectories over meshes. *Computers & Structures*, 125:45–52, 2013.

[7] Baoxing Chen, Eric J Lang, and Tsu-Wei Chou. Experimental and theoretical studies of fabric compaction behavior in resin transfer molding. *Materials Science and Engineering: A*, 317(1):188–196, 2001.

[8] David L Chopp. Replacing iterative algorithms with single-pass algorithms. *Proceedings of the National Academy of Sciences*, 98(20):10992–10993, 2001.

[9] Peggi Clouston, Frank Lam, and J David Barrett. Interaction term of tsai-wu theory for laminated veneer. *Journal of materials in civil engineering*, 10(2):112–116, 1998.

[10] A Endruweit, F Gommer, and AC Long. Stochastic analysis of fibre volume fraction and permeability in fibre bundles with random filament arrangement. *Composites Part A: Applied Science and Manufacturing*, 49:109–118, 2013.

[11] Omar Faruk, Andrzej K Bledzki, Hans-Peter Fink, and Mohini Sain. Biocomposites reinforced with natural fibers: 2000–2010. *Progress in polymer science*, 37(11):1552–1596, 2012.

[12] FEDER. Macobio project. Online on http://www.centexbel.be/fr/projects/macobio, 2017.06.04.

[13] Ray S Fertig and Eric M Jensen. Effect of fiber volume fraction variation across multiple length scales on composite stress variation: the possibility of stochastic multiscale analysis. In *55th AIAA/ASMe/ASCE/AHS/SC Structures, Structural Dynamics, and Materials Conference*, page 1169, 2014.

[14] Daniel Gay. *Matériaux composites*. Hermes, 1987.

[15] Michel Geier, D Duedal, and L Rechner. *Guide pratique des matériaux composites*. Technique et Documentation Lavoisier, 1985.

[16] Christophe Geuzaine and Jean-François Remacle. Gmsh. Online on http://gmsh.info/, 2017.

[17] François Glineur. Modèles et méthodes d'optimisation [inma1702] : Slides de cours., 2013.

[18] Mahesh Gupta and KK Wang. Fiber orientation and mechanical properties of short-fiber-reinforced injection-molded composites: Simulated and experimental results. *Polymer Composites*, 14(5):367–382, 1993.

[19] Justin Hale. Boeing 787 from the ground up. *Aero*, 4(24):7, 2006.

[20] Kuang-Ting Hsiao, Rex Little, Omar Restrepo, and Bob Minaie. A study of direct cure kinetics characterization during liquid composite molding. *Composites Part A: Applied Science and Manufacturing*, 37(6):925–933, 2006.

[21] Shuping Huang, Sankaran Mahadevan, and Ramesh Rebba. Collocation-based stochastic finite element analysis for random field problems. *Probabilistic engineering mechanics*, 22(2):194–205, 2007.

[22] Derek Hull and TW Clyne. An introduction to composite materials, cambridge university press. *Macmillan, New Yovk*, 1981.

[23] Saâd Jbabdi, Pierre Bellec, Roberto Toro, Jean Daunizeau, Mélanie Pélégrini-Issac, and Habib Benali. Accurate anisotropic fast marching for diffusion-based geodesic tractography. *Journal of Biomedical Imaging*, 2008:2, 2008.

[24] T Kanit, S Forest, Ia Galliet, Va Mounoury, and D Jeulin. Determination of the size of the representative volume element for random composites: statistical and numerical approach. *International Journal of solids and structures*, 40(13):3647–3679, 2003.

[25] Kari Karhunen. *Ueber lineare Methoden in der Wahrscheinlichkeitsrechnung*. 1947.

[26] Autar K Kaw. *Mechanics of composite materials*. CRC press, 2005.

[27] Roland Keunings. Mécanique des matériaux composites. *Nodes du cours MECA2640*, 2007.

[28] Ron Kimmel and James A Sethian. Computing geodesic paths on manifolds. *Proceedings of the National Academy of Sciences*, 95(15):8431–8435, 1998.

[29] Ender Konukoglu, Maxime Sermesant, Olivier Clatz, Jean-Marc Peyrat, Hervé Delingette, and Nicholas Ayache. A recursive anisotropic fast marching approach to reaction diffusion equation: Application to tumor growth modeling. In *Information processing in medical imaging*, pages 687–699. Springer, 2007.

[30] Olivier Le Maître and Omar M Knio. *Spectral methods for uncertainty quantification: with applications to computational fluid dynamics*. Springer Science & Business Media, 2010.

[31] Vincent Legat. Introduction aux éléments finis. *Notes du cours MECA2120*, 2004.

[32] D Liaw, S Singhal, P Murthy, and CHRISTOS CHAMIS. Quantification of uncertainties in composites. In *34th Structures, Structural Dynamics and Materials Conference*, page 1440, 1993.

[33] M Ločve. Fonctions aléatoires de second order, supplement to p. *Levy, Processus Stochastiques et Mouvement Brownien, Gauthier-Villars, Paris*, 1948.

[34] Pankar K Mallick. *Fiber-reinforced composites: materials, manufacturing, and design*. CRC press, 2007.

[35] MathWorks. Matlab. Online on `https://nl.mathworks.com/products/matlab.html`, 2017.

[36] Frank L Matthews and Rees D Rawlings. *Composite materials: engineering and science*. Elsevier, 1999.

[37] James Mercer. Functions of positive and negative type, and their connection with the theory of integral equations. *Philosophical transactions of the royal society of London. Series A, containing papers of a mathematical or physical character*, 209:415–446, 1909.

[38] TS Mesogitis, AA Skordos, and AC Long. Uncertainty in the manufacturing of fibrous thermosetting composites: A review. *Composites Part A: Applied Science and Manufacturing*, 57:67–75, 2014.

[39] TS Mesogitis, Alexandros A Skordos, and AC Long. Stochastic simulation of the influence of cure kinetics uncertainty on composites cure. *Composites Science and Technology*, 110:145–151, 2015.

[40] GNU Octave. Octave. Online on `https://www.gnu.org/software/octave/`, 2017.

[41] SK Padmanabhan and R Pitchumani. Stochastic analysis of isothermal cure of resin systems. *Polymer composites*, 20(1):72, 1999.

[42] Kim L Pickering, MG Aruan Efendy, and Tan Minh Le. A review of recent developments in natural fibre composites and their mechanical performance. *Composites Part A: Applied Science and Manufacturing*, 83:98–112, 2016.

[43] KD Potter. Understanding the origins of defects and variability in composites manufacture. In *International Conference on Composite Materials (ICCM)-17, Edinburgh, UK*, 2009.

[44] Python. Python. Online on `https://www.python.org/about/`, 2017.

[45] Jianliang Qian, Yong-Tao Zhang, and Hong-Kai Zhao. Fast sweeping methods for eikonal equations on triangular meshes. *SIAM Journal on Numerical Analysis*, 45(1):83–107, 2007.

[46] Carl Edward Rasmussen and Christopher KI Williams. Gaussian processes for machine learning. 2006. *The MIT Press, Cambridge, MA, USA*, 38:715–719, 2006.

[47] Junuthula Narasimha Reddy, Anna Cuprjak, and Loïc Villain. *Mécanique des milieux continus: introduction aux principes et applications*. de Boeck, 2013.

[48] Joon-Kyung Seong, Won-Ki Jeong, and Elaine Cohen. Anisotropic geodesic distance computation for parametric surfaces. In *Shape Modeling and Applications, 2008. SMI 2008. IEEE International Conference on*, pages 179–186. IEEE, 2008.

[49] James A Sethian and Alexander Vladimirsky. Ordered upwind methods for static hamilton–jacobi equations: Theory and algorithms. *SIAM Journal on Numerical Analysis*, 41(1):325–363, 2003.

[50] James Albert Sethian. *Level set methods and fast marching methods: evolving interfaces in computational geometry, fluid mechanics, computer vision, and materials science*, volume 3. Cambridge university press, 1999.

[51] RMJS Sidhu, RC Averill, M Riaz, and F Pourboghrat. Finite element analysis of textile composite preform stamping. *Composite structures*, 52(3):483–497, 2001.

[52] Alexandros A Skordos and Michael PF Sutcliffe. Stochastic simulation of woven composites forming. *Composites Science and Technology*, 68(1):283–296, 2008.

[53] Siemens PLM Software. Samcef. Online on `https://www.plm.automation.siemens.com/en/products/lms/samtech/samcef-solver-suite/`, 2017.

[54] Bruno Sudret and Armen Der Kiureghian. *Stochastic finite element methods and reliability: a state-of-the-art report*. Department of Civil and Environmental Engineering, University of California Berkeley, CA, 2000.

[55] Harry L Van Trees. *Detection, estimation, and modulation theory*. John Wiley & Sons, 2004.

[56] Libo Yan, Nawawi Chouw, and Xiaowen Yuan. Improving the mechanical properties of natural fibre fabric reinforced epoxy composites by alkali treatment. *Journal of Reinforced Plastics and Composites*, 31(6):425–437, 2012.

[57] Samih Zein, Adissa Laurent, and David Dumas. Simulation of a gaussian random field over a 3d surface for the uncertainty quantification in the composite structures. Submitted for publication.

[58] F Zhang, Sébastien Comas-Cardona, and Christophe Binetruy. Statistical modeling of in-plane permeability of non-woven random fibrous reinforcement. *Composites science and technology*, 72(12):1368–1379, 2012.

[59] Jinchun Zhu, Huijun Zhu, James Njuguna, and Hrushikesh Abhyankar. Recent development of flax fibres and their reinforced composites based on different polymeric matrices. *Materials*, 6(11):5171–5198, 2013.

Appendices

Appendix A

Proof of the rule of mixtures

The rule of mixtures determines the 4 engineering constants E_1, E_2, ν_{12} and G_{12} based on the properties of the fibres, the matrix and on FVF under the following assumptions:

- the material is free of voids
- the fibres and the matrix are homogeneous, linear elastic and isotropic elements
- fibres are continuous, parallel and the space between fibres is uniform
- perfect bound between the matrix and the fibres

Let $V_f = \frac{V_{fibre}}{V_{tot}}$ the fibre volume fraction, E_i, ν_i and G_i respectively the Young modulus, the Poisson ration and the shear modulus of material $i = \{f, m\}$ with f the fibre and m the matrix.

A.1 Longitudinal Young's modulus

The RVE is subject to uniaxial stress σ_1 in the direction of the fibres (see figure A.1).

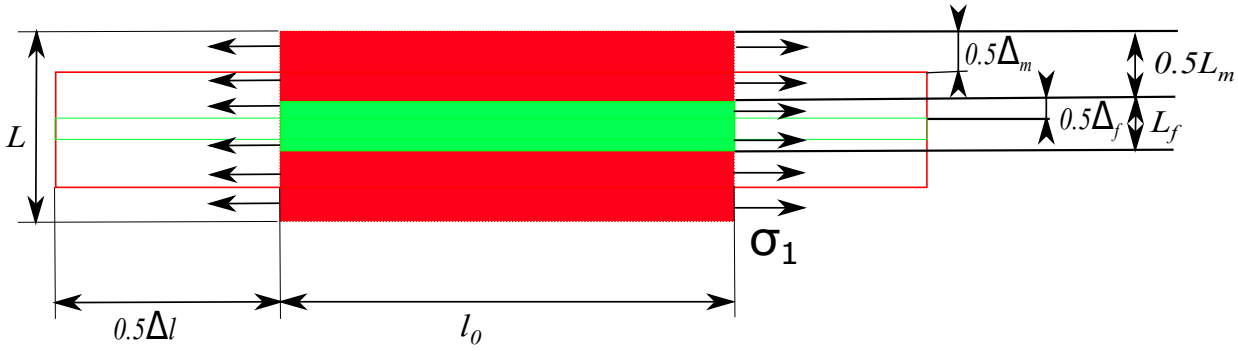

Figure A.1: RVE under longitudinal stress.

The deformation is supposed uniform in the RVE:

$$\epsilon_1 = \frac{\Delta l}{l_0}$$

where l_0 is the initial length of the RVE in the direction of the fibres and Δl is the deformation in the direction of the fibres. The stresses in the fibres σ_f and in the matrix σ_m are given by:

$$\sigma_f = E_f \epsilon_1 \qquad\qquad \sigma_m = E_m \epsilon_1$$

The total loads on the cross section of the fibres F_f, the matrix F_m and the composite F are given by

$$F_f = \sigma_f A_f \qquad F_m = \sigma_m A_m \qquad F = \sigma_1 A = F_f + F_m \tag{A.1}$$

where A_f, A_m and $A = A_f + A_m$ are respectively the areas of the cross section of the fibres, the matrix and the RVE. The longitudinal Young's modulus can be written as a function of E_f, E_m and FVF using relation (A.1):

$$\sigma_1 = \sigma_f V_f + \sigma_m (1 - V_f) \Rightarrow E_1 = E_f V_f + E_m (1 - V_f)$$

A.2 Transverse Young's modulus

The RVE is subject to uniaxial stress σ_2 in the direction perpendicular to the fibres (see figure A.2).
The stresses applied to the fibres, the matrix and the composite are supposed to be equal $\sigma_2 = \sigma_f = \sigma_m$. The transverse expansion of the RVE, Δ, is the sum of the transverse expansion of the fibres, Δ_f, and the transverse expansion of the matrix, Δ_m:

$$\Delta_f = \epsilon_f L_f \qquad \Delta_m = \epsilon_m L_m \qquad \Delta = \epsilon_2 L = \Delta_f + \Delta_m$$

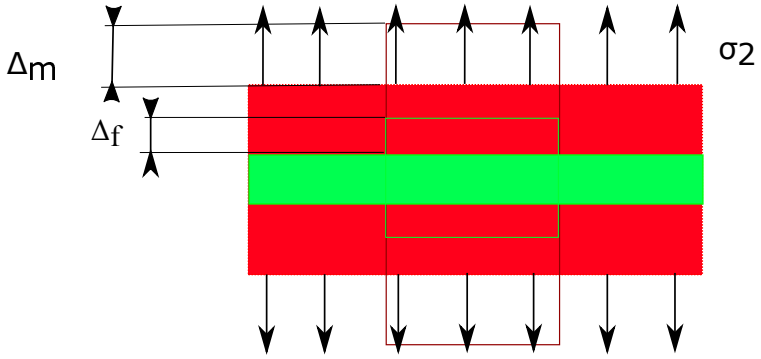

Figure A.2: RVE under transverse stress.

with L_f the transverse length of the fibres, L_m the transverse length of the matrix, L the transverse length of the RVE and ϵ_f, ϵ_m such that:

$$\epsilon_f = \frac{\sigma_2}{E_f} \qquad \epsilon_m = \frac{\sigma_2}{E_m} \qquad \epsilon_2 = \frac{\sigma_2}{E_2}$$

The transverse Young's modulus is thus given by:

$$E_2 = \left(\frac{V_f}{E_f} + \frac{(1-V_f)}{E_m}\right)^{-1}$$

A.3 Major Poisson's ratio

The RVE is subject to uniaxial stress σ_1 in the direction of the fibres (see figure A.1). The transverse deformation Δ of the RVE is the sum of the transverse deformation of the fibres Δ_f and the matrix Δ_m:

$$\Delta_f = \nu_f L_f \epsilon_1 \qquad \Delta_m = \nu_m L_m \epsilon_1 \qquad \Delta = \nu_{12} L \epsilon_1 = \Delta_f + \Delta_m$$

which allows to find the major Poisson's ratio:

$$\nu_{12} = V_f \nu_f + (1-V_f)\nu_m$$

A.4 In plane shear modulus

The RVE, the fibres and the matrix are subject to pure shear stress τ (see figure A.3). The shear strains of the fibres ϵ_f, the matrix

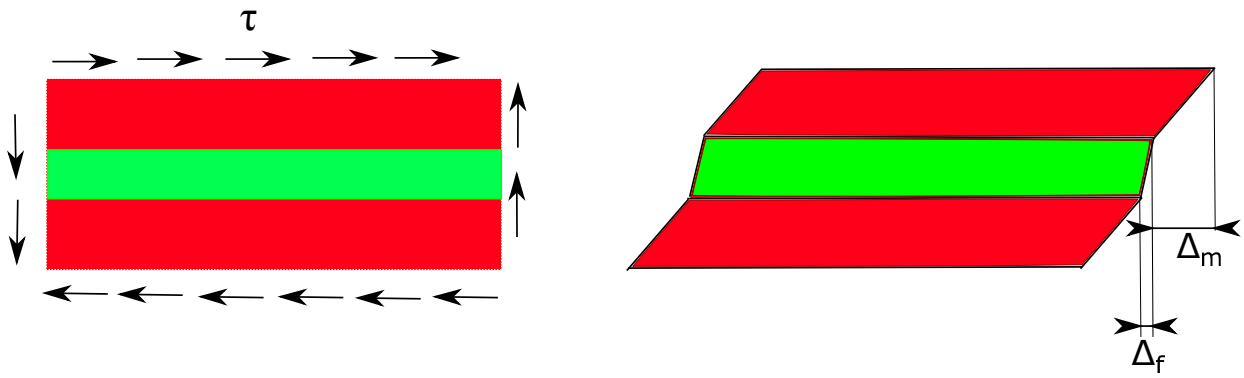

Figure A.3: RVE under shear stress.

ϵ_m and the RVE ϵ_6 are given by

$$\epsilon_f = \frac{\tau}{G_f} \qquad \epsilon_m = \frac{\tau}{G_m} \qquad \epsilon_6 = \frac{\tau}{G_{12}}$$

Furthermore, the total longitudinal deformation Δ is equal to the sum of the longitudinal deformations of the fibres Δ_f and the matrix Δ_m:

$$\Delta_f = \epsilon_f L_f \qquad \Delta_m = \epsilon_m L_m \qquad \Delta = \epsilon_6 L = \Delta_f + \Delta_m$$

with L_f the transverse length of the fibres, L_m the transverse length of the matrix and L the transverse length of the RVE. The in plane shear modulus is given by:

$$G_{12} = \left(\frac{V_f}{G_f} + \frac{V_m}{G_m}\right)^{-1}$$

Appendix B

Proof of the macro mechanical model of a laminate

Based on the mechanical properties of the plies and the angles of the plies with respect to the main axes, the CLT predicts the mechanical properties and responses of a laminate shown with its axis coordinate system $(\boldsymbol{e}_x, \boldsymbol{e}_y, \boldsymbol{e}_z)$ on figure B.1. The plane Oxy is set on the mid-surface of the laminate. The CLT makes the following hypothesis: displacements are continuous and small along axis $\boldsymbol{e}_z$, the laminate is only loaded in its plane (σ_{xz}, σ_{yz}, σ_{zz} are negligible with respect to σ_x, σ_y, σ_{xy}) and a straight perpendicular line to the mid-surface remains straight, perpendicular and of same length after deformation ($\epsilon_{xz} = \epsilon_{yz} = \epsilon_z = 0$).
Denoting $\mathtt{u}_0$, $\mathtt{v}_0$ and $\mathtt{w}_0$ the displacements on the mid-surface in directions $\boldsymbol{e}_x$, $\boldsymbol{e}_y$ and $\boldsymbol{e}_z$ and $\mathtt{u}$, $\mathtt{v}$ and $\mathtt{w}$ the displacements in directions $\boldsymbol{e}_x$, $\boldsymbol{e}_y$ and $\boldsymbol{e}_z$, the goal is to determine displacements and deformations inside the laminate as a function of displacements and deformations on the mid-surface. Fix a point $\boldsymbol{C}$ situated outside the mid-surface of the laminate and perpendicular to a point $\boldsymbol{B}$ located on the mid-surface. The two points are separated by a distance z. After deformation, segment $\boldsymbol{BC}$ form an angle α with respect to the normal of the Oxy plane. The laminate is shown before and after deformation at figure B.2.

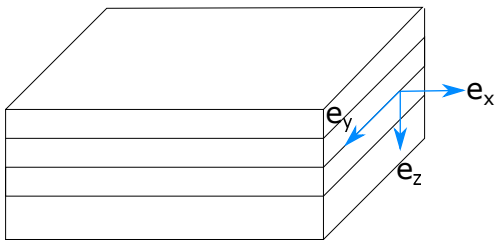

Figure B.1: Laminate structure and coordinate system.

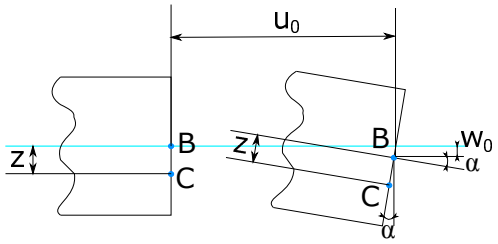

Figure B.2: Laminate deformation in the Oxy plane.

Kirchoff approximation allows to find the displacement along $\boldsymbol{e}_x$:

$$\epsilon_z = 0 \Longrightarrow \mathtt{u} = \mathtt{u}_0 - z\alpha$$
$$\epsilon_{xz} = 0 \Longrightarrow \alpha = \frac{\partial \mathtt{w}_0}{\partial x}$$

Displacement along directions $\boldsymbol{e}_x$, $\boldsymbol{e}_y$ and $\boldsymbol{e}_z$ are thus given by:

$$\mathtt{u}(x,y,z) = \mathtt{u}_0(x,y) - z\frac{\partial \mathtt{w}_0(x,y)}{\partial x}$$
$$\mathtt{v}(x,y,z) = \mathtt{v}_0(x,y) - z\frac{\partial \mathtt{w}_0(x,y)}{\partial y}$$
$$\mathtt{w}(x,y,z) = \mathtt{w}_0(x,y)$$

The corresponding strains are given by:

$$\epsilon_x = \frac{\partial \mathtt{u}}{\partial x} = \frac{\partial \mathtt{u}_0}{\partial x} - z\frac{\partial^2 \mathtt{w}_0}{\partial x^2}$$
$$\epsilon_y = \frac{\partial \mathtt{v}}{\partial y} = \frac{\partial \mathtt{v}_0}{\partial y} - z\frac{\partial^2 \mathtt{w}_0}{\partial y^2}$$
$$2\epsilon_{xy} = \frac{\partial \mathtt{u}}{\partial y} + \frac{\partial \mathtt{v}}{\partial x} = \frac{\partial \mathtt{u}_0}{\partial y} + \frac{\partial \mathtt{v}_0}{\partial x} - 2z\frac{\partial^2 \mathtt{w}_0}{\partial x \partial y}$$

Denoting the strains of the mid-surface by $\boldsymbol{\epsilon}_0 = \begin{pmatrix}\epsilon_x^0 & \epsilon_y^0 & 2\epsilon_{xy}^0\end{pmatrix}^T = \begin{pmatrix}\frac{\partial \mathtt{u}_0}{\partial x} & \frac{\partial \mathtt{v}_0}{\partial y} & \frac{\partial \mathtt{u}_0}{\partial y} + \frac{\partial \mathtt{v}_0}{\partial x}\end{pmatrix}^T$, the mid-plane curvatures by $\boldsymbol{\kappa} = \begin{pmatrix}\kappa_x & \kappa_y & \kappa_z\end{pmatrix}^T = \begin{pmatrix}-\frac{\partial^2 \mathtt{w}_0}{\partial x^2} & -\frac{\partial^2 \mathtt{w}_0}{\partial y^2} & -2\frac{\partial^2 \mathtt{w}_0}{\partial x \partial y}\end{pmatrix}^T$ and the strains inside the laminate by $\boldsymbol{\epsilon} = \begin{pmatrix}\epsilon_x & \epsilon_y & 2\epsilon_{xy}\end{pmatrix}^T$, the strains can be expressed as

$$\boldsymbol{\epsilon}(x,y,z) = \boldsymbol{\epsilon_0}(x,y) + z\boldsymbol{\kappa}(x,y)$$

The strain stress relation of a ply k with stiffness matrix $\boldsymbol{C}_k$ (in local axis $\boldsymbol{e}_x$ and $\boldsymbol{e}_y$) is given by

$$\boldsymbol{\sigma}_k(x,y,z) = \boldsymbol{C}_k\boldsymbol{\epsilon_0}(x,y) + z\boldsymbol{C}_k\boldsymbol{\kappa}(x,y)$$

Given a n ply laminate of thickness h, the resultant forces per unit length $\boldsymbol{N}(x,y)$ and the resultant moments $\boldsymbol{M}(x,y)$ are given

by

$$\boldsymbol{N}(x,y) = \begin{pmatrix} N_x & N_y & N_{xy} \end{pmatrix}^T = \int_{-\frac{h}{2}}^{\frac{h}{2}} \boldsymbol{\sigma} dz = \sum_{k=1}^{n} \int_{h_{k-1}}^{h_k} \boldsymbol{\sigma}_k dz \tag{B.1}$$

$$\boldsymbol{M}(x,y) = \begin{pmatrix} M_x & M_y & M_{xy} \end{pmatrix}^T = \int_{-\frac{h}{2}}^{\frac{h}{2}} z\boldsymbol{\sigma} dz = \sum_{k=1}^{n} \int_{h_{k-1}}^{h_k} z\boldsymbol{\sigma}_k dz \tag{B.2}$$

with $h_k = -\frac{h}{2} + \sum_{u=1}^{k} t_u$ for $k = 1, ..., n$ and $h_0 = -\frac{h}{2}$. In this expression, t_k is the thickness of ply k and $\sum_{u=1}^{n} t_u = h$. Replacing $\boldsymbol{\sigma}_k$ by its expression, equations (B.1) and (B.2) become:

$$\boldsymbol{N}(x,y) = \sum_{k=1}^{n} \boldsymbol{C}_k \left(\boldsymbol{\epsilon_0} \int_{h_{k-1}}^{h_k} dz + \boldsymbol{\kappa} \int_{h_{k-1}}^{h_k} z dz \right)$$

$$\boldsymbol{M}(x,y) = \sum_{k=1}^{n} \boldsymbol{C}_k \left(\boldsymbol{\epsilon_0} \int_{h_{k-1}}^{h_k} z dz + \boldsymbol{\kappa} \int_{h_{k-1}}^{h_k} z^2 dz \right)$$

Knowing that

$$\int_{h_{k-1}}^{h_k} dz = h_k - h_{k-1} \qquad \int_{h_{k-1}}^{h_k} z dz = \frac{1}{2}(h_k^2 - h_{k-1}^2) \qquad \int_{h_{k-1}}^{h_k} z^2 dz = \frac{1}{3}(h_k^3 - h_{k-1}^3)$$

allow to conclude

$$\begin{pmatrix} \boldsymbol{N} \\ \boldsymbol{M} \end{pmatrix} = \begin{pmatrix} \boldsymbol{P} & \boldsymbol{Q} \\ \boldsymbol{Q} & \boldsymbol{R} \end{pmatrix} \begin{pmatrix} \boldsymbol{\epsilon}_0 \\ \boldsymbol{\kappa} \end{pmatrix} \tag{B.3}$$

with

$$P_{ij} = \sum_{k=1}^{n} (C_{ij})_k (h_k - h_{k-1})$$

$$Q_{ij} = \frac{1}{2} \sum_{k=1}^{n} (C_{ij})_k (h_k^2 - h_{k-1}^2)$$

$$R_{ij} = \frac{1}{3} \sum_{k=1}^{n} (C_{ij})_k (h_k^3 - h_{k-1}^3)$$

Appendix C

Discrete Fredholm equation : implementation details

This section is mainly inspired from [31].

C.1 Approximation of the eigenfunctions

In order to develop a general framework, we will work on standard elements. Let's consider a mesh made of triangular elements. Lets take a random triangular element Ω_e whose vertex are given by $P_1 = (X_1^e; Y_1^e; Z_1^e)$, $P_2 = (X_2^e; Y_2^e; Z_2^e)$ and $P_3 = (X_3^e; Y_3^e; Z_3^e)$. The standard triangle is such that its projection on space $(\eta; \xi)$ has coordinates $\Xi_1 = (0; 0)$, $\Xi_2 = (1; 0)$ and $\Xi_3 = (0; 1)$.
The isomorphism between the triangular element Ω_e in space $\boldsymbol{x} = (x; y; z)$ and the standard triangle $\hat{\Omega}$ in space $\boldsymbol{\xi} = (\xi; \eta; \zeta)$ is defined as

$$
\begin{aligned}
x(\boldsymbol{\xi}) &= P(\xi, \eta) = (1 - \xi - \eta)X_1^e + \xi X_2^e + \eta X_3^e \\
y(\boldsymbol{\xi}) &= Q(\xi, \eta) = (1 - \xi - \eta)Y_1^e + \xi Y_2^e + \eta Y_3^e \\
z(\boldsymbol{\xi}) &= R(\xi, \eta) = (1 - \xi - \eta)Z_1^e + \xi Z_2^e + \eta Z_3^e
\end{aligned}
$$

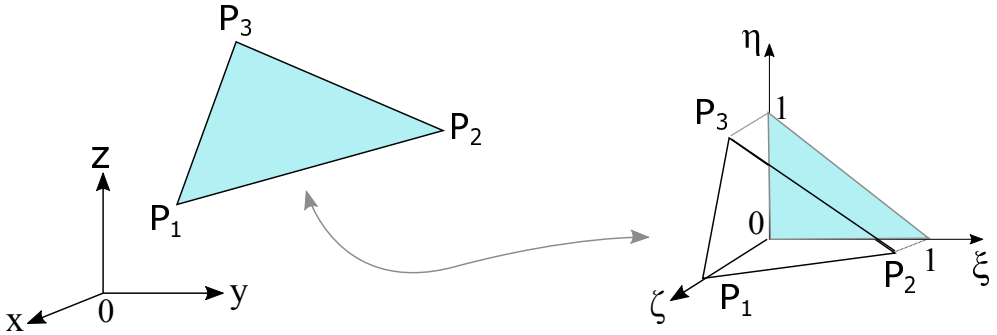

Figure C.1: Isomorphism between a random finite element Ω_e and the standard element $\hat{\Omega}$

On every element, we wish to approximate the eigenfunction ϕ_i by a set of functions $\phi_i(\boldsymbol{x}) \approx \hat{\phi}_i(\boldsymbol{x}) = \sum_{j=1}^{N} d_j^i h_j(\boldsymbol{x})$. We associate every basis function h_j to a node $\boldsymbol{X}_j$ such that

$$
h_j(\boldsymbol{X}_i) = \delta_{ij} = \begin{cases} 1 \text{ if } i = j \\ 0 \text{ else} \end{cases}
$$

The basis functions are polynomials. To correctly interpolate polynomials of order 0, one only needs one basis function linked to the center of mass of the triangle:

$$
h_1(\boldsymbol{\xi}) = 1 \tag{C.1}
$$

To correctly interpolate polynomials of order 1, one needs 3 linear basis functions. Every basis function is linked to a vertex of the triangle:

$$
h_1(\boldsymbol{\xi}) = 1 - \xi - \eta \qquad h_2(\boldsymbol{\xi}) = \xi \qquad h_3(\boldsymbol{\xi}) = \eta \tag{C.2}
$$

C.2 Quadrature rules

Integrals (4.5) can be written as the sum of the integrals over the mesh elements:

$$
A_{i,j} = \sum_e \sum_f \int_{\Omega^e} h_i(\boldsymbol{x}) \int_{\Omega f} C(\boldsymbol{x}, \boldsymbol{y}) h_j(\boldsymbol{y}) d\boldsymbol{y} d\boldsymbol{x} \qquad B_{i,j} = \sum_e \int_{\Omega^e} h_i(\boldsymbol{x}) h_j(\boldsymbol{x}) d\boldsymbol{x} \tag{C.3}
$$

In order to evaluate integrals (C.3), the triangular mesh elements Ω^e and Ω^f are mapped to the standard triangle $\hat{\Omega}$. The integrals in the sum become

$$\int_{\Omega^e} h_i(\boldsymbol{x}) \int_{\Omega^f} C(\boldsymbol{x},\boldsymbol{y}) h_j(\boldsymbol{y}) d\boldsymbol{y} d\boldsymbol{x}$$
$$= \int_{\hat{\Omega}} h_i(\boldsymbol{x}(\xi,\eta)) \int_{\hat{\Omega}} C(\boldsymbol{x}(\xi,\eta),\boldsymbol{y}(\xi,\eta)) h_j(\boldsymbol{y}(\xi,\eta)) |J_1(\xi,\eta)||J_2(\xi,\eta)| d\boldsymbol{\xi_1} d\boldsymbol{\xi_2}$$
$$\int_{\Omega^e} h_i(\boldsymbol{x}) h_j(\boldsymbol{x}) d\boldsymbol{x} = \int_{\hat{\Omega}} h_i(\boldsymbol{x}(\xi,\eta)) h_j(\boldsymbol{x}(\xi,\eta)) |J_1(\xi,\eta)| d\boldsymbol{\xi_1}$$

where $J_1(\xi,\eta)$ and $J_2(\xi,\eta)$ are the Jacobian of the transformations. The first Jacobian is given by

$$J_1(\xi,\eta) = \left| \frac{\partial(x,y,z)}{\partial(\xi,\eta)} \right| = 2A_e$$

where A_e is the area of element Ω_e. $J_2(\xi,\eta)$ is defined similarly with respect to element Ω_f.

Gaussian quadratures on triangles take the form

$$\int_{\hat{\Omega}} g(\xi,\eta) d\boldsymbol{\xi} \approx \frac{1}{2} \sum_p w_p g(\boldsymbol{x}_p)$$

A quadrature of degree N is exact for all polynomials of degree N in two dimensions. In the rest of this thesis, the integration will be computed using quadrature rules of degree 1 and 3.
A quadrature of degree 1 perfectly integrates all polynomials spanned by the basis $span\{1,\xi,\eta\}$. In other words

$$\begin{cases} \int_{\hat{\Omega}} 1 d\boldsymbol{\xi} = \frac{1}{2} & = \frac{1}{2} \sum_p w_p g(\boldsymbol{x}_p) \\ \int_{\hat{\Omega}} \xi d\boldsymbol{\xi} = \frac{1}{6} & = \frac{1}{2} \sum_p w_p g(\boldsymbol{x}_p) \\ \int_{\hat{\Omega}} \eta d\boldsymbol{\xi} = \frac{1}{6} & = \frac{1}{2} \sum_p w_p g(\boldsymbol{x}_p) \end{cases} \tag{C.4}$$

A solution is given by $w_1 = 1$, $\xi_1 = \eta_1 = \frac{1}{3}$.
A quadrature of degree 3 perfectly integrates all polynomials spanned by the basis $span\{1,\ \xi,\ \eta,\ \xi^2,\ \eta^2,\ \xi\eta,\ \xi^3,\ \eta^3,\ \xi^2\eta,\ \eta^2\xi\}$. In other words

$$\begin{cases} \int_{\hat{\Omega}} 1 d\boldsymbol{\xi} & = \frac{1}{2} = \frac{1}{2} \sum_p w_p g(\boldsymbol{x}_p) \\ \int_{\hat{\Omega}} \xi d\boldsymbol{\xi} = \int_{\hat{\Omega}} \eta d\boldsymbol{\xi} & = \frac{1}{6} = \frac{1}{2} \sum_p w_p g(\boldsymbol{x}_p) \\ \int_{\hat{\Omega}} \xi^2 d\boldsymbol{\xi} = \int_{\hat{\Omega}} \eta^2 d\boldsymbol{\xi} & = \frac{1}{12} = \frac{1}{2} \sum_p w_p g(\boldsymbol{x}_p) \\ \int_{\hat{\Omega}} \xi\eta d\boldsymbol{\xi} & = \frac{1}{24} = \frac{1}{2} \sum_p w_p g(\boldsymbol{x}_p) \\ \int_{\hat{\Omega}} \xi^3 d\boldsymbol{\xi} = \int_{\hat{\Omega}} \eta^3 d\boldsymbol{\xi} & = \frac{1}{20} = \frac{1}{2} \sum_p w_p g(\boldsymbol{x}_p) \\ \int_{\hat{\Omega}} \xi^2\eta d\boldsymbol{\xi} = \int_{\hat{\Omega}} \xi\eta^2 d\boldsymbol{\xi} & = \frac{1}{12} = \frac{1}{2} \sum_p w_p g(\boldsymbol{x}_p) \end{cases} \tag{C.5}$$

The associated weight to the ten quadrature points shown on figure C.2 are given by

$$w_1 = w_4 = w_{10} = \frac{1}{30}$$
$$w_2 = w_3 = w_5 = w_7 = w_8 = w_9 = 0.075$$
$$w_6 = 0.45$$

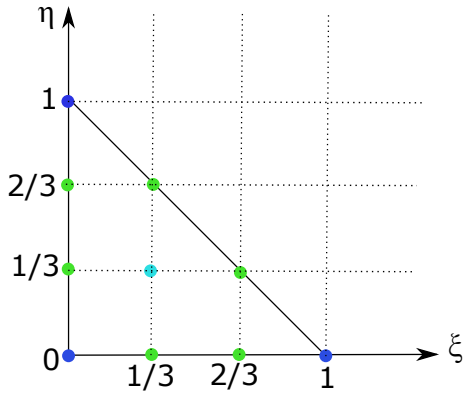

Figure C.2: Quadrature points of the quadrature rule of degree 3.

Appendix D

Solution of the optimisation problem involved in AFMM

Considering a triangle XYZ in which we know T_Y and T_Z, the AFMM tries to find point $\tilde{x} = p(Y - Z) + Z$ on segment YZ that minimises the anisotropic distance T_X. The optimisation problem is given by:

$$f_{2D}(X, Y, Z) = \min_{p\in[0,1]} pT_Y + (1-p)T_Z + ||\tilde{x}X||_M$$

It can be written as

$$f_{2D}(X, Y, Z) = \min_{p\in[0,1]} pT_Y + (1-p)T_Z + \left((p\boldsymbol{YX} + (1-p)\boldsymbol{ZX})\,\boldsymbol{M}\,(p\boldsymbol{YX} + (1-p)\boldsymbol{ZX})\right)^{\frac{1}{2}} \tag{D.1}$$

$$= \min_{p\in[0,1]} pT_Y + (1-p)T_Z + \left(p^2a + pb + c\right)^{\frac{1}{2}} \tag{D.2}$$

with

$$\begin{aligned} a &= \boldsymbol{YX}\cdot\boldsymbol{M}\cdot\boldsymbol{YX} + \boldsymbol{ZX}\cdot\boldsymbol{M}\cdot\boldsymbol{ZX} - \boldsymbol{YX}\cdot\boldsymbol{M}\cdot\boldsymbol{ZX} - \boldsymbol{ZX}\cdot\boldsymbol{M}\cdot\boldsymbol{YX} \\ b &= \boldsymbol{YX}\cdot\boldsymbol{M}\cdot\boldsymbol{ZX} + \boldsymbol{ZX}\cdot\boldsymbol{M}\cdot\boldsymbol{YX} - 2\boldsymbol{ZX}\cdot\boldsymbol{M}\cdot\boldsymbol{ZX} \\ c &= \boldsymbol{ZX}\cdot\boldsymbol{M}\cdot\boldsymbol{ZX} \end{aligned}$$

This problem is an optimisation problem with two inequality constraints. It can be solved using the Lagrangian method. Let's recall how the Lagrangian method works [17]. Given a function f defined on the real space, the optimisation problem is written as:

$$\begin{aligned} &\min_{x\in\mathbb{R}^n} f(x) \\ &\quad c_i(x) = 0 \qquad \forall i \in \mathcal{E} \\ &\quad c_i(x) \geq 0 \qquad \forall i \in \mathcal{I} \end{aligned}$$

where $\mathcal{E}$ is the set containing all equalities' indices and $\mathcal{E}$ is the set containing all inequalities' indices. The Lagrangian function is defined as

$$\mathcal{L}(x, \lambda) \equiv f(x) - \sum_i \lambda_i c_i(x)$$

The KKT conditions express that, if x^* is an extremum, and all gradients $\{\nabla c_i(x^*)\}_{i\in\mathcal{A}(x^*)}$, with $\mathcal{A}(x) = \{i \in \mathcal{E} \cap \mathcal{I} | c_i(x) = 0\}$, are independent, there exist a $\boldsymbol{\lambda}^*$ such that

$$\begin{aligned} \nabla_x\mathcal{L}(x^*, \boldsymbol{\lambda}^*) &= 0 \\ \lambda_i^* &\geq 0 \qquad i \in \mathcal{I} \\ \lambda_i^* c_i(x^*) &= 0 \qquad i \in \mathcal{I} \end{aligned}$$

The Lagrangian function associated with optimisation problem (D.2) is given by :

$$\mathcal{L}(p) = pT_Y + (1-p)T_Z + \left(p^2a + pb + c\right)^{\frac{1}{2}} - \lambda_1 c_1(p) - \lambda_2 c_2(p)$$

with $c_1(p) = p$ and $c_2(p) = 1 - p$. The gradient of the Lagrangian function with respect to p is given by

$$\nabla_p\mathcal{L}(p) = T_Y - T_Z + \frac{2ap + b}{2\sqrt{p^2a + bp + c}} - \lambda_1 + \lambda_2$$

The KKT conditions are given by:

$$\begin{aligned} \nabla_p\mathcal{L}(p^*) &= 0 \\ \lambda_1^* p^* &= 0 \\ (1 - p^*)\lambda_2^* &= 0 \end{aligned}$$

Furthermore, if $c_1(p*) = 0$, then $c_2(p*) = 1$ and inversely. The gradient of the constraints only contain one element. Let's analyse whether the KKT conditions can be satisfied. Three cases must be checked :

$\lambda_1^* = \lambda_2^* = 0$: The first KKT condition can be written as the second order equation

$$0 = \alpha p^2 + \beta p + \gamma \tag{D.3}$$
$$\alpha = 4a^2 - 4a(T_Z - T_Y)^2 \tag{D.4}$$
$$\beta = 4ab - 4b(T_Z - T_Y)^2 \tag{D.5}$$
$$\gamma = b^2 - 4c(T_Z - T_Y)^2 \tag{D.6}$$

A possible admissible solution is a solution of equation (D.3) with real value between 0 and 1. Because the problem is convex, an admissible solution is necessarily the global optimum.

$\lambda_1^* = 0,\ \lambda_2^* \neq 0$: The candidate solution is given by $p^* = 1$. The solution is admissible if $\lambda_2^* = -T_Y + T_Z - \frac{2a+b}{2\sqrt{a+b+c}} > 0$.

$\lambda_1^* \neq 0,\ \lambda_2^* = 0$: The candidate solution is given by $p^* = 0$. The solution is admissible if $\lambda_2^* = T_Y - T_Z + \frac{b}{2\sqrt{c}} > 0$.

$\lambda_1^* \neq 0,\ \lambda_2^* \neq 0$: This case admits no possible solution.